UNIVERSIDADE DE SÃO PAULO
Faculdade de Filosofia, Ciências e Letras de Ribeirão Preto
Departamento de Física

André Monteiro Paschoal

Optimização e aplicação de métodos quantitativos de imagem por ressonância magnética para analisar perfusão sanguínea e funções cerebrais

Optimization and application of quantitative magnetic resonance imaging methods to analyze brain perfusion and function

Ribeirão Preto, São Paulo, Brasil
2019

André Monteiro Paschoal

Optimização e aplicação de métodos quantitativos de imagem por ressonância magnética para analisar perfusão sanguínea e funções cerebrais

Optimization and application of quantitative magnetic resonance imaging methods to analyze brain perfusion and function

Tese de doutorado apresentada ao Programa de Pós-Graduação em Física Aplicada à Medicina e Biologia do Departamento de Física da Faculdade de Filosofia, Ciências e Letras de Ribeirão Preto da Universidade de São Paulo, para a obtenção do título de Doutor em Ciências.

Universidade de São Paulo – USP

Faculdade de Filosofia, Ciências e Letras de Ribeirão Preto – FFCLRP

Programa de Pós-Graduação em Física Aplicada à Medicina e Biologia

Versão Corrigida

Supervisor: Renata Ferranti Leoni

Co-supervisor: Fernando Fernandes Paiva

Ribeirão Preto, São Paulo, Brasil

2019

Paschoal, André Monteiro

Optimização e aplicação de métodos quantitativos de imagem por ressonância-magnética para analisar perfusão sanguínea e funções cerebrais.

Optimization and application of quantitative magnetic resonance imaging methods to analyze brain perfusion and function / André Monteiro Paschoal. – Ribeirão Preto, São Paulo, Brasil, 2019-

120 p. : il. ; 30 cm.

Tese de doutorado apresentada ao Programa de Pós-Graduação em Física Aplicada à Medicina e Biologia do Departamento de Física da Faculdade de Filosofia, Ciências e Letras de Ribeirão Preto da Universidade de São Paulo

Supervisor: Renata Ferranti Leoni

1. Arterial spin labeling. 2. Cerebral blood flow. 3. Diffusion. 4. Functional MRI. 5. Intravoxel incoherent motion. 6. Perfusion.

André Monteiro Paschoal

Optimização e aplicação de métodos quantitativos de imagem por ressonância magnética para analisar perfusão sanguínea e funções cerebrais

Optimization and application of quantitative magnetic resonance imaging methods to analyze brain perfusion and function

Tese de doutorado apresentada ao Programa de Pós-Graduação em Física Aplicada à Medicina e Biologia do Departamento de Física da Faculdade de Filosofia, Ciências e Letras de Ribeirão Preto da Universidade de São Paulo, para a obtenção do título de Doutor em Ciências.

Ribeirão Preto, São Paulo, Brasil, 09 de dezembro de 2019:

Aprovado em:___/___/_____

Banca Avaliadora

Prof. Dr.:_____ Instituição: _____

Julgamento:_____ Assinatura: _____

Prof. Dr.:_____ Instituição: _____

Julgamento:_____ Assinatura: _____

Prof. Dr.:_____ Instituição: _____

Julgamento:_____ Assinatura: _____

Prof. Dr.:_____ Instituição: _____

Julgamento:_____ Assinatura: _____

Ribeirão Preto, São Paulo, Brasil
2019

Dedico este trabalho aos meus pais, Oswaldo e Ana Celia, e minha namorada Carol por todo apoio durante esta jornada.

Acknowledgements

À minha orientadora, professora Renata Leoni, por todo o suporte, sugestões e paciência ao longo dos últimos quatro anos. Obrigado por todas as discussões do projeto, dicas e orientação contínua que certamente contribuíram para este trabalho e, mais importante, para a minha formação como cientista.

Ao meu coorientador do doutorado e meu orientador do mestrado, professor Fernando Paiva, por sempre estar contribuindo com meus trabalhos e meu crescimento, mesmo que à distância. Espero que possamos continuar colaborando, apesar de agora você ser o cara das rochas!

To my advisor in Leiden, Prof. Thijs van Osch, my sincere gratitude for accepting me in your lab. Working with one of the greatest ASL reference was not only enriching for my career, but a really amazing life experience. Spending this time in Leiden was much easier and fun thanks to your attention and friendship. Thanks for all the discussion, journal clubs and scan sessions that really pushed my career up.

Also thanks for all colleagues from the Gorter Center, in special the ASL clan. Thanks Sophie, Suzanne, Merlijn, Leon, Thijs, Lydiane, Leonie, Lena, Sahar and Thom for all the discussion, coffees, drinks and all the patience that you had in helping me when I was lost in my activities. Also thanks to my office mates Thomas, Wyger and Myriam for helping me with so many things.

Aos brasileiros em Leiden, por toda a amizade que fizemos e que ainda continua firme e forte. Muito obrigado pela ajuda que vocês deram para mim e para a Carol em tantas situações. Obrigado também por cada reunião, cafés, happy hours e tantos outros momentos divertidos que tivemos. Espero poder rever vocês em breve, seja aqui no Brasil ou novamente em Leiden. Não vou citar nomes para não esquecer ninguém, mas todos foram igualmente importantes, inclusive os maridos holandeses das casadas :)

Ao pessoal do HCRP, todos os técnicos que me ajudaram durante as inúmeras sessões de ressonância que tivemos. Ao professor Antônio Carlos dos Santos, por toda a ajuda em arrumar tempo de máquina para nossas aquisições e pela colaboração que apenas iniciamos nestes 4 anos, ao professor Octávio Pontes-Neto, também pela frutífera colaboração que iniciamos e por todo o entusiasmo que trata a pesquisa. Agradeço também ao grupo da neurovasc, Dr. Guilherme, Dra Ana Paula por cada discussão que tivemos.

Ao laboratório InBrain em todos os diferentes momentos durante esses quatro anos. Sempre escutamos falar de desgastes emocionais durante a realização de um doutorado, mas com o ambiente deste laboratório não senti nem de perto qualquer tipo de desgaste ou cansaço. Acho que as pessoas não imaginam o quanto é divertido trabalhar quando se

está no lugar certo. Tanta gente passou nesses quatro anos, mas de uma forma ou de outra, o ambiente sempre foi cheio de diversão, cafés e bons momentos. Obrigado prof. Garrido por todas as discussões que foram muito importante para meu trabalho e pela amizade. Tanta gente que é difícil até começar, vou tentar seguir pela ordem cronológica. Felipe, Danilo, Carlo, Gustavo, Jeam, Icaro, Luciana, Pedro, Bruno, Maíra, João Paulo, Kaio, Isabella, Fábio, Hohana e aos mais novos InBrainners, Julia, Lucas, Larissa, obrigado pelo companheirismo de vocês durante todo esse tempo. Impossível falar individualmente de cada um, senão minha tese daria 400 páginas.

Aos meus pais por todo o apoio nesses longos anos de pós-graduação, por sempre apoiarem minhas decisões e por acreditarem em mim sempre. Mesmo nas situações mais difíceis e de incerteza, por sempre demonstrar total apoio e incentivo. Vocês são muito importantes.

Por fim, mas não menos importante, Carol, minha companheira de todos os momentos. Seu apoio durante esses quatro anos foram fundamentais, sempre apoiando minhas decisões. Em especial por ter embarcado comigo em nosso intercâmbio. Sei o quanto foi difícil para você, mas fez com que minha (nossa) experiência no exterior fosse muito mais fácil e completa. Obrigado por tudo. Obrigado também aos nossos pets Judy e Sophie, por tantos momentos alegres que fazem toda a diferença para aliviar o cansaço após um dia cheio de trabalho.

This study was financed in part by the Coordenação de Aperfeiçoamento de Pessoal de Nível Superior - Brasil (CAPES) - Finance Code 001 and Conselho Nacional de Desenvolvimento Científico e Tecnológico - Process Number 140110/2016-0.

Abstract

The human brain consists of a very complex and specialized organ and is responsible for coordinating the execution of several functions performed by the subjects. The brain tissue must be continuously supplied with oxygen and all the nutrients necessary to provide the required energy to keep all these mechanisms regulated in a normal condition since the brain is not capable of storing energy. The neurovascular system is crucial to keep the delivery of nutrients constant, though it implies a complex mechanism of auto-regulation. Deregulation of this essential mechanism may impair the delivery of nutrients according to the demand for energy, which may lead to various brain disorders.

Magnetic resonance imaging (MRI) is a potent imaging tool that allows the analysis of several characteristics related to brain structure, function, perfusion, water diffusion, and others. These characteristics can be assessed exploiting different possible contrast mechanisms. Arterial Spin Labeling (ASL) and Intravoxel Incoherent Motion (IVIM) are two noninvasive and quantitative methods based on blood perfusion and water diffusion, respectively, which enable the quantification of cerebral blood flow (CBF) and water diffusion coefficient in brain tissue. Moreover, due to the neurovascular coupling, the analysis of the temporal fluctuations in blood perfusion at different anatomical brain regions allows the study of brain functions, which is called functional MRI (fMRI) and consists of a widely used imaging modality to assess brain integrity.

In this study, we worked on the interface between the development of image acquisition and analysis methods, and their application in both healthy subjects and patients. Regarding acquisition methods, we worked on the optimization of the 3D Gradient and Spin Echo (GRASE) readout and the effect of flow compensated gradients in ASL images. For IVIM, we evaluated the effect of different acquisition parameters in the analysis model to optimize the analysis for neurological and neurovascular patients. Finally, we evaluated the capability of ASL to study brain functions in a resting-state condition and while performing different actions, such as motor and language tasks. We started with a simple and robust motor task to validate our method and then applied it to study a more complex function (language). We developed and implemented a novel dual-echo readout for ASL protocol to improve quantitative assessment of the CBF and the blood oxygen level-dependent (BOLD) signals.

The main findings of this thesis include the better delineation of the arterial signal when using segmented 3D GRASE and flow compensation gradients; the demonstration of the feasibility of ASL with dual-echo readout in a simultaneous accurate quantification of CBF and measurement of BOLD signal for functional analysis; the investigation of the physiological basis for brain functional reorganization and better spatial localization of brain activation of

a cognitive task through dual-echo ASL; a description of the start-of-the-art use of IVIM for neurological and neurovascular diseases; an analysis of the impact of IVIM acquisition and analysis parameters to better fit the IVIM measurements, and a pilot study of IVIM applied in patients with brain glioma as a model of the blood-brain barrier disruption.

Keywords: arterial spin labeling, cerebral blood flow, diffusion, functional MRI, intravoxel incoherent motion, perfusion.

Resumo

O cérebro humano consiste de um orgão bastante complexo e especializado, sendo responsável por coordenar a execução das mais diversas funções desempenhadas pelo indivíduo. Para manter esses mecanismos regulados em uma condição normal, o cérebro deve ser continuamente abastecido por oxigênio e nutrientes requeridos para geração da energia necessária para desempenhar tais funções, uma vez que o cérebro não é capaz de armazenar energia. Para manter a entrega de nutrientes constante, o sistema neurovascular é crucial, o que implica em um complexo mecanismo de auto-regulação para evitar quaisquer obstrução em seu caminho. Tendo em vista a optimização da execução das tarefas requeridas, o cortex cerebral é dividido em sub-regiões estruturais, funcionais e vasculares, de modo que o abastacimento do cérebro pelo sangue varia tanto regionalmente quanto temporalmente, a depender do estímulo recebido pelo cérebro e com a demanda de energia requerida, de modo que uma desregulação dessa organização cerebral pode levar às mais variadas doenças.

Imagem por ressonância magnética (IRM) é uma poderosa ferramenta de imagens que possibilita a análise de diversas características do tecido cerebral, tais como estrutura, função, perfusão tecidual, fluxo sanguíneo, difusão das moléculas de água no tecido e muitas outras. Todas essas características podem ser analisadas devido a existencia de inúmeros tipos de mecanismos de constraste nas IRM. Para avaliar a entrega de sangue no tecido cerebral, imagens ponderadas em perfusão sanguínea e difusão molecular são dois dos contrastes recomendáveis, e Arterial Spin Labeling (ASL) e Intravoxel Incoherent Motion (IVIM), imagens ponderadas em persufão e difusão respectivamente, são dois importantes métodos não-invasivos e quantitativos. Além disso, analisando flutuações temporais no fluxo sanguíneo em diferentes regiões anatômicas é possível realizar um estudo das funções cerebrais, o que é chamado IRM funcional (fIRM) e que consiste numa importante modalidade de imagem.

No presente estudo, nós trabalhamos na interface entre o desenvolvimento de métodos de acquisição e análise de imagens bem como na aplicação tanto em sujeitos saudáveis quanto em pacientes. Em termos de aquisição de imagem, trabalhamos na optimização do modo de leitura 3D Gradiente e Spin Eco (3D GRASE) e o efeito do uso de gradientes de compensação de fluxo nas imagens. Para os dados de IVIM, analisamos o efeito de diferentes parâmetros de aquisição nos modelos de análise, com o intuito de optimizar os algorítimos de análise das imagens a fim de uma fácil aplicação na rotina de pacientes com doenças neurológicas e cerebrovasculares. Finalmente, avaliamos a capacidade de ASL no estudo de funções cerebrais, seja no estado de repouso ou durante a realização de tarefas motoras e de linguagem. Para isso, usamos um módulo de leitura duplo eco para as imagens ASL, possibilitando assim a obtenção de parâmetros adequados tanto para a quantificação do fluxo sanguíneo cerebral (CBF), quanto para a análise do sinal que é dependente do nível de oxigenação do sangue

(sinal BOLD). Para isso, começamos com uma tarefa mais simples e robusta, a tarefa motora, para a validação dos modelos utilizados e posteriormente a aplicação de tais modelos em sistemas mais complexos, como o caso das redes cerebrais de linguagem.

Os principais achados desta tese incluem a melhor delimitação do sinal arterial ao usar o módulo de leitura 3D GRASE segmentado e gradientes de compensação de fluxo; a demonstração da viabilidade do ASL com leitura de eco duplo para a medida simultânea da quantificação precisa de CBF e medição do sinal BOLD para análise funcional; a investigação das bases fisiológicas da reorganização funcional do cérebro e melhor localização espacial da ativação cerebral de uma tarefa cognitiva por meio do ASL com eco duplo; uma descrição do estado da arte em IVIM para doenças neurológicas e neurovasculares; uma análise do impacto dos parâmetros de aquisição e análise do IVIM para melhor ajustar as medidas de IVIM e um estudo piloto de IVIM aplicado em pacientes com glioma cerebral como um modelo de ruptura da barreira hematoencefálica.

Palavras-chave: marcação dos spins arteriais, fluxo sanguíneo cerebral, difusão, IRM funcional, movimento incoerente intravoxel, perfusão.

List of Figures

List of Tables

Abbreviations

D^* pseudo-diffusion coefficient 74–81, 83

aBV arterial blood volume 13, 24, 26, 64, 66, 68–71

ADC apparent diffusion coefficient 75, 81–84, 87, 89, 90

ASL arterial spin labeling 13, 23–33, 35–37, 43, 45, 47, 49, 57, 61, 63–69, 71, 73, 74, 79–81, 84–86, 91, 95, 96

ATT arterial transit time 26, 28, 63, 64

BA Brodmann's areas 45, 50, 52–55, 57, 59, 60

BBB blood-brain barrier 23, 25, 26, 33, 63, 69, 73, 79, 82, 84, 85, 96

BC betweenness centrality 51

BOLD blood oxygen level-dependent 23, 24, 31, 32, 35, 36, 39, 42, 43, 46, 47, 49, 57, 59, 60, 95

BS background suppression 28

CASL continuous ASL 27

CB cerebellar network 51

CBF cerebral blood flow 13, 23–27, 31–33, 35–43, 45–55, 57–61, 63, 64, 66, 70, 73, 74, 78–82, 95

CBV cerebral blood volume 23, 24, 26, 32, 36, 73, 74, 78–80

ccBOLD concurrent BOLD 13, 32, 35, 36, 38–40, 42, 47, 49–51, 53–55, 57–60

CMRO2 cerebral metabolic rate of oxygen 23, 24, 32, 36

cSVD cerebral small vessels disease 82, 85

CT computed tomography 25

D diffusion coefficient 74–78, 81, 83, 84

DAN dorsal attention network 51, 54, 60

DCE dynamic contrast-enhanced 26, 73, 79, 80, 84, 91, 96

DE-ASL dual-echo ASL 35–37, 39, 47, 48

DMN default mode network 50–52, 54, 59, 60

DSC dynamic susceptibility contrast 26, 73, 79, 80, 82, 84, 91

DTI diffusion tensor imaging 26, 32

DWI diffusion weighted images 26, 32, 74, 80, 82–84, 86, 87

EPI echo-planar images 29, 30, 32, 33, 37, 41, 48, 63–65, 67, 69, 71

f perfusion fraction 75–84

fASL functional ASL 31–33, 95

FC flow compensation 13, 28, 63, 64, 66, 69–71

FLAIR fluid-attenuated inversion recovery 48

fMRI functional Magnetic Resonance Imaging 23, 31, 36, 43, 45–47, 49, 50, 58, 60, 61, 95

FPN frontal-parietal network 51

GE gradient echo 31–33

GLM general linear model 38, 40, 50

GM gray matter 37

GRASE gradient and spin echo 29, 30, 33, 63–67, 69–71, 95

GTA graph theory analysis 51

HGG high grade glioma 82, 83

ICA independent component analysis 38, 40

ICP intracranial pressure 24

IFG inferior frontal gyrus 50, 52–54, 57, 59, 60

IVIM Intravoxel Incoherent Motion 13, 23–26, 32, 33, 73–93, 95, 96

ktrans water exchange rate 26

LAN language network 51, 54, 60

LD labeling duration 28

LGG low grade glioma 82, 83

M0 proton-density-weighted images 48

MFG medial frontal gyrus 50, 52, 55

MMSE-2EV mini-mental state examination – expanded version 48

MRI magnetic resonance imaging 23–32, 35, 36, 45, 48, 61, 66, 73, 74, 79, 82, 84–88, 91, 95, 96

MT magnetization transfer 27

MTT mean transit time 26, 74, 79, 80

NNLS non-negative least square 87–92

PASL pulsed ASL 27, 28, 70

pCASL pseudo-continuous ASL 13, 27, 29–31, 33, 35, 37, 41, 43, 48, 63, 64, 66, 67, 69, 71, 95

PET positron emission tomography 25, 57, 58, 78

PLD post labeling delay 28, 30, 31, 63–71, 85, 95

pMTG posterior division of the left middle temporal gyrus 50, 52, 53

pSTG posterior division of the left superior temporal gyrus 50, 52

PWI perfusion weighted images 26, 63

RARE rapid acquisition with relaxation enhancement 30

RF radio frequency 26, 27, 29, 30, 35, 63, 65

ROI region of interest 26, 35, 50–52, 54, 59, 83

SAN salience network 51, 54

SAR specific absorption rate 30

SFG superior frontal gyrus 50, 52, 54, 60

SMN sensory-motor network 51, 54

SNR signal-to-noise ratio 28–31, 33, 35, 42, 63, 65, 69, 96

SVF semantic verbal fluency 45–48, 50–54, 57–61

T1 longitudinal relaxation time 26, 28, 37, 49

T2 transversal relaxation time 26, 36, 38, 45, 47, 49, 58

TE time to echo 35–40, 42, 43, 47, 49, 63, 66, 69

te-pCASL time-encoded pCASL 33, 63–65, 69, 71

TR repetition time 29, 31, 63, 65

tSNR temporal signal-to-noise ratio 13, 64, 67–71

VF verbal fluency 45

VN visual network 51

WM white matter 37

Contents

1 General Introduction

Studies on neurovascular diseases are of increasing interest, since according to the World Health Organization, in the top ten causes of death, two are classified as neurovascular (1). Stroke is the second cause, while Alzheimer's disease and other vascular dementias take the seventh place. For this reason, new strategies of diagnosis, treatment, and monitoring related to this class of diseases are in the focus of the scientific community worldwide. In this context, magnetic resonance neuroimaging emerges as an important tool that can be used for the diagnosis and monitoring of such diseases, especially for being a noninvasive alternative to evaluate the patient's condition.

Magnetic resonance imaging (MRI) is a technique of high impact in both research and clinical environment. Among the reasons for such importance, one can highlight the absence of ionizing radiation and the great diversity of imaging contrasts. Specifically to neurovascular diseases, several MRI-based methods are beneficial, such as those weighted in perfusion, molecular diffusion, and angiography (2). All of them can be used separately or even combined to provide a robust set of information.

The choice of the best method to use depends on the specific tissue characteristic that we intend to investigate. For the neurovascular questions, important topics are the blood delivery into the brain tissue, the CBF, water diffusion properties, and blood-brain barrier (BBB) permeability, which may be altered in, e.g., cerebral small vessels disease (CSVD) and Leukoaraiosis (3, 4, 5). Despite the existing methods available in clinical routines to assess blood flow, water diffusion, and angiography, most of them are not quantitative and/or demands the injection of a bolus of exogenous tracer, which might be invasive for the patients. Among all the possibilities, ASL and IVIM appear as two promising options to evaluate the neurovascular system and the delivery of blood to the brain. Furthermore, the combination of these methods with other MRI components, such as crushing gradients, showed interesting results (6, 7, 8, 9, 10).

Another strategy to evaluate patients of neurologic and neurovascular diseases refers to the assessment of brain functionality (11, 12). Several tools can be used for this purpose, such as neuropsychological tests and neuroimaging. Functional Magnetic Resonance Imaging (fMRI) is a very well established tool widely used to assess brain networks and functional connectivity. The gold standard fMRI technique is based on the blood oxygen level-dependent (BOLD) contrast (13), which depends on the variation of the rate between oxi-hemoglobin and deoxi-hemoglobin (14). Although the BOLD contrast provides good results, the use of ASL in functional studies has increased over the last years because of two main reasons. First, while BOLD contrast depends on a complex combination of blood oxygenation, cerebral blood volume (CBV), CBF and the cerebral metabolic rate of oxygen (CMRO2), ASL provides

quantitative information of one physiologic parameter (CBF). Second, ASL has a better spatial specificity to neuronal activity when compared to BOLD.

Therefore, the present study aimed to contribute with the improvement of acquisition methods and analysis models for quantitative MRI measurements, specifically brain perfusion and diffusion information through ASL and IVIM methods. We also worked on advanced applications of functional ASL, reporting its benefits compared to a traditional method as the BOLD signal analysis. The next sections of this chapter will cover the general basis necessary to follow our results and a description of our objectives.

1.1 Motivations: from vessels to brain

The human brain is the most complex organ, responsible for coordinating all the functions performed by the subject. In order to keep its mechanism properly working, the supply of oxygen and nutrients through the arterial blood is crucial, since the brain tissue is not able to store enough energy. This necessity of continuous delivery of blood requires a highly complex mechanism of coupling between the vascular system and the brain tissue, whose auto-regulation is vital for a normal neurological condition.

Some physical models based on physiological parameters are proposed to measure, monitor, and explain this high-complex blood-brain coupling (Figure 1). Such parameters are the CBV, aBV, CBF, CMRO2 and intracranial pressure (ICP) (15). All of them are directly or indirectly related to each other such as the deregulation of one can compromise the entire system, possibly leading to a disorder condition.

Figure 1 – The neurovascular coupling

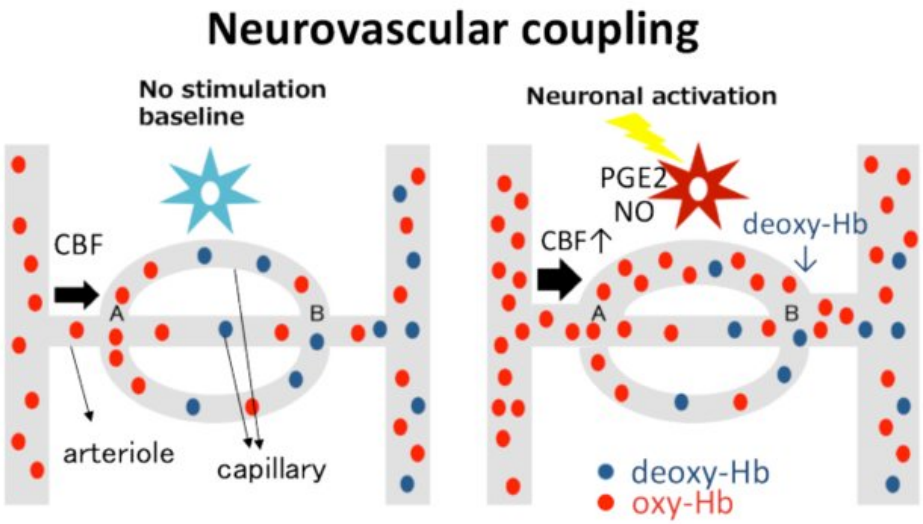

The neurovascular coupling mechanism (16).

Among all the mentioned parameters, the CBF plays a central position in the auto-

regulation mechanism. While the brain represents about only 2% of total human body weight, it demands an amount of 12 to 15% of total cardiac output (17, 18). Therefore, CBF needs to remain approximately constant over time, which implies in adjustment in the other parameters according to changes in the metabolism and external conditions. Several conditions lead to changes in CBF, being both healthy or pathological. In a healthy adult, CBF value in baseline varies from 60 to 80 ml/(100g of tissue)/min, but it shows regional and temporal fluctuations according to the performance of a task by the person. It is also known that changes in CO2 and O2 partial pressure in the blood lead to vasoconstriction or vasodilatation. Finally, disruption and deregulation of BBB (Figure 2) can also cause an impact in regional CBF, which might result in some diseases, especially the Alzheimer's disease and other vascular dementias (19).

Contextualized the physiological importance of the CBF, it is not difficult to understand why measuring it is so relevant. In the next section, there will be a discussion of the importance of MRI-based methods to measure CBF. Particularly, we will focus on two noninvasive methods: ASL and IVIM.

Figure 2 – Blood-brain barrier

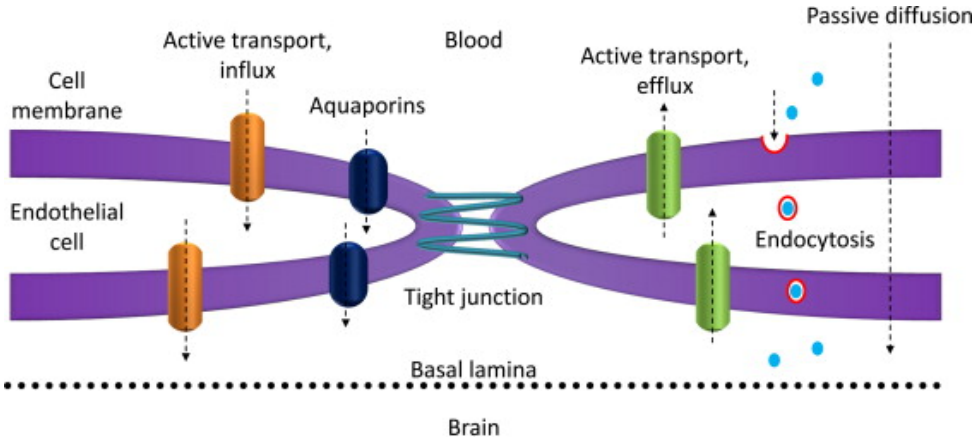

The water transfer mechanism across the blood-brain barrier (19).

1.2 Magnetic resonance imaging methods to measure blood flow - brain perfusion properties

Magnetic resonance imaging is a powerful imaging modality that takes advantage of the electromagnetic properties of the tissues. Despite other useful techniques, such as X-rays, computed tomography (CT) and positron emission tomography (PET), the use of MRI has been preferred, due to at least two main reasons: (1) it does not require the use of ionizing radiation and (2) the possibility to explore a big range of different imaging contrast, which may be chosen according to the necessity.

Among all the several existing contrast mechanisms, three of them suit better the measurement of the blood flow-brain coupling: perfusion weighted images (PWI), diffusion weighted images (DWI) and MR angiography. All of them are on the spins' mobility. However, while MR angiography is optimized to image the vascular compartment, PWIs and DWIs are focused on spins movements in the brain tissue.

The concept of PWIs is based on the labeling of spins or the injection of a tracer in the blood. In dynamic susceptibility contrast (DSC) and dynamic contrast-enhanced (DCE) methods, the kinetic tracer is exogenous, intravenously injected in the subject (20, 21, 22). The contrast agent then travels until the region of interest (ROI), where it changes relaxation properties with the tissue, changing the image contrast. In DSC, by exploring changes in the transversal relaxation time (T2), it is possible to estimate CBF, CBV and the mean transit time (MTT). On the other hand, DCE explore changes in longitudinal relaxation time (T1) to measure the water exchange rate (ktrans) mainly. However, besides DSC and DCE are the two most commonly used methods in the clinical environment to assess brain perfusion, arterial spin labeling is a PWI method that has gained more attention since it enables the measurement of quantitative values of CBF, aBV, and arterial transit time (ATT) noninvasively (23). Furthermore, more complex ASL methods are being developed to measure regional angiography and CBF, BBB permeability and oxygen extraction (24, 7, 25).

DWI is an imaging modality based on the diffusion of water molecules in the biological tissue. Due to its high sensibility to detect biological changes in the tissue characteristics, such as abnormal blood irrigation, altered cellularity level, and tissue death, DWIs significantly revolutionized the use of MRI for some diseases, e.g., stroke and brain tumor. DWIs are also the basis for a popular model of structural analysis nowadays, the diffusion tensor imaging (DTI) model, which allows the tractography reconstruction to study the brain fibers (26, 27, 28). Alternatively, it is also possible to extract perfusion information from DWI by exploring a method named intravoxel incoherent motion IVIM, which is based on multiple levels of diffusion movement restriction (29, 30).

The next two sections will cover the basis for understanding the two main methods explored during the evolution of this study, arterial spin labeling and intravoxel incoherent motion.

1.3 Arterial Spin Labeling

Arterial spin labeling (ASL) is a PWI method that uses the water molecules of the arterial blood as an endogenous tracer. A bolus of blood is tagged in a strategic position (Figure 3). This region is named labeling plane and is chosen where the main feeding arteries are relatively straight and perpendicular to the labeling plane. The bolus of blood at the labeling plane is magnetically labeled through the application of an radio frequency (RF)

pulse. There are three main classes of ASL methods according to the labeling strategy, but for all of them, a pair of images is acquired. When the labeling pulse is applied, the image acquired is named labeling image. Then, the control image is acquired at the same position as the labeling one, but without the application of any labeling pulse. The difference between the control and labeling images is proportional to the CBF (31, 32, 33).

Figure 3 – Arterial Spin Labeling

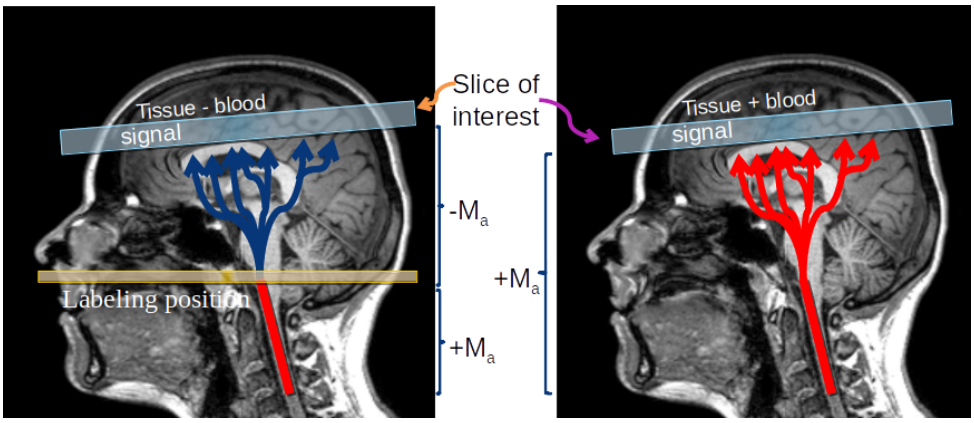

Arterial spin labeling: control and label images. Source: the author.

In pulsed ASL (PASL), a short-time pulse is applied, and the labeling plane is large, so a significant amount of blood is labeled to guarantee enough labeled blood at the imaging slab. However, the labeling efficiency in PASL is lower than for the other ASL methods. For continuous ASL (CASL), the labeling efficiency is higher in comparison with PASL. It is achieved by labeling a short-width labeling plane but for a longer time. The drawbacks of using a continuous RF labeling pulse are the accumulation of magnetization transfer (MT) effects and the mismatch when switching the head coil from RF pulse generation mode to receptor mode. This second drawback could be solved by using a dedicated labeling coil, but this hardware demand is not clinically accessible and would require a custom MRI system (34, 35, 36, 37, 38).

The third class of ASL is the pCASL. In this category, the labeling plane uses the same configuration as in CASL, but the labeling is achieved using a long train of short-duration RF pulses. This strategy keeps the labeling efficiency comparable to the CASL but avoiding its major side effects. In pCASL labeling train, the polarity of two subsequent RF pulses is alternated for the control condition and always remains positive for the labeling condition. There is also a subdivision in pCASL according to the gradient configuration in the labeling train of pulses. For balanced pCASL, the gradient configuration for two subsequent pulses remains constant, but the mean gradient value is not zero. On the other hand, for unbalanced pCASL, the mean gradient for two subsequent pulses is zero, but the gradient configuration between them is not the same (39, 40).

Due to the advantages listed before, pCASL has been recommended for research and

clinical uses, besides new designed ASL sequence are being optimized based on the PASL, e.g., the velocity selective ASL. (41). Despite ASL pulse sequence is composed of two main blocks, i.e., the preparation and the readout, several elements have been added to the pulse sequence in order to obtain images with higher signal-to-noise ratio (SNR), or to extract different information than the traditional ASL outputs. Over the last decade, a large amount of new ASL pulse sequence designs has been proposed through the different combination of some MRI elements. The numerous options of acquisition strategies became a hindrance to the dissemination of ASL in the clinical routine. Therefore, a paper with the consensus recommendation for clinical applications of ASL was published (31). Next, there is a short description of the major elements used in this study.

- Labeling duration (LD): is the duration of the labeling train of pulses. Optimally is defined according to T1 value (around 1800 ms) so that when these values are comparable, the ASL image SNR is higher.

- Post labeling delay (PLD): is the time interval between the end of ASL labeling and the start of the readout. It is calculated according to the arterial transit time, and therefore it varies among subjects and conditions, as aging and diseases. Traditionally, a single PLD is used, which is enough for several applications. However, a multi-PLD approach is preferred for an application where the transit time is not known, or to analyze the evolution of the ASL signal from the brain arteries to the tissue and obtain ATT maps (42, 43).

- Background suppression (BS): the ASL perfusion maps results from the subtraction of two images (control - label)and therefore its SNR is intrinsically low. Every one second of blood flow only 1% of the gray matter water is replaced by the new bolus of blood. Subject's motion during the acquisition also hampers the removal of the static brain tissue when the control - label subtraction is performed. Through the application of one or more saturation selective pulses (44, 45), it is possible to minimize the background signal for both control and label images, without compromising the subtracted image correspondent to the perfusion signal. This approach is not a time consuming element and can significantly improve the SNR of ASL maps (46, 47).

- Flow Compensation (FC): without flow compensation, the measurement of flowing spins can lead to dephasing effects at the time of echo, when the image is acquired. The dephased spins might have a direct impact in the visualization of the intravascular signal by suppressing it signal or adding some blurring to the interface between the vessel and brain tissue. A bipolar gradient can be added in a preparation module of the pulse sequence to minimize this effect, which also named gradient-moment nulling. This gradient's lobes are designed so that its effects to the static spins is null, but reduce the dephasing for the moving spins (48).

- Readout approaches: the choice of the readout module plays an important role in the resulted image SNR. Several new strategies have been optimized to get higher SNR in a short time interval. However, two main readout approaches are the most commonly used:

  – 2D multi-slice echo-planar images (EPI): it is a standard readout available in the MR systems that provides reasonable good ASL maps, besides not providing the highest SNR possible.

  – 3D gradient and spin echo (GRASE) (49): it is the recommended readout approach for pCASL, since it provides optimal background suppression by only using a single excitation per repetition time (TR) and results in a higher SNR compared to 2D EPI (31).

1.3.1 3D GRASE readout

The 3D Gradient and Spin Echo (GRASE) readout is an alternative approach to the EPI readout. Its pulse sequence consists of a train of RF refocusing pulses, combined with a train of alternating readout gradient polarity, similar to the EPI readout gradients. By this combination of RF pulses and readout gradients, the idea is to rephase the magnetization enabling the occurrence of several echoes and, consequently, the acquisition of several MRI signals with the application of only one RF excitation pulse (Figure 4) (50).

Figure 4 – 3D GRASE Readout

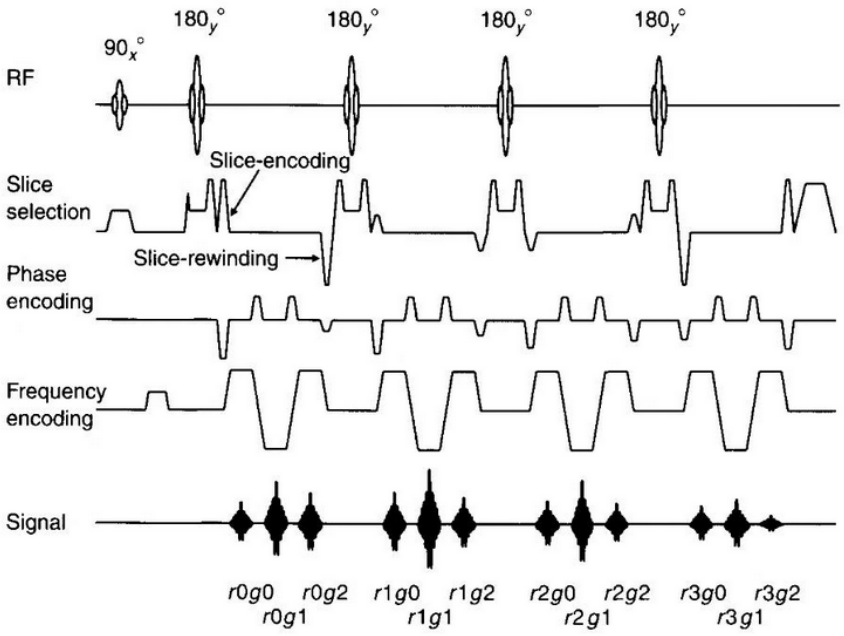

3D GRASE readout pulse sequence. Multi RF excitation pulses are combined with a train of alternating polarity readout gradients and a single excitation pulse. (51)

Although the EPI readout is a faster strategy, by acquiring several k-space lines with a single refocusing RF pulse or with a single refocusing through gradients, a large amount of phase is accumulated by the off-resonance spins. The best way to avoid phase accumulation would be the acquisition of one echo per refocusing pulse, in an approach called rapid acquisition with relaxation enhancement (RARE). However, the application of a high number of refocusing pulses increases significantly the specific absorption rate (SAR), which compromises its uses in a MRI pulse sequence with high SAR, as the ASL pulse sequence. The GRASE readout is in a half-way between the EPI and RARE readouts, by employing multiple refocusing pulses, but in a different way than in RARE (Figure 5).

Figure 5 – Phase accumulation by off-resonance spins

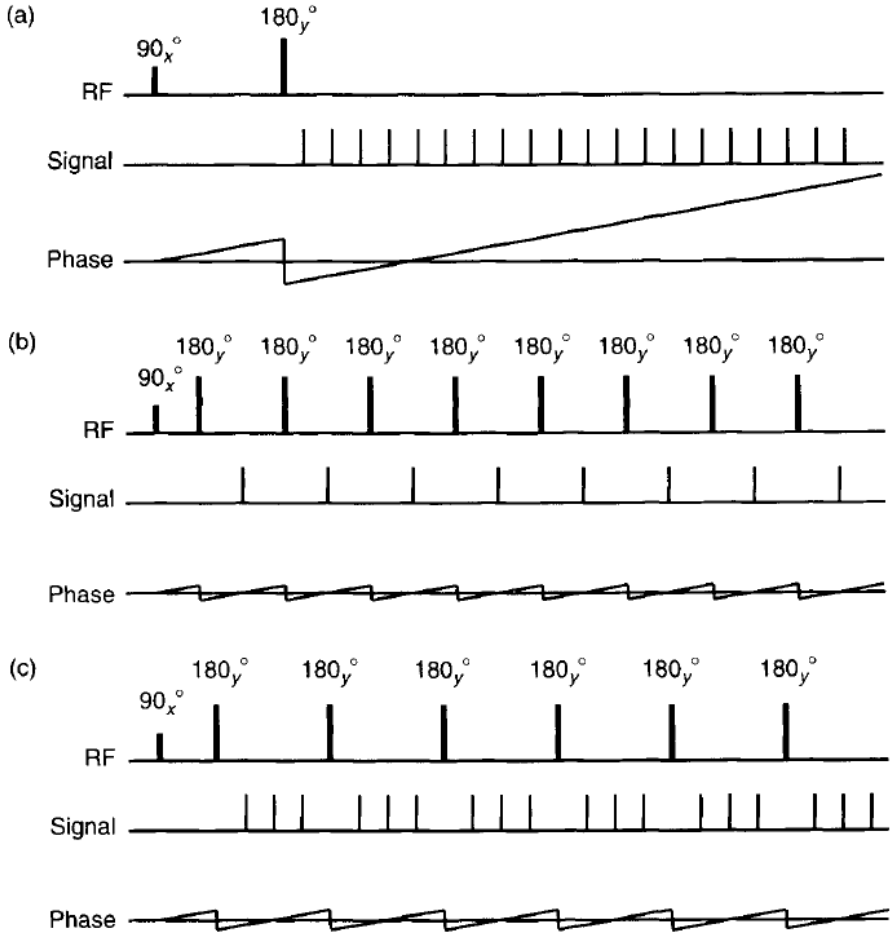

Phase accumulation by off-resonacne spins for (a) EPI, (b) RARE and (c) GRASE readouts. (51)

1.3.2 Time-encoded arterial spin labeling

For multi-PLD pCASL, traditionally, several images are acquired repeatedly for each one of the multiple PLDs used. It is necessary to increase the low SNR of ASL subtracted maps by taking the average of all repetition acquired. In this approach, the same information is

acquired several times, which makes the pulse sequence inefficient and the total acquisition time for the whole brain inadequate for clinical routine.

Gunther proposed a temporal encoding to the ASL labeling process to overcome this drawback (52). In this new approach, a bolus of blood is split into different blocks that can be both a label or a control block. The number of repetitions and blocks are defined according to a Hadamard matrix of rank H, resulting in (H - 1) blocks and H repetitions (53). Each Hadamard matrix line is a different bolus (ASL repetition) composed of a different combination of control and label blocks. This combination of blocks is designed, such as each Hadamard columns (or each sub-bolus) is composed of the same number of control and labels blocks. The Hadamard matrix is defined before data acquisition and must be used to decode the ASL images during the subtraction process.

Every sub-bolus will be read after waiting for a different PLD since the labeling duration is different across all the sub-bolus. In an acquisition of a pCASL data set using a Hadamard encoding strategy, there will be acquired a total $H/2 * (H-1)$ ASL pairs, or (H-1) PLDs and (H/2) repetitions by labeling only H bolus of blood. It is a very appealing approach when the hemodynamic information of the inflow blood is needed, or when it is desired to follow the blood passing from the vascular tree to the brain tissue (54, 24).

1.4 Functional Arterial Spin Labeling

In functional magnetic resonance imaging, the gold-standard method is based on the BOLD contrast. Among the reasons to use BOLD for fMRI, its high SNR, good temporal resolution and easy implementation in MRI systems are maybe the three most convincing arguments (55, 56, 57). Furthermore, the gradient echo (GE) is very sensitive to changes in the oxygenation level temporally, which is the basis for functional analysis.

The intrinsically low SNR of ASL maps requires the acquisition of multiple pairs of control-label images to calculate further the average of the subtracted images resulting in improved-SNR CBF maps. Exploring the signal fluctuation pair-by-pair in the temporal series, it is also possible to perform functional analysis in ASL data (58). The basis for a functional ASL (fASL) study is pretty similar to the BOLD basis since, for both methods, the analysis is based on temporal changes in blood flow, directly or indirectly.

There are some clear drawbacks of using ASL for fMRI study when directly compared to the BOLD approach. First, the TR of ASL is usually at least two times greater than it is for BOLD, which increases total acquisition time or limits the number of time points and increases the interval between two-time points data making it more susceptible to physiological changes, e.g., cardiac and respiratory trigger. There is also a disadvantage in the SNR, which is lower for ASL. Nonetheless, despite the drawbacks, there are physiological characteristics of the ASL that make it interesting to be explored. While the BOLD signal results from a complex

dependency among CBF, CMRO2 and CBV (59), for fASL the analysis depend only on one quantitative parameter (CBF). The advantage in using CBF for functional measurement is its more direct relation to neuronal activation than the BOLD signal (17, 60). Moreover, ASL signal comes from the capillary bed, which may lead to a spatial localization closer to the activation site (58, 61, 62, 63, 64).

The fASL can be performed in two different approaches, based on CBF fluctuations or by exploring the BOLD contamination of ASL data. The CBF approach consists in analyzing the CBF value temporally, pair-by-pair, and then proceed to the statistical analysis. On the other hand, the exploration of BOLD contamination of ASL images, or the ccBOLD effect, takes advantage of susceptibility effects in the acquired image (typical of a BOLD signal). Despite this susceptibility contamination is not desired for CBF quantification, it is hardly difficult to avoid during data acquisition, especially when using a GE-EPI readout. Therefore, it can be explored to obtain simultaneous information about CBF and BOLD effect.

1.5 Intravoxel Incoherent Motion

DWI takes advantage of the restrictions imposed to the water molecule movement in the biological tissue (65), which can be measured by the application of magnetic field gradients in an MRI acquisition (66, 67). Although the general pulse sequence to acquire a DWI is relatively simple and readily available in any MRI scanner, its use revolutionized the application of MRI to several different diseases, making DWI widely spread in clinical routine all over the world. Such versatility of DWI applications is because several intracranial diseases contribute to diffusion restrictions (68, 69).

Besides its simplicity in pulse sequence design, diffusion can also be explored in more complex models. A very typical diffusion advanced application is the DTI, one of the models to analyze brain structure through the tractography (70, 71). Another advanced DWI application is the intravoxel incoherent motion IVIM, which explores different restriction levels of the water molecules in the biological tissue to split the diffusion decay in MRI signal into a summation of contributions (72). According to its model, the main contribution to the total diffusion decay are the water molecules randomly moving in the biological tissue and those that are randomly moving within the blood system (73).

The motivation to split the total signal into different contributions is to extract pure diffusion maps of the static tissue and simultaneously get perfusion-related information. It is achieved by using a range of b-values (explained later) and the fitting of the signal decay with a multi-exponential model. The outputs of this model are the diffusion coefficient for the static tissue and the perfusion fraction, which represents the water molecules in a flowing movement. Unexpected values for perfusion fraction may indicate some abnormality in the blood flow - brain tissue coupling, while alterations in the diffusion coefficient mean

altered tissue restriction to water diffusion, typical of neurological diseases. Furthermore, the correlation between the different IVIM outputs are also useful to some application, e.g. glioma grading (74), and combining IVIM with ASL has been studied as a tool to measure the BBB permeability (7).

The complete description of the IVIM method and its main applications in neurological and cerebrovascular diseases will be presented in chapter 5.

1.6 Objectives

1.6.1 General objectives

This thesis aimed to perform image acquisition optimization, develop methods for image analysis and investigate advanced applications to obtain clinical relevant neurovascular information. The focuses were ASL and IVIM.

1.6.2 Specific objectives

The specific goals of this thesis are listed below. For each goal, we performed a study and wrote a manuscript. Therefore, each study is presented in a paper format in each chapter.

- Perform the optimization of 3D GRASE readout for time-encoded pCASL (te-pCASL) and analyze the effect of segmentation number in the temporal SNR for single-shot, two-shot and three-shot acquisitions as well as compare the results with the multi-slice GE-EPI readout. (Chapter 2).
- Evaluate the effect of gradients for flow compensation in delineating the intra-vascular signal in time-encoded pCASL. (Chapter 2).
- Analysis and validation of the dual-echo readout for pCASL for CBF quantification and functional analysis during the execution of a robust motor task. (Chapter 3).
- Indicate the benefits of fASL for the advanced application of measuring functional and physiological changes in brain organization when executing a semantic verbal fluency task and the comparison to the resting-state condition. (Chapter 4).
- Review the concepts of acquisition strategies and analysis models for IVIM, as well as an overview of the state-of-the-art in its applications, focused on neurological and neurovascular diseases. (Chapter 5).
- Investigate the critical parameters to execute the non-negative least square model to fit the IVIM data using a simulated signal and healthy subjects data. (chapter 6).

2 Dual-Echo Arterial Spin Labeling for Brain Perfusion Quantification and Functional Analysis

2.1 Abstract

Arterial Spin Labeling ASL is a noninvasive MRI-based method to measure cerebral blood flow (CBF). Recently, the study of ASL as a functional tool has emerged once CBF fluctuation comes from capillaries in brain tissue, giving a more spatially specific response when compared to the standard functional MRI method, based on the blood oxygenation level-dependent BOLD contrast. Although the BOLD effect could be desirable to study brain function, if one aims to quantify CBF, such effect is considered contamination that can be more attenuated if short time to echo (TE) value is used in the image acquisition. An approach that provides both CBF and function information in a simultaneous acquisition is the use of a dual-echo ASL (DE-ASL) readout. Our purpose was to evaluate the information provided by DE-ASL regarding CBF quantification and functional connectivity with a motor task. pCASL of twenty healthy subjects (age: 32.4 ± 10.2 years, 13 male) was acquired at a 3T scanner. We analyzed the influence of TE on CBF values and brain connectivity provided by CBF and concurrent BOLD (ccBOLD) time series. Brain networks were obtained by the general linear model and independent component analyses. Connectivity matrices were generated using a bivariate correlation (Fisher Z values). No effect of the sequence readout, but a significant effect of the TE value, was observed on gray matter CBF values. Motor networks with reduced extension and more connections with important regions for brain integration were observed for CBF data acquired with short TE, proving its higher spatial specificity. Therefore, it was possible to use a dual-echo readout provided by a standard commercial ASL pulse sequence to obtain reliable quantitative CBF values and functional information simultaneously.

2.2 Introduction

Arterial Spin Labeling (ASL) is a magnetic resonance perfusion-weighted technique with the advantage of not using an exogenous contrast agent. It is achieved by using the arterial blood as an endogenous tracer, which is magnetically labeled (label image) through the application of radiofrequency (RF) pulses. Such pulses are applied in a strategic position (labeling plane) so that the magnetization in the region of interest (ROI) is changed compared to a non-label situation (control image) (75, 23). With this set of images, cerebral blood flow (CBF) is estimated from the subtraction between control and label images. Due to the ASL intrinsic low SNR, there is the necessity of acquiring multiple control-label pairs, and the CBF map is the mean of all subtractions executed (76). On the other hand, the temporal series

of ASL images allows the evaluation of CBF fluctuations over time, from which functional information can be estimated (77, 78, 79).

Although in functional magnetic resonance imaging (fMRI) the blood oxygen level-dependent (BOLD) contrast is mainly used, applications of ASL in functional studies have increased over the last years mainly because of two reasons. First, while BOLD contrast depends on a complex combination of blood oxygenation, cerebral blood volume (CBV), CBF, and metabolic rate of oxygen (CMRO2), ASL provides quantitative information of one physiologic parameter (CBF) (60, 80). Second, ASL has a better spatial specificity to neuronal activity when compared to BOLD (58, 63, 64, 81, 62). Moreover, ASL combined with dual-echo readout (DE-ASL) is an interesting approach to optimize the acquisition aimed at both CBF quantification and functional analysis (82). Images acquired using short echo time (TE) are more weighted in perfusion, while the use of longer TE increases the effect of transversal relaxation (T2*), typical of the BOLD contrast (79, 83).

Some previous reports used DE-ASL to evaluate the correlation between CBF time series and the ccBOLD signal, either in resting state or with a visual/motor task condition, and analyze the functional connectivity (84, 61, 85, 86, 87). Lu and colleagues showed the influence of BOLD contamination on the temporal dynamics of ASL curve but did not analyze its effects on functional connectivity (61). Regarding acquisition and analysis, Ghariq and colleagues investigated some specific aspects of the signal and suggested the use of background suppression to reduce BOLD contamination and to increase CBF sensibility (84). Moreover, Storti and colleagues recently reported the contribution of ASL to understand how CBF is related to functional connectivity (85) and the feasibility of DE-ASL to analyze brain function (86). However, they did not evaluate the method regarding the direct effect of TE in CBF quantification, ccBOLD and CBF networks, and functional analysis.

Therefore, we aimed to evaluate the CBF quantification with DE-ASL in comparison with standard ASL acquisition, analyze the similarity of networks between CBF and ccBOLD and between each TE used, and verify changes in brain connectivity for different TE values.

2.3 Methods

2.3.1 Subjects

Twenty healthy participants (age: 32.4 ± 10.2 years, 13 male) were scanned on a 3T Achieva MRI Scanner (Philips Healthcare, Best, Netherlands) equipped with a 32-channel receive head coil. All subjects gave their written informed consent after the ethics committee of the institution approved the study.

2.3.2 Image Acquisition and Protocol

DE-ASL data were acquired using a 2D echo-planar imaging (EPI) readout and a pseudo-continuous labeling (pCASL) scheme with the following parameters: TR = 4000 ms, TE1/TE2 = 9/28 ms, labeling duration/postlabeling delay = 1450/1550 ms, 20 slices, slice thickness = 5 mm, spatial resolution = 3.75 x 3.75 mm^2, FOV = 240 x 240 mm^2, flip angle = 90°, and total acquisition time of 4.26 min. For conventional single-echo pCASL, the same parameters were used for both TE values (9 and 28 ms). No background suppression was used. In addition, a structural 3D gradient-echo T1-weighted scan was performed with TR = 7 ms, TE = 3.2 ms, FOV = 240 x 240 mm^2, 180 slices, slice thickness = 1 mm, spatial resolution = 1 x 1 mm^2, flip angle = 8°.

The experimental protocol was a block design paradigm alternating rest and right-hand finger tapping. Each block had duration of 32 seconds (8 volumes), totaling four blocks of rest and four blocks of motor task. The command to the subject to start or stop the task was shown in a monitor: red screen during rest blocks and green screen for the task blocks.

2.3.3 Image Processing

Imaging preprocessing was performed using local scripts in MATLAB (MathWorks, Natick, MA) in combination with Statistical Parametric Mapping (<SPM12,http://www.fil.ion.ucl.ac.uk/spm/software/spm12/>). Structural T1-weighted images were used for segmentation and obtaining the gray matter (GM) and white matter (WM) masks. For ASL images, we adapted scripts from ASLtbx (88) performing the following steps: motion correction, coregistration to anatomical image and masks, temporal filtering, and spatial smoothing through the application of an isotropic Gaussian kernel (FWHM = 4 mm for CBF quantification and FWHM = 6 mm for functional images).

2.3.4 CBF Quantification

Perfusion maps were generated by the subtraction of control and label images. For basal CBF analysis, we used the sync subtraction, while for functional analysis we performed a running pairwise subtraction to increase the number of perfusion images (89). Quantification was based on the General Kinetic Model (60) using the following parameters: blood longitudinal relaxation time T1 = 1650 ms; labeling efficiency = 0.85; blood/tissue water partition coefficient (GM/WM) = 0.98/0.84 g/mL; tissue T1 (GM/WM) = 1020/770 ms calculated using a Look-Locker sequence (90). Finally, CBF time series and mean CBF map were normalized to MNI standard space (resolution = 2 x 2 x 2 mm3; matrix size: 79 x 95 x 79).

2.3.5 General Linear Model

We ran a general linear model (general linear model (GLM)) analysis using FSL (<http://fsl.fmrib.ox.ac.uk/fsl/fslwiki>) to assess the differences regarding CBF and ccBOLD networks between TE values. Both CBF and ccBOLD information were obtained using FEAT to preprocess and perform the statistical analysis according to the following steps: subject motion correction (MCFLIRT (91)), brain extraction, spatial smoothing filtering (FWHM = 5 mm), temporal filtering, coregistration to MNI atlas, whitening, GLM analysis according to experimental design, and finally the clustering analysis. The obtained networks were spatially compared by the Dice Similarity Coefficient (DSC) (92) using local scripts in MATLAB.

2.3.6 Independent Component Analysis Networks

The functional analysis was performed using CONN Toolbox (93), in which CBF time series were detrended and filtered with a low-pass filter ($f < 0.07$). To remove the signal from white matter and cerebrospinal fluid we used principal component analysis (PCA) with the CompCor algorithm. Then, we ran the independent component analysis (independent component analysis (ICA)) algorithm setting 20 individual components previously.

Next, we selected the motor network that resulted from ICA from CBF maps obtained with each echo to evaluate the difference between them regarding spatial similarity and functional connectivity. For spatial similarity, we used the DSC calculated in MATLAB. We also analyzed the difference between groups in Z scores and performed a one-sample t-test using the R Project (94) to obtain a p-value matrix considering only significant differences ($p < 0.05$, corrected for multiple comparisons using Bonferroni-Holm method). Finally we evaluated the differences in functional connectivity between the two CBF time series.

2.4 Results

2.4.1 CBF Comparison between Single- and Dual-Echo pCASL

We compared the mean CBF values for gray matter acquired with different sequences and TEs to evaluate how such parameters affected the CBF quantification. Figure 6 shows CBF maps obtained with standard single-echo and dual-echo readouts. No significant difference in gray matter CBF values was observed for different readouts but the same TE. Mean values for TE1 were 35.50 ± 11.23 mL/100g/min and 36.08 ± 9.45 mL/100 g/min, respectively, for single- and dual-echo acquisitions ($p = 0.95$). For TE2 mean values were 21.84 ± 8.15 mL/100 g/min and 22.16 ± 6.74 mL/100 g/min, respectively, for single- and dual-echo acquisitions ($p = 0.95$). However, significant differences were observed when comparing CBF for different TE values but the same readout ($p < 0.05$), due to the T2 decay present in images acquired with longer TE value.

Figure 6 – Cerebral blood flow quantification

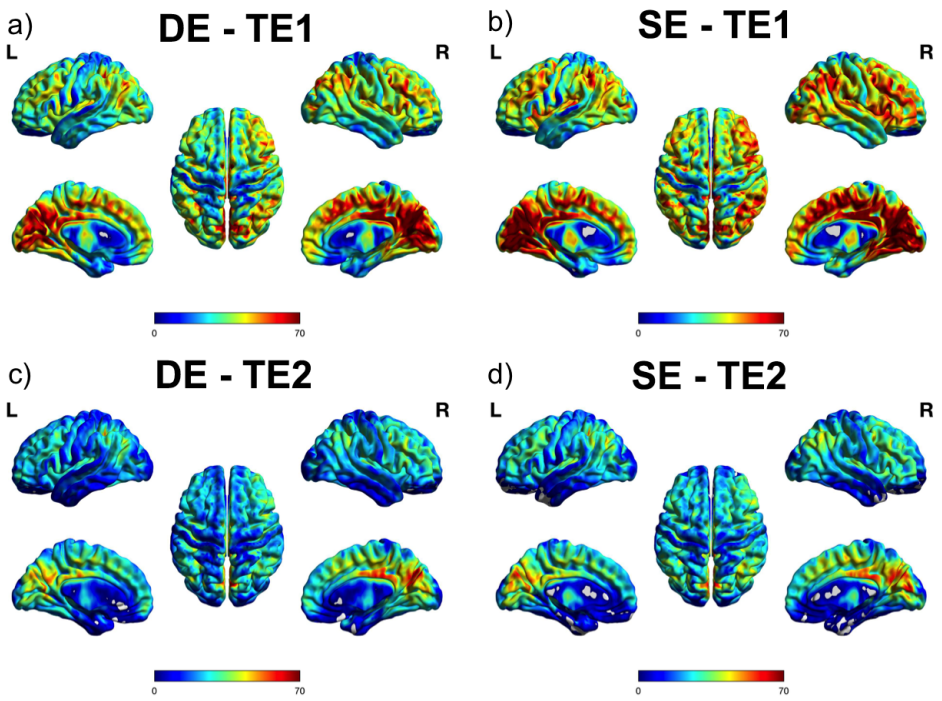

CBF maps obtained with different readouts (DE: dual-echo, SE: single-echo) and TE values: (a) DE, TE1 = 10 ms; (b) SE, TE1 = 10 ms; (c) DE, TE2 = 28 ms; (d) SE, TE2 = 28 ms. Color bar shows CBF range in mL/100 g/min. Source: the author.

Considering only the motor cortex, for TE1, CBF values were 41.58 ± 12.61 mL/100 g/min and 36.46 ± 14.21 mL/100 g/min, respectively, for single- and dual-echo acquisitions (p = 0.48). And for TE2, CBF values were 28.28 ± 8.22 mL/100g/min and 27.38 ± 9.69 mL/100g/min, respectively, for single- and dual-echo acquisitions (p = 0.88).

2.4.2 GLM Analysis

Figure 7 shows the motor network of normalized CBF and ccBOLD. We only assessed the results obtained with the DE-ASL since they were acquired during the same scan, and no variability resulted due to differences in task performance. The spatial similarity between them was higher for TE1 (DSC = 0.4, Figure 7a) than for TE2 (Figure 7b, DSC = 0.25). Moreover, when comparing CBF (Figure 7c) or ccBOLD (Figure 7d) network for both TE values, we observed a higher number of activated voxels for longer TE due to the higher BOLD contamination in the signal. It increases the sensitivity of the method to detect brain activation but decreases its spatial specificity. Such contamination can be seen on CBF time series for the longer TE. Figure 8 shows the mean CBF time series for all voxels of the motor network activated by the finger-tapping task normalized to the mean CBF of first rest condition block, considering all subjects.

Figure 7 – Activation maps for CBF and ccBOLD

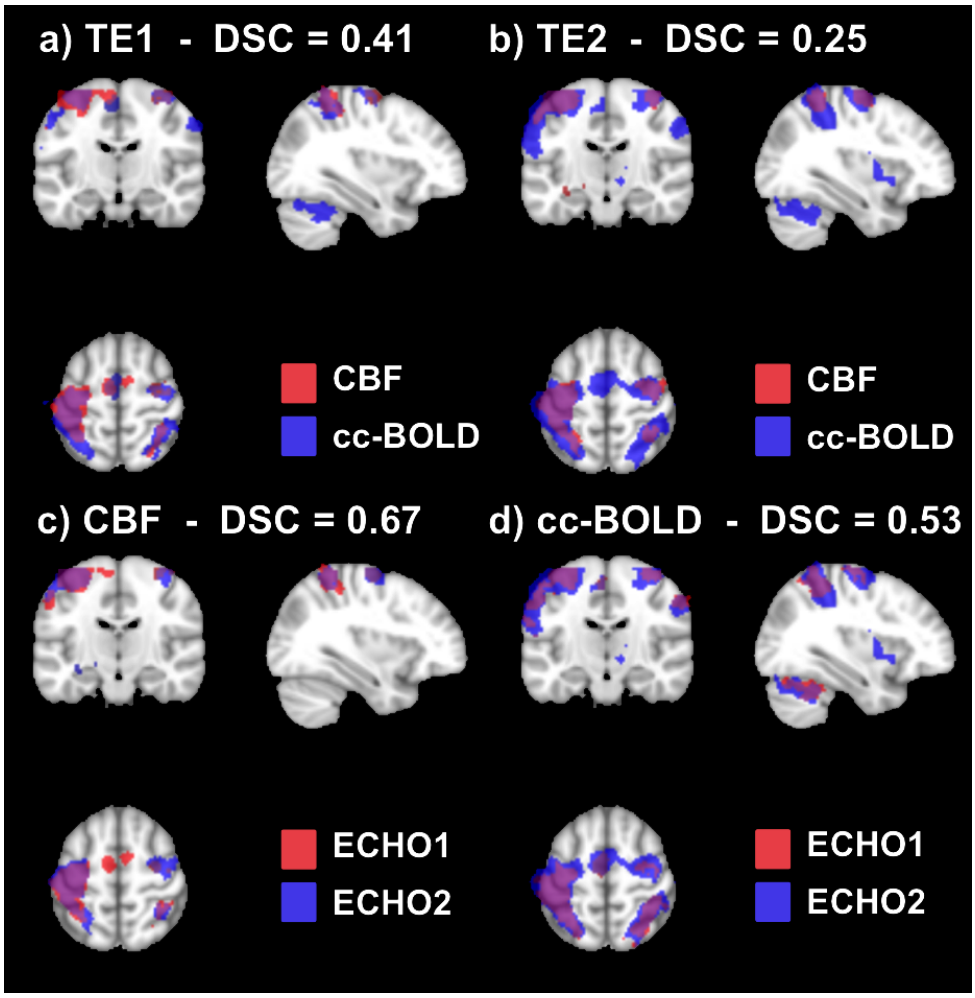

Comparisons of GLM results for the motor networks obtained with dual-echo readout: (a) CBF versus ccBOLD for TE1;(b)CBF versus ccBOLD for TE2;(c)TE1 versus TE2 for CBF networks; and (d) TE1 versus TE2 for ccBOLD networks. DSC: Dice Similarity Coefficient. Source: the author.

2.4.3 ICA Networks

For both TE values, in a dual-echo acquisition, ICA was able to identify the following networks: motor, auditory, default mode network (DMN), visual and executive control network (ECN). A comparison of the motor network obtained for each TE showed a spatial similarity of 30% (DSC = 0.30). Table 1 shows how that difference in similarity is distributed over the anatomical regions by the different number of activated voxels in the primary motor cortex.

Figure 9 shows the connectivity patterns for the motor network obtained with both TE values of the dual-echo readout. Although for TE2 (Figure 9b) the connectivity within the motor network was stronger than for TE1 (Figure 9a), some connections with other brain regions, such as the precuneus, were not identified for the longer TE. Moreover, the correlation between right precentral and postcentral gyri was statistically significant ($p < 0.05$, FDR corrected) when comparing data of both TE values.

Figure 8 – CBF time-series for TE1 and TE2

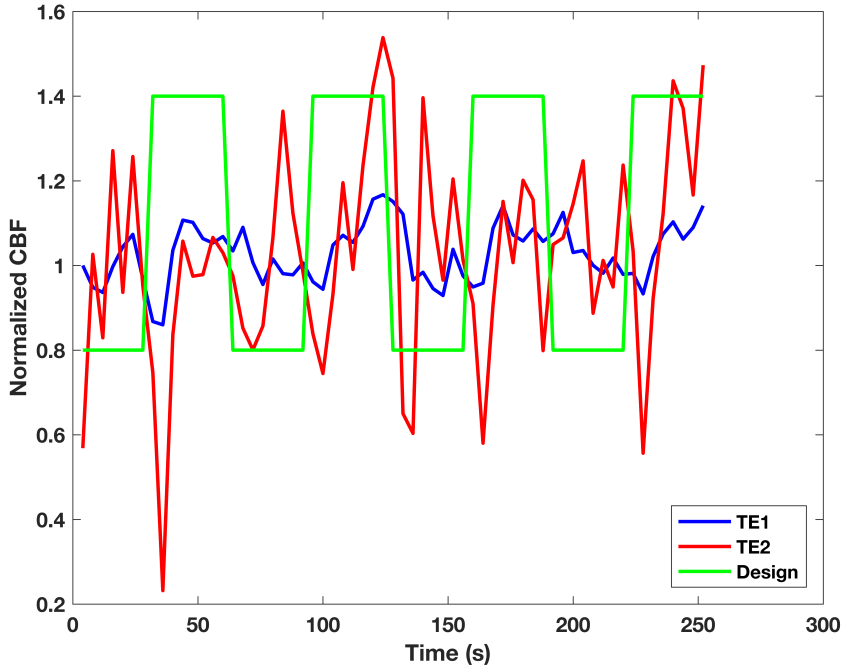

CBF time series normalized to the mean CBF of the first rest condition block for TE1(blue) and TE2(red). The experimental block design is shown in green. Source: the author.

Table 1 – Main anatomical regions activated during the finger-tapping task and the corresponding number of activated voxels.

TE_1	Number of voxels	TE_1	Number of voxels
Left Precentral Gyrus	418	Left Precentral Gyrus	431
Left Postcentral Gyrus	407	Left Postcentral Gyrus	500
Right Precentral Gyrus	384	Right Precentral Gyrus	489
Left Superior Parietal Lobule	292	Left Superior Parietal Lobule	281
Right Postcentral Gyrus	265	Right Postcentral Gyrus	176
Right Superior Parietal Lobule	169	Right Superior Parietal Lobule	241

2.5 Discussion

The acquisition of DE-pCASL is an interesting strategy to acquire quantitative CBF and functional network information simultaneously. To guarantee that CBF is measured with the same precision as in standard pCASL scheme, we compared the results of CBF quantification for both readout schemes, EPI single- and dual-echo. We found that there is no significant difference between the gray matter CBF values obtained for each scheme. The difference in CBF between TE1 and TE2 was also nearly the same for single- and dual-echo schemes, in

Figure 9 – Functional connectivity

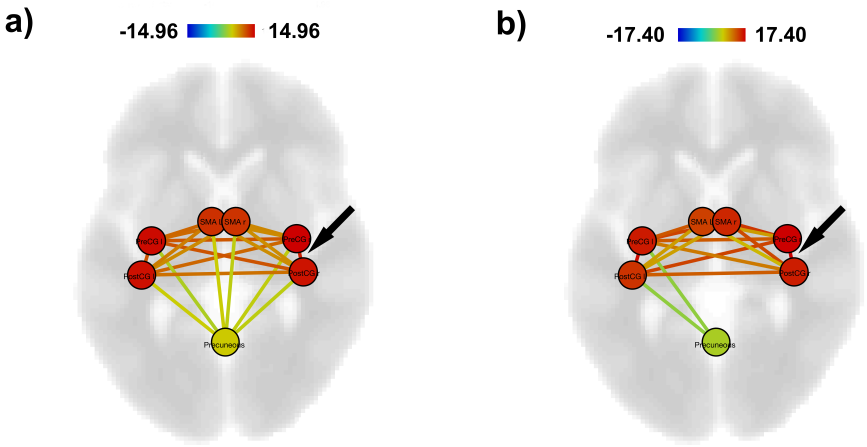

Functional connectivity within the motor network for (a) TE1 and (b)TE2. The arrow points to the correlation that shows a significant difference when comparing TE1 and TE2d ata. PreCG-l: left precentral gyrus; PreCG-r: right precentral gyrus; PostCG-l:left postcentral gyrus; PostCG-r: right postcentral gyrus; SMA-l: left supplementary motor area, SMA-r: right supplementary motor area, precuneus. Color bar refers to the range of T scores. Source: the author.

which the CBF values for TE2 were approximately 60% of the ones for TE1, due to T2 decay. One could account for such decay, but the lower image SNR for longer TE would still be present (95), resulting in a decrease of precision in CBF quantification. Short TE values are preferred for that case. To our knowledge, it is the first study that confirms that it is trustful to quantify CBF with DE-pCASL and short TE.

Although there was considerable spatial overlap between CBF and ccBOLD activation maps, the similarity coefficient was not high. More activation voxels were observed for ccBOLD, confirming its higher sensitivity but lower spatial specificity when compared to CBF signal (96, 97). It is especially observed for the longer TE acquisition where the BOLD contamination was higher (Figure 2). Such contamination may explain the signal variability observed on CBF time series for longer TE (Figure 3). For TE1, CBF values followed the experimental design for the finger-tapping task, in which all the four blocks were present. That behavior is not visible for TE2 due to the lower SNR of the images, so that the effect of outliers had a high impact in the time-series profile.

Those differences in CBF signal for different TE values also reflected changes in functional connectivity. There was a significant loss of connections among primary motor cortex areas and other regions not primarily associated with motor activation, but important for brain integration, such as the precuneus. Looking specifically to the primary motor cortex, we also found significant differences in the connectivity pattern for the connection between the post- and precentral gyri, two primary anatomical areas related to motor functions.

However, our study has some limitations. First, the number of volumes acquired in

each block of the acquisition paradigm was small, which may increase the effects of outliers in the temporal series, especially for the longer TE (Figure 3). However, increasing the number of volumes per block would increase significantly the total acquisition time, so that it must be considered to design the experiment. Second, our sample size may be considered small. However, we performed robust data analysis which is constantly performed in studies with similar sample size.

In conclusion, our study explored a set of information provided by the acquisition of DE-pCASL. Regarding CBF quantification, we found that CBF values obtained through DE-pCASL are statistically the same as those obtained with the standard pCASL scheme. Also, for functional analysis, images acquired with short TE were successful in identifying brain networks. Our findings suggest that DE-pCASL results are trustful for both CBF quantification and functional analysis and may be a good alternative to separate acquisitions of ASL and BOLD-fMRI, reducing acquisition time without losing any of that information.

3 Semantic verbal fluency brain network: delineating a physiological basis for the functional hubs using dual-echo ASL and graph theory approach

3.1 Abstract

The semantic verbal fluency (SVF) is a cognitive process that engages and modulates specific brain areas related to language comprehension and production, decision making, response inhibition, and memory retrieval. The impairment of the brain network responsible for these functions is related to a variety of neurological conditions, and different strategies have been proposed to assess SVF-related deficits in such diseases. In the present study, the concomitant changes of brain perfusion and functional connectivity were investigated during the reorganization of the brain network, considering resting state and SVF task performance. Arterial Spin Labeling, a perfusion-based magnetic resonance imaging (MRI) method, was used with a pseudocontinuous labeling approach and dual-echo readout, in thirteen healthy right-handed, Brazilian Portuguese speakers. During task performance, a significant increase in CBF was observed in language-related regions of the frontal lobe, including Brodmann's areas (BA) 6, 9, 45, and 47, associated with semantic processing, word retrieval, and speech motor programming. Such regions, along with the posterior cingulate, showed to have a crucial role in the SVF functional network, assessed by seed-to-voxel and graph analysis. Our approach was successful in overcoming the generalization problem regarding the graph analysis of functional MRI (fMRI) with cognitive, task-based paradigms. Moreover, the CBF maps enabled the functional assessment of orbital frontal and temporal regions commonly affected by magnetic susceptibility artifacts in conventional T2*-weighted fMRI approaches. Therefore, our results demonstrated the capability of ASL to evaluate perfusion alterations and functional patterns simultaneously during the reorganization of the SVF network providing a quantitative physiological basis to functional hubs in this network, which may support future clinical studies.

3.2 Introduction

Verbal fluency (VF) is a cognitive function that allows retrieving specific semantic or phonemic information within restricted searching parameters (98, 99). More specifically, semantic verbal fluency (SVF) involves typically the generation of words belonging to a given category. The cognitive processing associated with the SVF is supposed to engage and modulate specific brain areas related to language comprehension and production, decision making, response inhibition, and memory retrieval (100). The impairment of the brain network respon-

sible for these functions is related to several neurological conditions, such as Alzheimer's disease (101), Parkinson's disease (102), attention-deficit/hyperactivity disorder (103), epilepsy (104) and schizophrenia (105). Therefore, different strategies have been employed to assess SVF-related deficits related to them. They include the applications of neuropsychological tests (106) and neuroimaging techniques (100) in both clinical and investigational domains.

Functional neuroimaging studies have demonstrated the specialization of brain areas, mainly in frontal, parietal, and temporal lobes for SVF processing (107, 108). A recent meta-analysis reported left frontal areas along with left anterior cingulate, thalamus, and precuneus as the central regions involved with word production, attentional demands, and working memory (100). Other studies have also discussed the role of the temporal cortex, which is believed to mediate the semantic-based word retrieval (109, 108). Its involvement with SVF was confirmed by a recent study on the investigation of the effects of cortical excitability modulation with transcranial direct current stimulation (110). However, more than locating SVF-related regions, it is desirable to investigate how they are integrated. A dual-stream model, consisted of ventral and dorsal pathways for language, proposed that the dorsal route, which connects regions of the frontal lobe, is restricted to sensory-motor mapping of sound to articulation, while the ventral pathway, connecting the middle temporal lobe and the prefrontal cortex, subserves linguistic processing of sound to meaning (111). The ventral regions are also highly connected during resting-state, representing a semantic network, and facilitating neuronal activation during semantic-based tasks (112).

Moreover, recent studies have used graph theory analysis to assess the topology of brain networks. They have reported that semantic, phonological, and orthographic networks have small-world characteristics defined by short average path lengths between nodes and high local clustering (113). Regions of the anterior temporal lobe and inferior frontal cortex, including Broca's area, were reported to be hubs in functional brain networks related to language processing (114, 115). Also, graph analysis seems likely to become clinically relevant in neurology and psychiatry. It was useful to differentiate between mild cognitive impairment and Alzheimer's disease, and assess atypical hemispheric dominance in brain tumor, evaluating functional connections in language-related network (116, 117).

Many of SVF studies have used functional magnetic resonance imaging (fMRI based on the blood oxygen level-dependent (BOLD) contrast, given its fair compromise between spatial and temporal resolution, and high sensitivity to neuronal-related hemodynamic changes (78). However, BOLD contrast depends on a complex combination of blood oxygenation, cerebral blood volume, cerebral blood flow (CBF), and metabolic rate of oxygen, which may hamper the analysis in different diseases. On the other hand, the assessment of a single physiological parameter such as CBF, which is tightly coupled with glucose metabolism (118), is an appealing alternative for providing a novel perspective on the physiological basis underlying changes of functional connectivity in the healthy and damaged brain.

Arterial Spin Labeling (ASL) has shown its advantages as a magnetic resonance (MR) perfusion-weighted technique. Besides being noninvasive, ASL shows tissue specificity (119) and, to some degree, is insensitive to susceptibility artifacts (120). Perfusion-weighted images are achieved using the arterial blood as an endogenous tracer, which is magnetically labeled by the application of radiofrequency pulses. The pulses are applied in a strategic position (labeling plane), so the magnetization in the region of interest is altered when compared to a non-labeled condition (75, 23). CBF is then estimated from the subtraction between unlabeled images (ASL control images) and labeled images. Due to the ASL intrinsic low signal-to-noise ratio, multiple unlabeled-label pairs are acquired and averaged to quantify CBF (79). Moreover, the temporal series of ASL images allows the evaluation of CBF fluctuations over time, from which functional information can be estimated (78, 77, 79).

The investigation of the functional organization through ASL has two main advantages over BOLD-fMRI. First, ASL provides quantitative information about a single physiologic parameter (CBF) (60, 80). Second, ASL has a better spatial specificity to neuronal activity because its signal originates in the capillary bed (58, 61, 62, 63, 64). However, it is not as sensitive to hemodynamic alterations as BOLD-fMRI. Therefore, simultaneous BOLD and ASL sequences have been proposed (85, 86, 121). In this context, ASL, combined with a dual-echo readout (DE-ASL), is an emerging approach to optimize the acquisition aiming at both CBF quantification and functional analysis (82). Acquisition using short echo time (TE) provides perfusion-weighted images, while the use of longer TE increases the effect of transversal relaxation (T2*), typical of the BOLD contrast (79, 83). The BOLD signal measured from ASL images is called the concurrent BOLD (ccBOLD) effect.

Therefore, a simultaneous BOLD-CBF analysis was performed to assess the brain functional connectivity of the SVF-related network in healthy participants. The rearrangement of brain connections and changes in regional CBF, when compared to the resting-state condition, was also evaluated. A single perfusion-based ASL acquisition with dual-echo readout was used to ensure the same state during task engagement for BOLD and CBF responses. No similar study was previously reported for a cognitive task. Therefore, our objectives were to demonstrate the feasibility and advantages of performing this method to investigate the physiological basis underlying the functional organization of the SVF network; and to investigate the reorganization of the SVF network from resting-state to task performance. We hypothesize that we will observe CBF changes, and functional connectivity reorganization of SVF-related regions, mainly of classical word production, such as inferior frontal and temporal regions in the left hemisphere, from resting-state to task performance, using data of a single acquisition.

3.3 Methods

3.3.1 Subjects

Thirteen healthy right-handed, Brazilian Portuguese speakers were recruited. Exclusion criteria included: abuse of alcohol or illicit drugs, verified by the CAGE questionnaire (122); previous experience with the cognitive test within less than six months; language other than Portuguese; psychiatric disorders; presence of partial or total carotid artery stenosis, unilateral or bilateral; presence of brain injury from stroke or tumor; presence of pacemaker or prosthesis incompatible with the magnetic resonance environment; claustrophobia; visual deficits; and pregnancy. Gender, age, and education years were obtained from a demographic questionnaire. Cognitive status was assessed by the mini-mental state examination – expanded version (MMSE-2EV) (123). Participants showed no cognitive impairment (MMSE-2EV: 63 ± 8). The Ethics Committee of the institution approved the study, and all participants gave their written informed consent before participating in the study.

3.3.2 Image acquisition and protocol

Images were acquired on a 3T MRI scanner (Philips Healthcare, Best, Netherlands) equipped with a 32-channel receive head coil. A structural 3D gradient-echo T1-weighted scan was performed with TR = 7 ms, TE = 3.2 ms, FOV = 240 x 240 mm^2, 180 slices, slice thickness = 1 mm, spatial resolution = 1 x 1 mm^2, flip angle = 8°. 3D-TOF (time of flight) and axial fluid-attenuated inversion recovery (FLAIR) images were acquired with clinical protocols of the institution to confirm the absence of arterial occlusions and brain lesions, respectively.

DE-ASL data were acquired during task performance and at resting-state using a 2D echo-planar imaging (EPI) readout and a pseudo continuous (pCASL) labeling scheme with TR = 4000ms, TE1/TE2 = 9/28 ms, labeling duration/post-label delay = 1550/1600 ms, 20 slices, slice thickness = 5 mm, spatial resolution = 3.75 x 3.75 mm^2, FOV = 240 x 240 mm^2, flip angle = 90°. Proton-density-weighted images (M0) were acquired with TR = 15000 ms, TE = 14 ms, 20 slices, slice thickness = 5 mm, spatial resolution = 3.75 x 3.75 mm^2, FOV = 240 x 240 mm^2, flip angle = 90°, for CBF quantification.

The experimental protocol was divided into two runs: one consisting of a block-designed paradigm alternating an SVF task and a control condition, and another consisting of a 6-minute run at resting-state. For the task-based experiment (124), one category (among animals, colors, sports, and foods) was presented for each task block, and the participants were asked to think about words related to that category. During the control condition, participants were asked to read the months of the year presented randomly on a screen. Each block lasted 32 seconds (8 image volumes), totaling four blocks of rest and four blocks of task. Commands were developed in PsychoPy software (125) and presented on a monitor positioned in front of the MR scanner. Participants viewed the monitor through a mirror system placed on the

head coil. During the resting-state run, participants were asked to stay still with their eyes open in the absence of any specific thought or intention. Instead of including a rest condition between the task and control blocks, we chose to run a separate resting-state sequence to compare the task condition with the classical resting-state fMRI.

3.3.3 Image preprocessing

Imaging preprocessing was performed using customized scripts in MATLAB (MathWorks, Natick, MA), SPM12 (<http://www.fil.ion.ucl.ac.uk/spm>), and an open-source toolbox for ASL images (ASLtbx) (6). Preprocessing steps were applied to each participant's data separately. First, raw ASL images were head-motion corrected with a separate realignment for unlabeled and label images. No image dataset was excluded because of the incorrigible motion artifact. Then, ASL images were coregistered to anatomical images, temporal filtered (high pass > 0.04 Hz), and spatial smoothed using an isotropic Gaussian kernel (FWHM = 4 mm for CBF quantification and FWHM = 6 mm for functional analysis).

3.3.4 CBF quantification

Perfusion maps were generated by the subtraction of unlabeled and label images acquired with the short TE (= 9 ms). Quantification was performed using the sync subtraction for regional CBF mapping, while a running pairwise subtraction was performed for functional analysis to increase the number of perfusion-weighted images in the time series (89). Quantification was based on the General Kinetic Model (60) using the following parameters: blood longitudinal relaxation time (T1b) = 1650 ms; labeling efficiency = 0.85; blood/tissue water partition coefficient (gray matter/white matter) = 0.98/0.84 g/mL; tissue T1 (gray matter/white matter) = 1020/770 ms (90). Finally, CBF time series and mean CBF map were normalized to the MNI standard space (resolution = 2 x 2 x 2 mm3; matrix size: 79 x 95 x 79).

3.3.5 Functional Localization Analysis

Functional analysis for resting-state and task conditions was performed using the time series of CBF and concurrent BOLD (ccBOLD). The latter was obtained from the residual T2* weighting of the ASL images acquired with long TE (= 28 ms), regressing out the paradigm of the labeling and unlabeled [-1, 1, ... , -1, 1] from the label/unlabeled image series (126). CBF and ccBOLD time series were detrended and band-pass filtered (0.01-0.07 Hz for CBF; 0.0078-0.1 Hz for ccBOLD (86). A standard principal component analysis was used together with the CompCor algorithm (127) to remove the signal of white matter and cerebrospinal fluid.

A general linear model analysis using the FSL (<http://fsl.fmrib.ox.ac.uk/fsl/fslwiki>) was performed on each participant's data to check the activation map obtained from CBF

and ccBOLD (p-FDR < 0.05). The resulting maps were then compared with an anatomical template derived from the meta-analysis of different language tasks and fMRI (100). After overlapping the activated regions of our GLM maps and the template from the meta-analysis, six anatomical brain regions in the left hemisphere were coincident: superior frontal gyrus (SFG) – Brodmann area (BA) 6 and BA 8; medial frontal gyrus (MFG) – BA 6; inferior frontal gyrus (IFG) – BA 9, BA 45 and BA 47. These were selected for further analysis along with the posterior division of the left middle temporal gyrus (pMTG) – BA 21 and the posterior division of the left superior temporal gyrus (pSTG) – BA22. These regions are called SVF-related in the remaining of the text. Additionally, four nodes of the default mode network (DMN) and the cingulate gyrus (anterior and posterior divisions) were assessed. The additional regions were included due to th recent literature on SVF tasks (128).

The mean CBF value of each region was obtained for three conditions: resting-state, control, and SVF. A two-way ANOVA with repeated measures was performed to assess the effects of region and condition on CBF, considering significance at $p < 0.05$. A Tukey posthoc analysis was performed to evaluate CBF changes among conditions for each region of interest (ROI), considering multiple-comparisons and significance at $p < 0.05$. This statistical analysis was performed in R software.

A seed-to-voxel analysis was performed using CONN Toolbox (93), considering the SVF-related regions as seeds for the task-based data. First, CBF and ccBOLD were considered separately, and then the main effects of each one were analyzed to obtain a single map from both imaging modalities. For the three cases, a bivariate Pearson's correlation on r-values transformed to z-scores was performed. Significant correlations after correction for multiple comparisons and a cluster size cut-off (p-FDR < 0.00001, $k \geq 10$ for CBF and ccBOLD separately; p-FDR < 0.0000001, $k \geq 10$ for CBF and ccBOLD main effects) were shown in a spatial map.

The laterality index to verify the hemispheric dominance of SVF function, and the degree of clustering to assess the spatial layout of the obtained maps were calculated since meaningful processes tend to exhibit a well-defined spatial structure (129). The laterality index was defined as LI = (VLH – VRH)/(VLH + VRH), where VLH and VRH are the numbers of significant voxels in the left and right hemispheres of the obtained spatial maps, respectively. Left (LI > LITH) and right (LI < - LITH) dominances were assessed considering an LI threshold (LITH) of 0.2 (Seghier, 2008). The degree of clustering was defined as DCi = Nclu/Ntot for each obtained cluster i, where Nclu is the number of significant voxels of cluster i, and Ntot is the total number of significant voxels in the spatial map (130).

3.3.6 Functional Integration Analysis

First, an ROI-to-ROI analysis was performed considering the CBF and ccBOLD data separately for both SVF task and resting-state conditions. Then, for a combined analysis of

CBF and ccBOLD, the ROI-to-ROI analysis was performed considering both data. For all cases, a bivariate Pearson's correlation on r-values transformed to z-scores was performed and checked the significance correcting for multiple comparisons.

3.3.7 Graph Theory Analysis

Graph theory analysis (GTA) was performed using the Graph toolbox implemented in CONN (93). The topological structure of the functional brain network organization during the performance of the SVF task was analyzed to verify whether a small-world topology was satisfied for CBF, ccBOLD, and combined CBF and ccBOLD data. We used an approach for range cut-off threshold previously published (131), and two different templates separately.

- Template 1: ROIs previously used for functional integration analysis.
- Template 2: functional templates of the resting-state networks available in CONN toolbox and composed by the DMN, sensory-motor network (SMN), visual network (VN), salience network (SAN), dorsal attention network (DAN), frontal-parietal network (FPN), language network (LAN), cerebellar network (CB), and their subdivisions, totaling 32 nodes. This template comprised a whole-brain network and was used for exploratory analysis of the brain organization during the SVF task.

The next step was the construction of a weighted adjacency matrix for each template and threshold them over a range of r-values in steps of 0.01. Since there is no consensus on the most accurate approach for such thresholding (132), the following criteria to define the r-value range (133) were considered. First, the experimental network should be fully connected, i.e., every node should be integrated into the network by at least one edge (131). Second, the experimental network should meet the criteria for a small-world network, as expected from a group of young participants (134). Finally, the experimental network should be as cost-efficient as possible, i.e., it should have the lowest connection density while keeping the same efficiency. Therefore, its wiring cost should not exceed the value of 0.5 (135).

To meet the small-world network condition, two main criteria were analyzed. First, the range in which the global efficiency of the experimental network approximates to the global efficiency of an equivalent random network and, second, when its local efficiency surpasses that of an equivalent random network (136). The analysis considering all criteria described above was used to find the range of r-values (Fisher transformed) for thresholding. The following parameters were calculated over the obtained range: clustering coefficient, local efficiency, characteristic path length, global efficiency, degree, and betweenness centrality (136, 137, 138). Nodes with degree and betweenness centrality (BC) values at least one standard deviation above the average values for the network were considered hubs. All graph metrics were compared to assess the differences between the resting-state and SVF task. First,

variable homoscedasticity was tested with the Shapiro-Wilk normality test ($p < 0.05$). For normal variables, a parametric t-test for two independent means was used. For non-normal variables, a non-parametric Mann Whitney U test.

3.4 Results

3.4.1 CBF changes

Figure 10 shows the mean CBF values for all ROIs comparing resting-state, control condition, and SVF task performance. No region showed CBF differences when comparing the control condition with the other two conditions (SVF and resting-state). CBF differences were significant between SVF and resting-state conditions for the superior frontal gyrus (SFG – BA6; $p = 0.008$) and inferior frontal gyrus (IFG – BA47; $p = 0.023$). For SFG – BA9 ($p = 0.078$), medial frontal gyrus (MFG – BA6; $p = 0.077$) and IFG – BA45 ($p = 0.065$), the differences indicate a tendency of CBF change.

Figure 10 – Regional cerebral blood flow

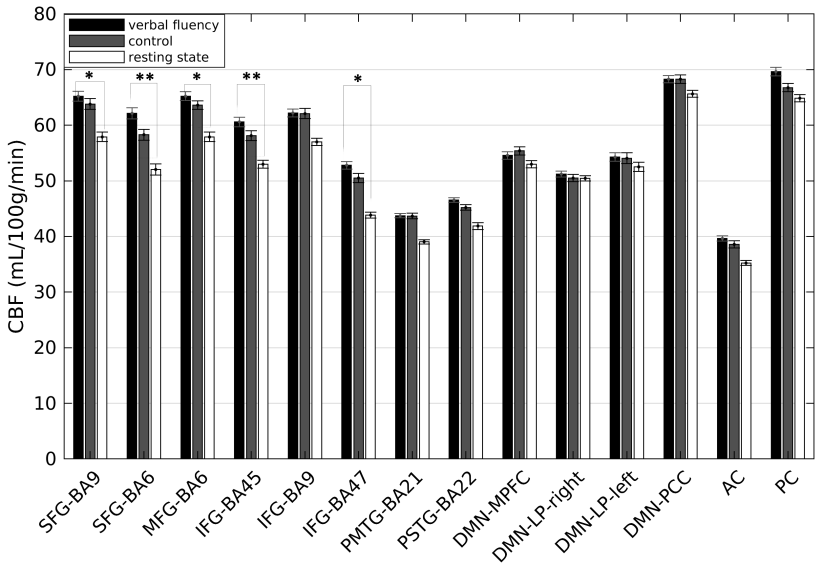

Mean CBF values (mL/100g/min) of each region of interest (ROI) for semantic verbal fluency (SVF, black), control (gray), and resting-state (white) conditions. A two-way ANOVA with repeated measures was performed to assess the effects of region and condition on CBF. A Tukey posthoc analysis was performed to assess CBF changes among conditions for each ROI. ** $p < 0.05$, corrected for multiple comparisons. * $p < 0.1$, corrected for multiple comparisons ($p < 0.05$, when control condition was excluded from the statistical analysis). SFG: superior frontal gyrus, MFG: medial frontal gyrus, IFG: inferior frontal gyrus, pMTG: middle temporal gyrus – posterior division, pSTG: superior temporal gyrus – posterior division, DMN: default mode network. MPFC: medial prefrontal cortex, LP: lateral parietal, PCC: posterior cingulate cortex, AC: anterior cingulate, PC: posterior cingulate. Source: the author.

3.4.2 Seed-to-voxel analysis

Functional maps obtained from ccBOLD (Figure 11a) and CBF (Figure 11b) showed responses mostly in the left hemisphere during the SVF task, confirming the lateralization of this function. Responses were more lateralized for CBF (LI = 0.63) compared to ccBOLD (LI = 0.42), but no difference was observed regarding degree of clustering (CBF – DC = 0.018, ccBOLD – DC = 0.022; $p > 0.05$). Moreover, ccBOLD map showed a more extended response in the frontal pole, middle frontal gyrus, superior parietal lobule, and superior portion of the lateral occipital cortex. On the other hand, the CBF map showed more extended response in the middle and superior temporal gyri, Heschl's gyrus, planum temporale, orbital part of the inferior frontal gyrus, and insular cortex. When considering CBF and ccBOLD information simultaneously (Figure 11c), it resulted in left lateralization (LI = 0.44), and degree of clustering similar to the other maps (DC = 0.018).

Figure 11 – Functional localization

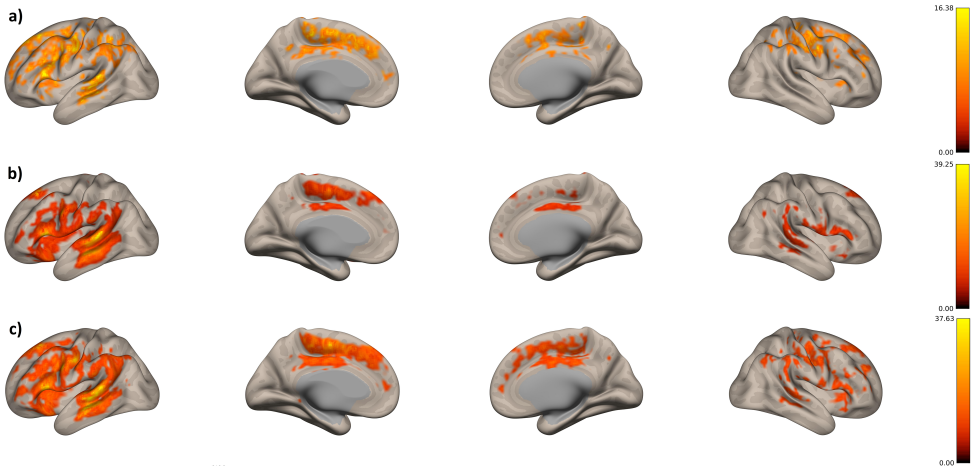

Functional maps of the semantic verbal fluency task for (a) ccBOLD (p-FDR < 10^{-5}, k ≥ 10), (b) CBF (p-FDR < 10^{-5}, k ≥ 10) and (c) combined CBF and ccBOLD time series (p-FDR < 10^{-7}, k ≥ 10). Color bars represent F-values. Source: the author.

3.4.3 ROI-to-ROI analysis

Figure 12 shows the functional connectivity patterns for the SVF network compared to the resting-state (SVF task > resting-state). Results from ccBOLD (Figure 12a) showed the inferior frontal gyrus (BA 9) connecting to the frontal, temporal, and right hemisphere areas of the network. Functional connectivity obtained from CBF (Figure 12b) showed pMTG connecting to the entire network. ccBOLD findings presented a higher number of significant connections and connected nodes when compared to the CBF results. Moreover, the SVF-related network, when considering the main effects of CBF and ccBOLD together (Figure 13), showed the IFG-BA 9 as an important node. This conjunction analysis showed a more integrated network when compared to the findings from Figure 12.

Figure 12 – Functional connectivity

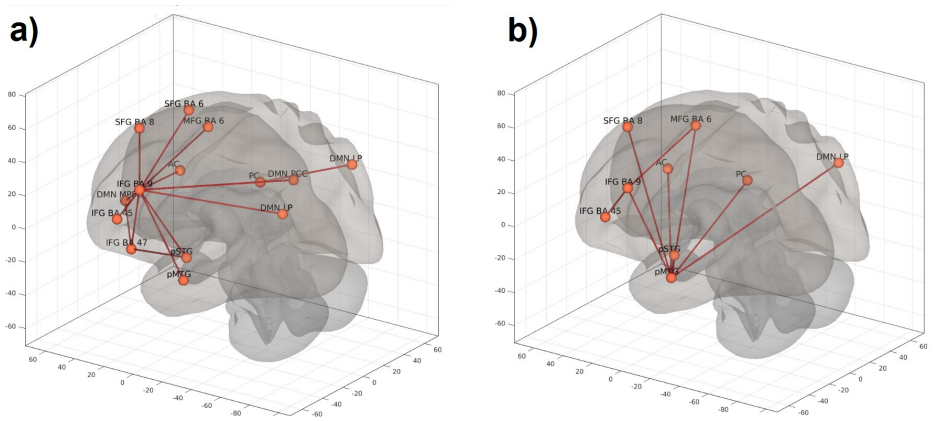

ROI-to-ROI functional connectivity patterns for (a) ccBOLD, and (b) CBF. Significance was set to $p < 0.1$, FDR-corrected. Source: the author.

3.4.4 Graph Analysis

3.4.4.1 Small-world networks

During resting-state condition and SVF task, the network of our empirical data met all criteria for small-worldness when considering CBF, ccBOLD, and CBF-ccBOLD time series for both templates. Table 2 presents the respective r-value ranges for such cases. For illustration, Figure 14 shows the obtained graphs for combined CBF-ccBOLD data, indicating the intervals of costs where the networks present small-world characteristics when template 2 was used.

3.4.4.2 Graph metrics

Table 3 presents the graph metrics calculated from data obtained with CBF, ccBOLD and the combination of CBF and ccBOLD information for both resting-state and task conditions, using templates 1 and 2, and the respective r-value ranges obtained for small-wordness criteria (Table 2). For template 1, results showed no difference in graph metrics during the functional reorganization. However, for template 2, global efficiency, cost, and degree increased significantly when considering the CBF time-series, while only betweenness centrality increased significantly when considering the ccBOLD time-series. For the combination of both imaging categories, the clustering coefficient, local efficiency, global efficiency, degree, and cost increased significantly, while the average path length decreased, during the reorganization of the whole-brain network from resting-state to task performance.

Moreover, for template 2, regions that constitute the DMN, LAN, and DAN were hubs during the resting-state condition, while regions of the DMN, SAN, LAN, and DAN were hubs during task performance (Table 4). The left IFG portion of LAN englobes part of the IFG-BA 47 node, while both the superior node of SMN and left FEF portion of DAN overlap with part of the SFG-BA 6. In contrast, no functional hubs were found for template 1 when using the three

Figure 13 – Functional integration

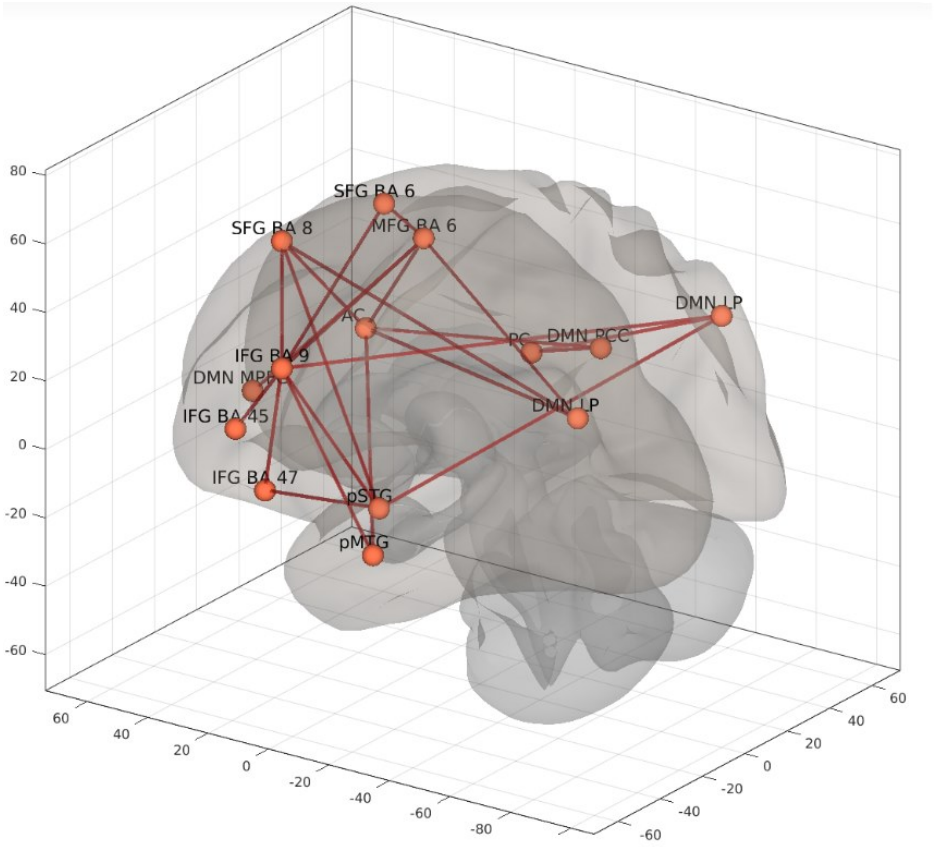

Functional connectivity pattern considering the main effects of CBF and ccBOLD time series. All regions of template 1 were considered (p-FDR < 0.1). Source: the author.

Table 2 – Functional hubs obtained for template 2.

	Resting-state condition				Semantic verbal fluency task			
	Template 1		Template 2		Template 1		Template 2	
	r min[i]	r max[ii]	r min	r max	r min	r max	r min	r max
ccBOLD	0.52	0.58	0.41	0.47	0.53	0.59	0.50	0.56
CBF	0.34	0.36	0.45	0.51	0.44	0.50	0.41	0.47
CBF-ccBOLD	0.39	0.43	0.46	0.52	0.46	0.52	0.41	0.47

[i] r min: minimum r-value [ii] r max: maximum r-value

time-series (CBF, ccBOLD and the combination of both). However, the MFG (BA 6) and the posterior cingulate presented high values of global efficiency, cost, betweenness centrality, and degree, when considering the combined CBF-ccBOLD information (Figure 15).

Table 3 – Graph metrics (mean ± SD) of the overall network for CBF, ccBOLD, and combined CBF-ccBOLD data.

	CBF			ccBOLD			CBF-ccBOLD		
	RS[iii]	Task	Statistic	RS	Task	Statistic	RS	Task	Statistic
Template 1									
Clustering Coefficient	0.71 ± 0.12	0.61 ± 0.22	U=64, z=-1.02, †p=0.15	0.50 ± 0.28	0.65 ± 0.12	U=61, z=1.18, †p=0.12	0.68 ± 0.10	0.65 ± 0.18	U=290, z=-0.87, †p=0.19
Local Efficiency	0.80 ± 0.12	0.69 ± 0.25	U=58, z=-1.33, †p=0.09	0.57 ± 0.32	0.74 ± 0.13	U=59, z=1.28, †p=0.10	0.77 ± 0.17	0.74 ± 0.21	U=299, z=-0.70, †p=0.24
Global Efficiency	0.66 ± 0.15	0.57 ± 0.21	t=-1.22, *p=0.12	0.45 ± 0.18	0.55 ± 0.22	t=1.20, *p=0.12	0.62 ± 0.19	0.60 ± 0.22	U=327, z=-0.19, †p=0.42
Average Path Length	1.69 ± 0.34	1.72 ± 0.33	t=0.19, *p=0.43	1.92 ± 0.43	1.68 ± 0.27	t=-1.70, *p=0.05	1.63 ± 0.27	1.66 ± 0.29	t=0.37, p=0.35
Betweenness Centrality	0.054 ± 0.02	0.050 ± 0.02	t=-0.34, *p=0.37	0.06 ± 0.03	0.04 ± 0.02	t=-1.29, *p=0.10	0.04 ± 0.02	0.04 ± 0.02	t=0.22, *p=0.41
Degree	5.84 ± 2.22	4.94 ± 2.49	t=-0.98, *p=0.17	3.41 ± 1.75	4.61 ± 2.35	t=1.47, *p=0.08	5.60 ± 2.38	5.38 ± 2.57	t=-0.32, *p=0.37
Cost	0.45 ± 0.17	0.38 ± 0.19	t=-0.98, *p=0.17	0.26 ± 0.13	0.35 ± 0.18	t=1.47, *p=0.08	0.43 ± 0.18	0.41 ± 0.19	t=-0.32, *p=0.37
Template 2									
	RS	Task	Statistic	RS	Task	Statistic	RS	Task	Statistic
Clustering Coefficient	0.64 ± 0.06	0.66 ± 0.09	t=0.89, *p=0.19	0.66 ± 0.09	0.68 ± 0.09	t=0.49, *p=0.31	0.63 ± 0.09	0.69 ± 0.11	U=206, z=2.40, †**p=0.008**
Local Efficiency	0.74 ± 0.06	0.78 ± 0.07	t=1.57, *p=0.06	0.79 ± 0.09	0.81 ± 0.08	U=75, z=0.46, †p=0.32	0.74 ± 0.11	0.80 ± 0.09	U=192, z=2.66, †**p=0.004**
Global Efficiency	0.39 ± 0.13	0.56 ± 0.07	t=4.18, *p=0.0002	0.58 ± 0.10	0.53 ± 0.17	t=-0.79, *p=0.22	0.43 ± 0.14	0.62 ± 0.12	t=5.26, *p<0.00001
Average Path Length	2.12 ± 0.35	2.03 ± 0.29	t=-0.71, *p=0.24	2.04 ± 0.65	1.84 ± 0.29	U=71, z=-0.67, †p=0.25	2.14 ± 0.39	1.86 ± 0.35	U=195, z=-2.61, †**p=0.0045**
Betweenness Centrality	0.029 ± 0.010	0.032 ± 0.010	t=0.70, *p=0.24	0.032 ± 0.018	0.022 ± 0.056	U=43, z=-2.10, †p=0.02	0.030 ± 0.010	0.027 ± 0.011	t=-0.99, *p=0.16
Degree	6.17 ± 2.25	9.62 ± 2.77	t=3.49, *p=0.0009	10.07 ± 3.39	10.04 ± 4.94	t=-0.02, *p=0.49	6.92 ± 2.87	11.97 ± 4.95	t=4.49, *p=0.00002
Cost	0.19 ± 0.07	0.31 ± 0.09	t=3.48, *p=0.0009	0.32 ± 0.11	0.32 ± 0.16	t=-0.02, *p=0.49	0.63 ± 0.09	0.69 ± 0.11	t=4.49, *p=0.00002

[iii] RS = resting state † p calculated using Mann Whitney U test. * p calculated using the t-test for two independent means. Significant differences in bold.

Figure 14 – Small-world networks

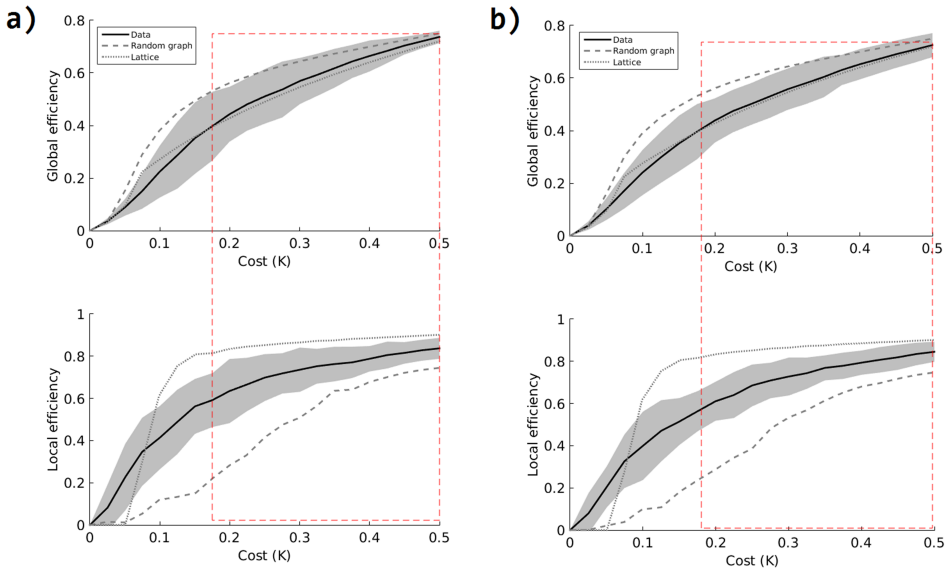

Global efficiency and local efficiency versus the cost of the brain network organization (a) at resting-state and (b) task performance using template 2. Combined CBF-ccBOLD data was considered. Red dotted rectangles indicate the regions where the networks present small-world characteristics. Source: the author.

3.5 Discussion

In the present study, the reorganization of the semantic verbal fluency network in healthy controls was evaluated using a dual-echo ASL acquisition, allowing the quantification of CBF and the assessment of functional connectivity concomitantly, which provided a physiological basis to our functional findings.

When comparing task performance with the resting-state condition, an increase in CBF was observed in language-associated regions in the frontal lobe, mainly in the inferior (BA 47) and superior (BA 6) frontal gyri. Both areas are associated with semantic (88, 126, 90) and phonological processing (93) and encoding (127, 85, 86). Moreover, a PET study reported that BA 6 is related to word retrieval (139), while a previous BOLD study reported its activation during overt speech (140). The significant CBF change in BA 6 during our covert word production task seems to be associated with word retrieval and speech motor programming. However, these areas did not show CBF increase when comparing SVF task with the control condition, probably because both regions are also related to word reading, aloud or silently, as in our control task (reading the months of the year) (141, 142). Other frontal regions previously associated with language processing, including Broca's area (IFG – BA 45), showed a trend for a significant increase in CBF during SVF task performance compared to the resting-state condition. These areas are involved in the ability to generate words and working memory during tasks similar to ours (79, 60, 80).

The functional connectivity maps obtained with the seed-to-voxel analysis showed

Figure 15 – Graphs metrics

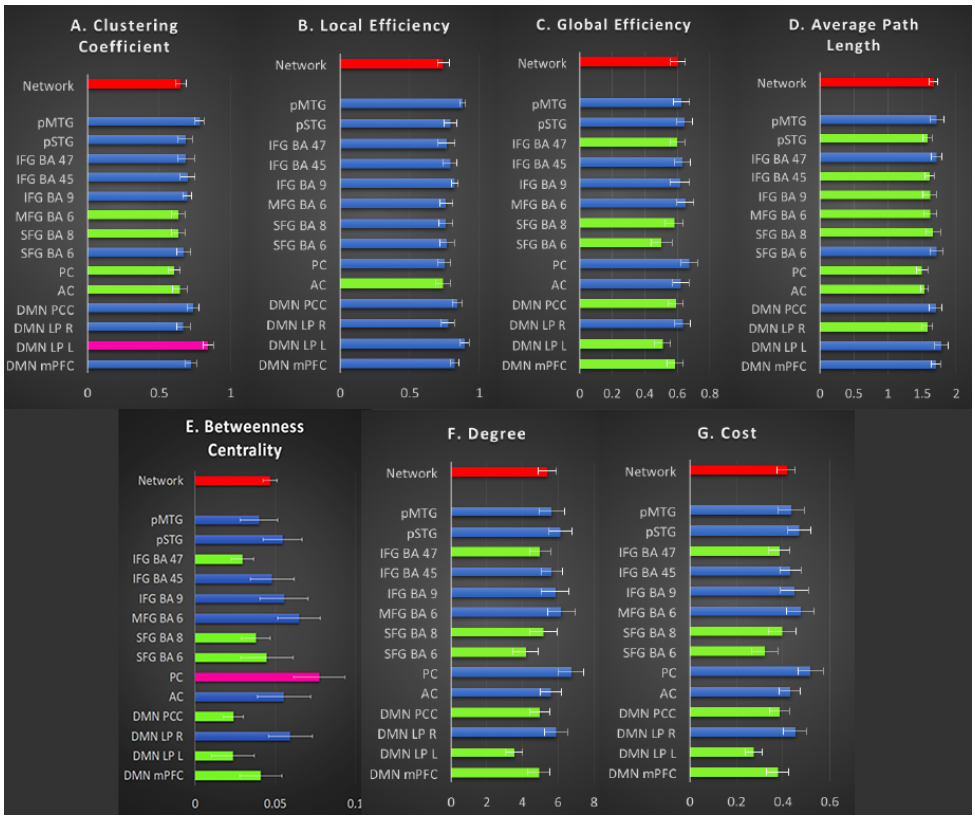

Panels (A–G) illustrate the averaged graph metrics of the semantic verbal fluency network considering the combined CBF-ccBOLD information (r-value range: 0.46 to 0.52) during task condition. Red: the network mean values; pink: regions (nodes) with mean value at least one standard deviation over the network mean; blue: regions with a mean value higher than the average value for the network; light green: regions with equal or smaller values than the average value for the network. Error bars represent the standard error. Source: the author.

similar spatial patterns when comparing CBF and ccBOLD data regarding left lateralization and response of the main SVF-related regions. However, ccBOLD map showed response in a greater area of the frontal lobe, superior parietal lobule, and lateral occipital cortex (superior portion). These regions, associated with language processing and speech motor programming, were also found in CBF maps, but in smaller clusters. On the other hand, CBF map showed extended response in the orbital part of the inferior frontal gyrus, and in the temporal gyrus, which encloses areas that are part of the language network for comprehension and production, as identified in PET studies (131, 143). Such areas are mostly affected by the signal loss at the interface of tissue and fluid/air due to local differences of magnetic susceptibility in conventional T2*-weighted fMRI approaches (144, 114). The results obtained by DE-ASL were able to overcome this issue, which suggests this method an appealing alternative to combine brain physiology and functionality in a non-invasive approach.

Additional connectivity findings include the anterior and posterior parts of the cingulate gyrus, and parietal regions, which are associated with transferring visual information to Wernicke's area and with lexico-semantic processing of familiar words (145). Moreover, the

Table 4 – Functional hubs obtained for template 2.

	Resting State			Task		
	Region	BC	Degree	Region	BC[iv]	Degree
CBF	Left lateral region (SMN[v])	0.083	12.10	Right lateral parietal (DMN)	0.048	14.25
	Right lateral region (SMN)	0.061	10.89	Right SMG[vi] (SAN[vii])	0.067	16.36
	Left STG[viii] (LAN[ix])	0.067	11.67	Left STG (LAN)	0.049	16.38
	Right STG (LAN)	0.067	10.69			
ccBOLD	Left IPS[x] (DAN[xi])	0.055	14.46	Left IPS (DAN)	0.040	15.58
	Right IPS (DAN)	0.056	14.52			
	Right lateral region (SMN)	0.053	15.80			
	Right STG (LAN)	0.056	14.07			
CBF-ccBOLD	Left lateral region (SMN)	0.063	12.21	Right SMG (SAN)	0.090	17.53
	Right lateral region (SMN)	0.055	11.85	Left STG (LAN)	0.043	17.78
	Left STG (LAN)	0.067	11.47			
	Right STG (LAN)	0.064	10.09			

[iv] BC: betweenness centrality [v] SMN: sensory-motor network [vi] SMG: supramarginal gyrus [vii] SAN: salience network [viii] STG: superior temporal gyrus [ix] LAN: language network [x] IPS: intraparietal sulcus. [xi] DAN: dorsal attention network

anterior cingulate is activated during word generation and can be related to the attentional demands required by the task. It was recently reported that this region is critical in reducing distraction from irrelevant stimuli and driving attention toward specific sites (146).

The rearrangement of brain temporal functional connectivity patterns between resting-state and SVF conditions was evaluated by an ROI-to-ROI analysis. For ccBOLD, the rearrangement had IFG-BA9 as a critical connecting region as previously reported (106). On the other hand, for CBF, there were a lower number of rearranged connections and nodes. Such feature reinforced the spatial specificity of CBF measurements and suggested a more accurate localization of the rearranged regions (147, 97), while BOLD presented higher sensitivity.

Moreover, the combined CBF-ccBOLD analysis presented a more interconnected network, while retaining a connection between clusters (functional integration), typical behavior of BOLD signal analysis (148, 149, 150). Furthermore, considering the DMN nodes and the anterior and posterior portions of the cingulate cortex, the results showed that the posterior regions are associated with transferring visual information to Wernicke's area, where such information is comprehended, and phonological retrieval happens (151), and then transferred to frontal areas, where words are generated. Our findings support the current model of language processing in which a frontotemporal network is divided into dorsal and ventral pathways associated with phonological and semantic operations (152).

SVF functional organization presented small-world characteristics, that is, high local and global efficiencies. It reflects highly clustered networks with a small average path length, allowing rapid communication between any two regions of the network (134). As expected, the most probable functional hubs were found in regions of the attentive, language and sensorimotor networks when considering the whole brain (template 2). Moreover, the posterior cingulate and medial frontal gyrus (BA 6) seem to play an essential role in the SVF network when considering only the regions activated by the task (template 1). The posterior cingulate is known as part of the central DMN node, being related to language and semantic discrimination (128). This region also presented the highest CBF value for all conditions, showing a possible relationship between metabolism and functional hubs. In addition, as cited before, the medial frontal gyrus is commonly associated with word retrieval and speech motor programming and showed a significant increase in CBF during task performance.

Another approach used to verify the reorganization of the whole-brain network from resting-state to task performance was the graph metrics. For this analysis, increases in the clustering coefficient, local efficiency, global efficiency, degree and cost, and decrease in average path length were observed when analyzing the combined CBF-ccBOLD. This analysis using fMRI has been previously performed for the brain network at rest, showing that it presents small-world topology (122), which is considered a characteristic of healthy subjects. However, graph analysis in task-based fMRI suffers from limited validity and generalization (123). Therefore, we applied the criteria used in a previous graph theory analysis of language in the brain at rest (133) and found similar and consistent results.

In summary, the graph analysis using the CBF and BOLD information concomitantly and a whole-brain template for the nodes allowed us to assess the changes that occurred in the SVF functional network when comparing the resting-state condition with the task performance. Our results suggest that the used methodology may overcome the generalization problem regarding the graph analysis of fMRI with cognitive paradigms. Therefore, the graph theory approach can be used as a tool in future studies to assess functional markers between healthy and clinical groups in both rest and task-based fMRI if one carefully selects the regions of interest.

The joint CBF-ccBOLD analysis presented a more interconnected network with every node integrated with the network by at least on edge when compared to ccBOLD and CBF individual findings. Interestingly, it meets the first criteria considered in this study to perform graph analysis (131). It suggests that joint CBF-ccBOLD is useful to apply graph theory approaches. Additionally, it was possible to delineate a physiological basis for functional hubs in the SVF network, once significant CBF changes in SFG-BA 6 and IFG-47 nodes match areas of functional hubs of SVF network, namely the DMN, DAN, and LAN networks. It suggests that dual-echo acquisition providing CBF and ccBOLD conjunction analysis are useful to determine functional hubs in task performance and its related physiological basis using a

whole-brain parcellation template.

Limitations of our study include the relatively small number of participants, and the SVF task performed silently. Currently, verbal fluency fMRI studies have used tasks with loud articulation of words, since silent articulation may produce non-linguistic activation, resulting from response inhibition within the motor speech system. However, we chose the silent performance of the SVF task to avoid motor and movement artifacts. Regarding the sample size, although small, it is similar to the number of participants of other task-based fMRI studies. Moreover, the results were consistent between subjects and were in accordance with what we expected based on the literature.

In conclusion, our study demonstrated the potential of arterial spin labeling technique for the assessment of an important brain function by evidence of a quantitative physiological parameter. Through a single MRI acquisition, our results suggested the effectiveness of ASL to detect CBF changes under an SVF task, and are comparable to other imaging techniques. Moreover, our CBF/ccBOLD results for network delineation, functional connectivity, and graph analysis provided a complete evaluation of the functional brain reorganization in agreement to classical results in the literature. The advantage of spatial specificity and quantitative physiological information makes ASL an appealing method to investigate neurological disorders that affect the cognitive processing of language-associated brain function.

4 Evaluation of number of segments in 3D GRASE readout and flow compensation effects for time-encoded pCASL

4.1 Introduction

Arterial Spin Labeling (ASL) is a noninvasive perfusion-weighted image (PWI) that takes advantage of the arterial blood as an endogenous tracer. A bolus of arterial blood is magnetically labeled in a slab proximal to the imaging plane to follow the flowing blood from the basilar artery to the intracranial arteries and further crossing the blood-brain barrier (BBB) to reach the brain tissue. After labeling the blood through the application of radio-frequency (RF) pulses, the labeled blood continues flowing during a time interval called post labeling delay PLD until arriving at the imaging slab. In order to measure the cerebral blood flow (CBF), a single PLD is enough. Nonetheless, when the subject suffers from an altered arterial transit time (ATT) or when it is desired to measure ATT or to follow the inflow blood, multiple PLDs are required, the so-called multi-PLD ASL.

Although a general ASL sequence can be described as three main blocks (labeling, post-labeling delay and the readout), there are several different ASL pulse sequence designs, which hampered its dissemination to the clinical routine practices. In 2015, a consensus paper was published with the recommended implementation of ASL for clinical application (31) to help the standardization and dissemination of ASL. Pseudo-continuous ASL (pCASL) combined with a Hadamard temporal encoding strategy was the recommended combination of labeling and post-labeling delay when multi-PLD ASL is chosen. Hadamard-encoded pCASL or time-encoded pCASL (te-pCASL) is a time-efficient way to retrieve ATT information as well as the monitoring of the inflow blood during the brain perfusion process (52, 153, 154, 53).

Regarding the readout module for ASL pulse sequence, the recommendation was the segmented 3D Gradient and Spin Echo (GRASE) (50, 49, 31), since it provides optimal background suppression by only using a single excitation pulse per TR and results in a higher SNR compared to 2D echo-planar images (EPI) (47, 45). The choice of the number of segments of the 3D GRASE readout scheme requires a fine-tuning between gains in SNR, blurring in the z-direction, and vulnerability to motion. While e.g. single-shot 3D GRASE results in significant blurring in the z-direction and the acquisition of only one average will make the images vulnerable to motion, it can be time-efficient when the M0 scan is acquired with the same segmentation number.

Another difficult choice is whether to use flow compensated (FC) gradients that compensate for the first-order dephasing effects (48). The use of FC can result in longer TE as well as longer readout times, which may lead to the introduction of blurring artifacts. However, the absence of FC might crush the vascular ASL-signal and thereby the suppression of vas-

cular artifacts. Despite the use of flow crushing was not recommended, the impact of FC is especially important for te-pCASL since it also depicts the angiographic phase of the dynamic ASL signal.

This study aimed to evaluate the impact of the number of segmentation of the 3D GRASE readout on the tSNR, comparing its performance to the 2D EPI readout, as well as to analyze the effect of flow compensation gradients, regarding the delineation of the presence of vascular ASL-signal.

4.2 Methods

4.2.1 Hadamard-encoded pCASL

Figure 16 – Hadamard encoding pCASL

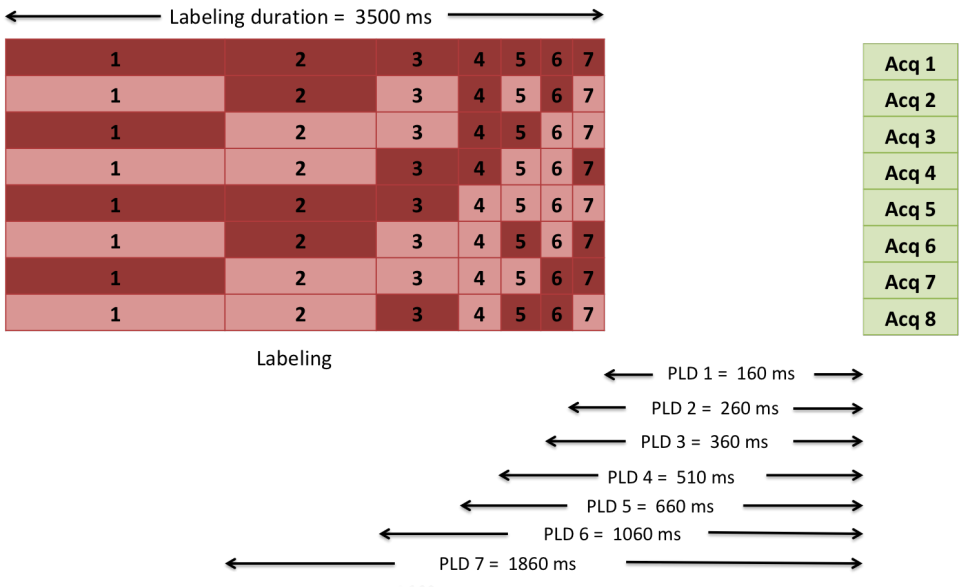

pCASL labeling scheme with temporal enconding using the Hadamard matrix. Source: the author.

Time-encoded or Hadamard-encoded pCASL is a time-efficient strategy to acquire multi-PLD pCASL, providing the monitoring of the inflow blood in the brain tissue, CBF quantification, ATT and aBV maps. In a time-encoded acquisition, the labeling module is divided into small label and control blocks, which are encoded according to a Hadamard matrix to determine if a block will be control or label. In this study, a Hadamard-8 matrix was chosen for the labeling module, with a total labeling duration of 3500 ms split into seven blocks of 1800, 800, 400, 2 x 150, and 2 x 100 ms. After the labeling module, there is a post-labeling delay PLD of 160 ms until the image acquisition (Figure 16). The image is acquired eight times so that each one contains information of all the PLD acquired, which can be a control or label information, according to the Hadamard matrix. The subtraction is then

performed for each column of blocks by decoding the Hadamard matrix. Since there are eight repetitions and seven PLDs, a total of 56 images are acquired, resulting in 28 ASL pairs.

4.2.2 3D GRASE segmentation number experiment

The 3D GRASE readout is an alternative strategy to combine the time efficiency of EPI readout with the high SNR of the rapid acquisition with refocused echoes (RARE) technique. The approach consists of the use of refocusing RF pulses to reduce the effects of phase errors, allowing the acquisition of multiple k-space lines with a single excitation RF pulse (Figure 17). If an entire slab is acquired with the application of only one excitation pulse, the approach is called single-shot 3D GRASE, while when more than one shot is required to fill the k-space for one slab the approach is named multi-shot. In this study, we evaluated the number of shots in 3D GRASE readout for a te-pCASL acquisition regarding time efficiency, blurring in the z-direction and the SNR by acquiring images using approaches with a single shot, two shots, and three shots. The results for SNR were also compared to a 2D multi-slice EPI.

Figure 17 – 3D GRASE readout for one segment

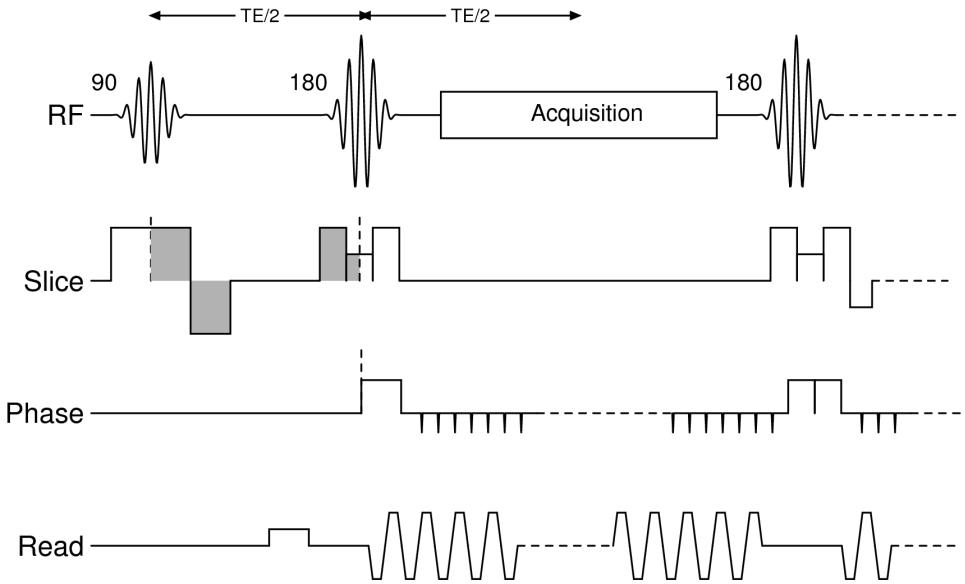

3D GRASE readout for one segment. For this approach, only one excitation pulse is employed in one TR. N refocusing pulses are employed to reduce the dephasing errors. Source: the author.

4.2.3 Flow compensation scaling experiment

The purpose of using flow compensation gradients is to correct for 1^{st} order flow-related dephasing. It is achieved by the employment of additional bipolar gradient lobes before signal readout (Figure 18). As the contribution for the positive and negative lobes are the same, the mean gradient added is zero, so these gradients do not affect stationary spins. On the other hand, the timing for the application of each gradient lobe is calculated to

have zero dephasing at imaging time for the moving spins. The limitations in adding flow-compensate gradients are the correction only for spins moving under constant velocity or acceleration, and the increase in the TE value, which may introduce some blurring effects to the acquired images. These limitations were the reason for the non-recommendation of FC gradients for ASL. Nonetheless, especially when using a 3D readout, the visualization of the intravascular signal in the angiography phase of the dynamic ASL signal can be hardly hampered. Therefore, we analyzed the effect of scaling the FC gradients added in a 2-shot 3D GRASE readout on the resulted images, evaluating the results for both intravascular and perfusion phases.

Figure 18 – Flow compensation gradients

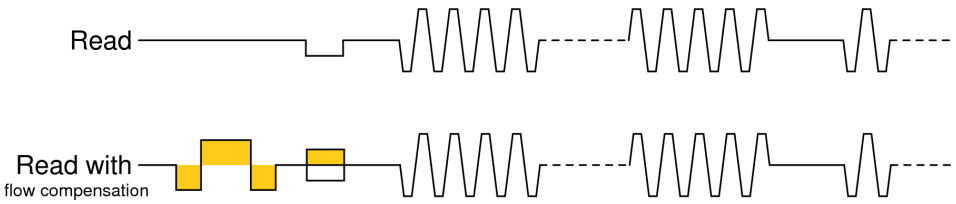

A bipolar flow compensate gradient is added to the readout gradients in x-direction to minimize dephasing effects for moving spins. Source: the author.

4.2.4 MRI experiments

Eleven volunteers (7 females, age 26.3 ± 5.2 years) were scanned in a 3T Philips MRI scanner. We used a time-encoded Hadamard 8 pCASL labeling sequence with single-shot, two-shot and three-shot 3D GRASE (TE (ms)/TR (s) = 9.2/4.1, 13.9/3.9 and 10.5/3.9, respectively; all with first-order FC enabled) and 2D EPI (TE (ms)/TR (s) = 9.2/4.1). The total labeling duration was 3500 ms, which was divided into blocks of 1800, 800, 400, 2 x 150, and 2 x 100 ms and a minimum PLD of 260 ms. Two background suppressions were applied at 1831 ms and 3135 ms. For all acquisitions, total scan time was kept around 6 min using 8, 6, 3 and 1 averages, respectively. Two-shot 3D GRASE scans were acquired with and without FC. The flow-compensation gradients' strength was also scaled with 25%, 50%, 75% and 100% of full first-order FC to analyze the visualization of the vascular ASL-signal.

4.2.5 Data analysis

The decoding of the Hadamard matrix for ASL subtraction was performed in MATLAB (MathWorks, Natick, MA) to obtain the perfusion maps. The scans were corrected for motion using the MCFLIRT tool in FSL (FMRIB Analysis Group, Oxford, UK) to reduce subtraction errors. FSL/BASIL was used to quantify CBF and arterial blood volume (aBV). Post-processing

and calculation of temporal SNR (tSNR) was done in MATLAB according to Equation 4.1.

$$\text{tSNR} = S * \sqrt{\frac{\text{Number of averages in 6 min}}{\sigma}} \tag{4.1}$$

where S is the mean signal of a voxel over the different PLDs and σ is the standard deviation for the same voxel.

4.3 Results

4.3.1 Effects of segmentation number

Figure 19 – Time-encoded pCASL maps

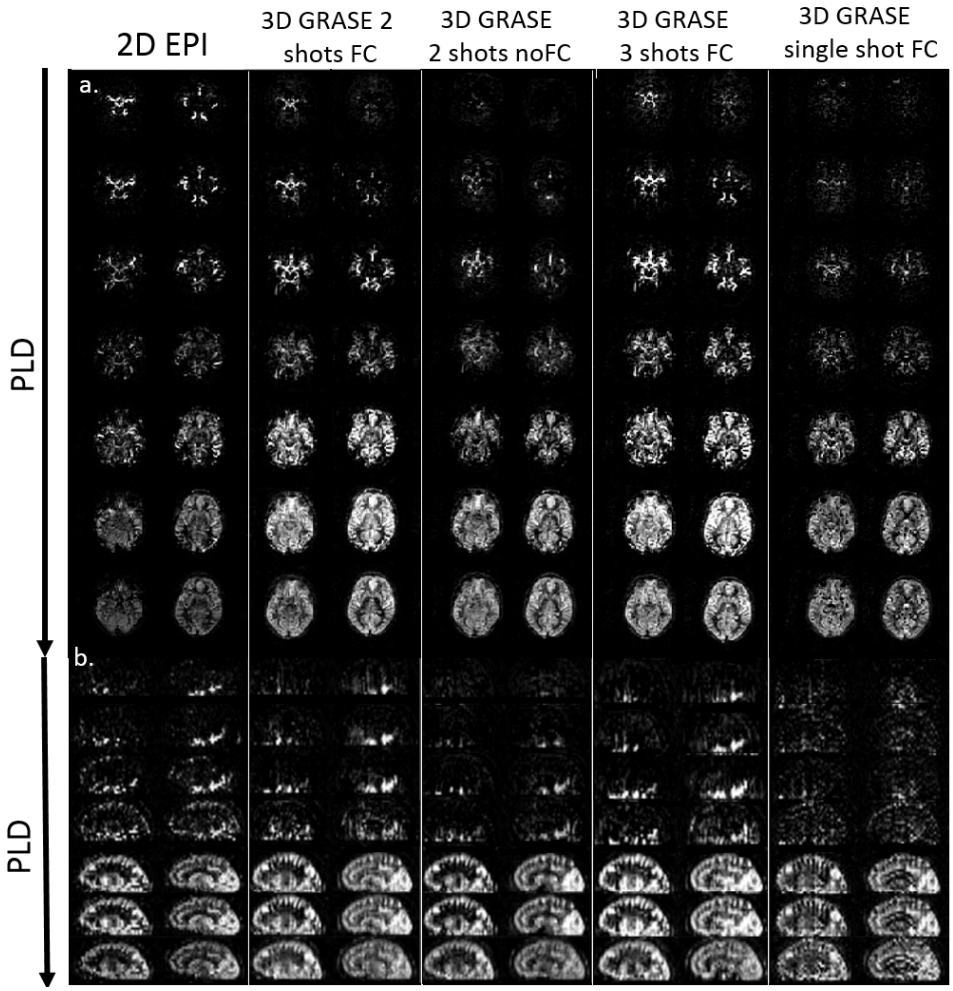

Two representative slices for all PLDs and readout schemes. (a) Axial view; (b) Sagittal view. Source: the author.

In Figure 19 two representative slices of ASL maps at multiple PLDs are shown in (A) axial and (B) sagittal views for 3d GRASE with different number of shots, and also for the 2D multislice EPI. Axial maps were used to calculate the tSNR maps (Figure 20) for two

representative PLDs to analyze the intravascular and the perfusion signal, while the sagittal maps were used to visualize the blurring in the z-direction. For a better analysis of the vascular signal, the arterial blood volume maps were calculated from the ASL maps, and Figure 21 show the results for the different number of segmentation acquired.

Figure 20 – tSNR maps for different readouts

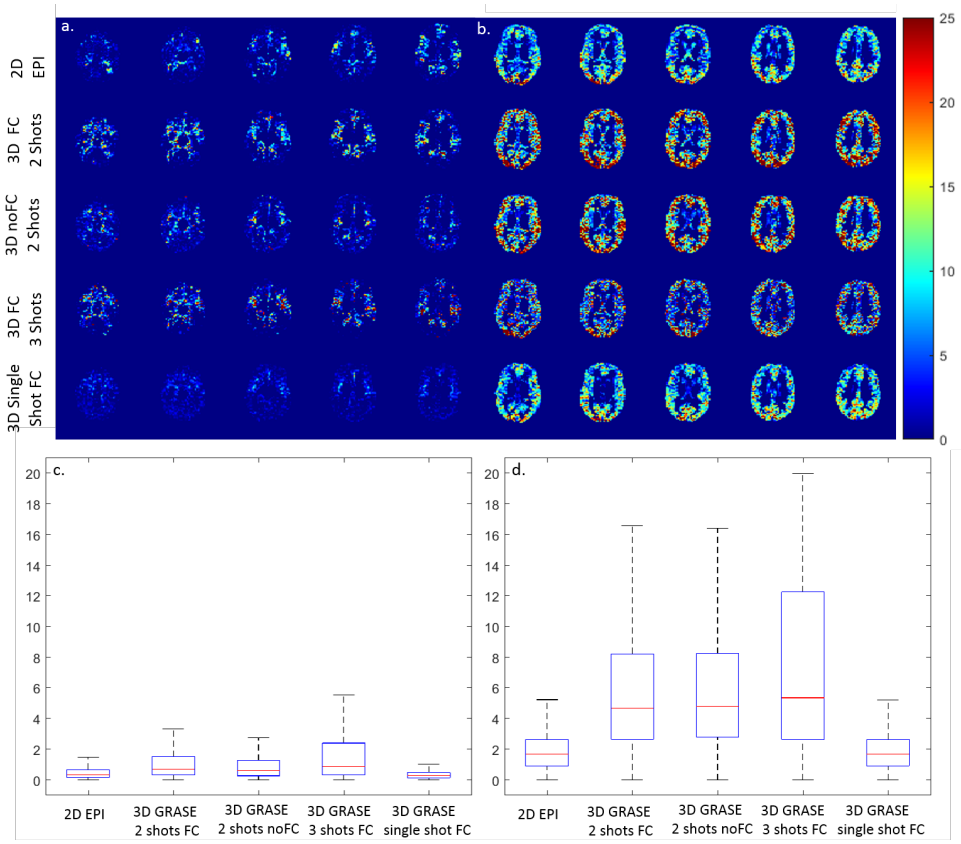

Temporal SNR calculated for all readouts at a PLD of 360ms (a and c) and 1860ms (b and d). Source: the author.

Figure 21 – aBV maps for different readouts

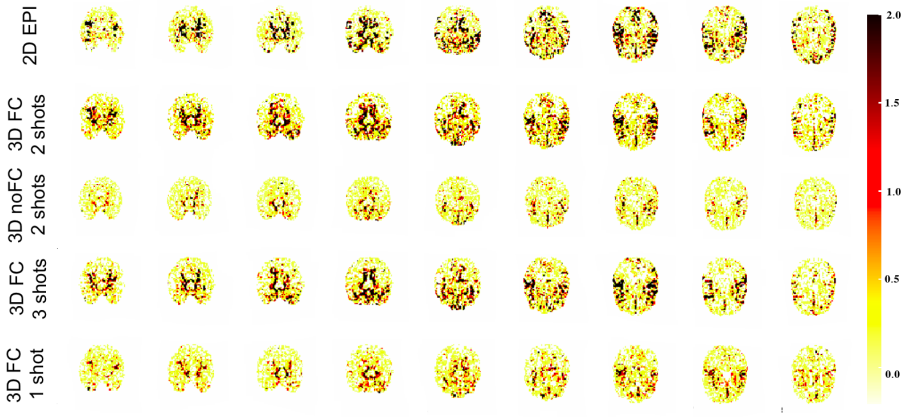

Arterial blood volume (aBV) maps quantified from the time-encoded pCASL data. Color bar shows aBV range in mL/100 g. Source: the author.

4.3.2 Effects of flow compensation scaling

Figure 22 – Time-encoded pCASL maps for different flow-compensation levels

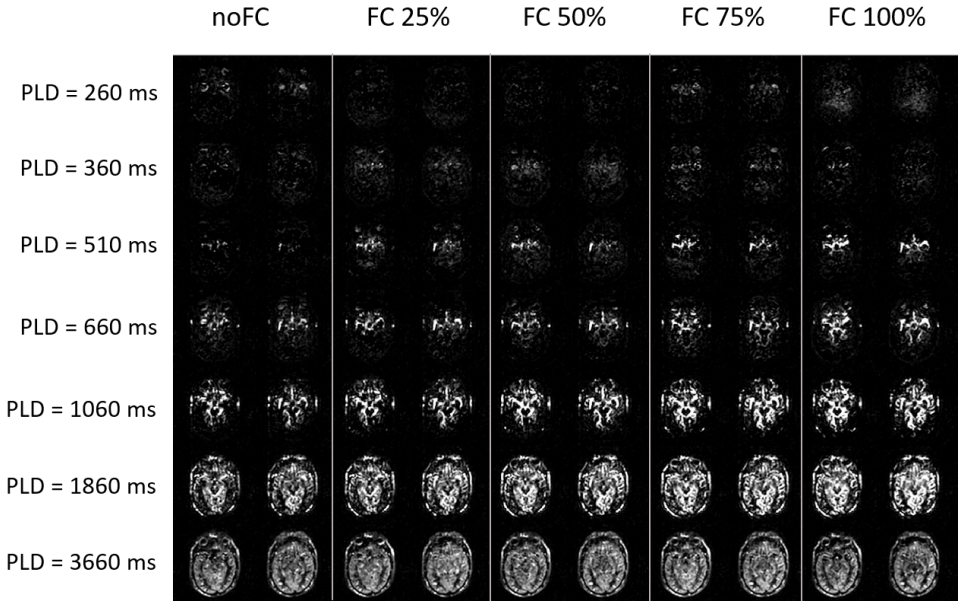

Two representative slices for all PLDs and each flow compensation (FC) level acquired. Source: the author.

The last experiment consisted in varying the intensity of flow compensation gradients (Figure 18) to scale the reduction of the dephasing effects arising from the moving spins in blood flow. This scale was performed for two-shot 3D GRASE te-pCASL, and the results are in Figure 22 for two representative slices at multiple PLDs. The tSNR maps for two representative PLDs is reported in Figure 23 as well as the statistical analysis for this measurement. Finally, aBV maps from the respective FC scaling is shown in Figure 24.

4.4 Discussion

In this study, the number of segmentation in 3D GRASE readout and the effect of the use of flow-compensation gradients were evaluated for a te-pCASL approach using a Hadamard-8 matrix to encode the labeling module. The number of segmentation represents a close connection between gains in SNR and the time efficiency for the total acquisition duration. Additionally, the use of flow compensation gradients consists of a complex relationship among increasing the TE, adding blurring in the vessels/brain boundary, and good visualization of the arterial compartment. Both factors are important to advanced applications of ASL, such as measurement of BBB permeability (155, 7) and oxygen extraction factor (25, 41).

In a visual inspection of the maps acquired with different readouts in Figure 19, the 2D EPI showed good results for time-encoded pCASL, allowing the visualization of both arterial and perfusion signal, albeit with lower SNR than segmented 3D GRASE (Figure 20). When using a single-shot 3D GRASE, the tSNR was comparable to the one obtained by 2D EPI for

Figure 23 – tSNR maps for different FC levels

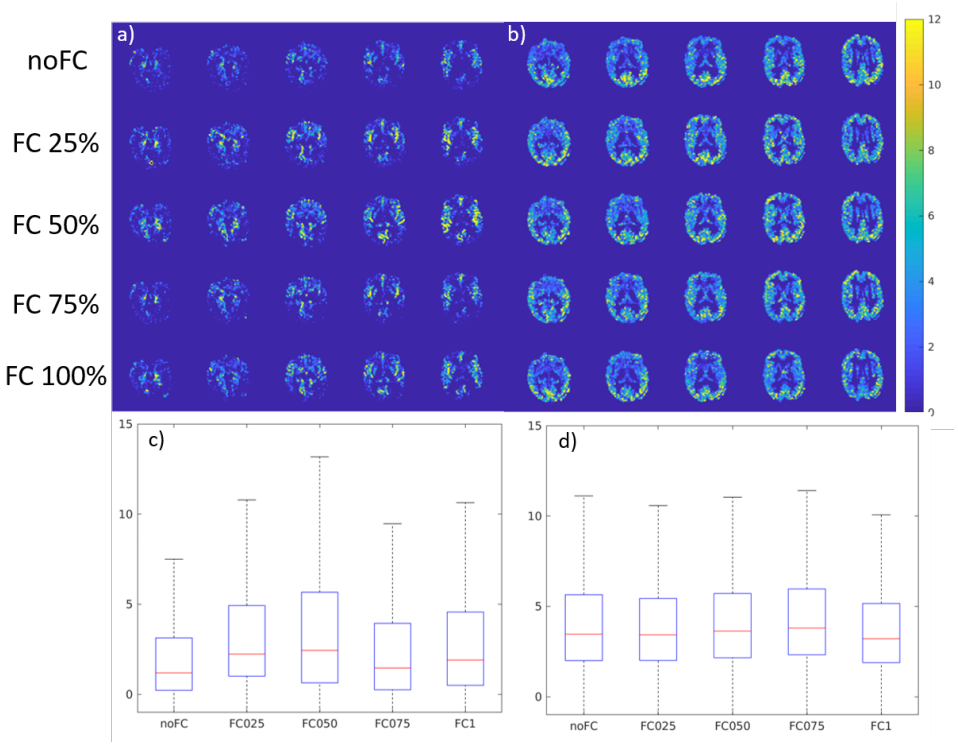

Temporal SNR calculated for different levels of flow compensation at a PLD of 360ms (a and c) and 1860ms (b and d). Source: the author.

Figure 24 – aBV maps for different FC levels

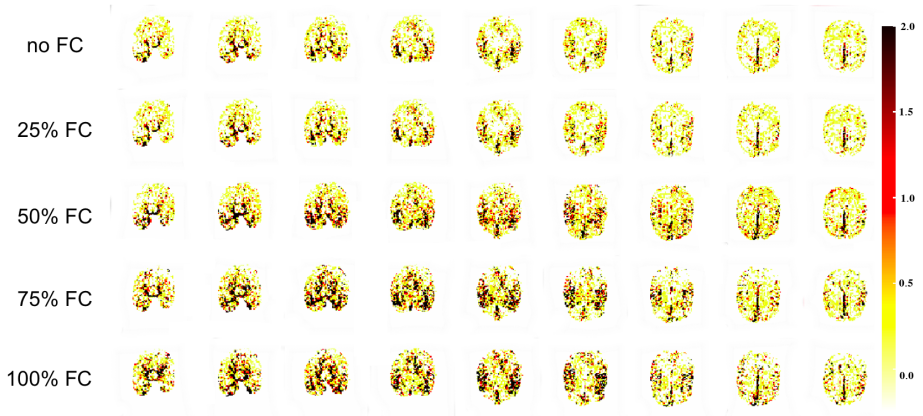

Arterial blood volume (aBV) maps quantified from the time-encoded pCASL data for each different flow compensation level. Color bar shows CBF range in mL/100 g. Source: the author.

perfusion signal (Figure 20b), in agreement to Feinberg et al (156), which analyzed the effects of the number of segmentation in a single-PLD 3D GRASE PASL data, but worse than for arterial signal (Figure 20 a and c). On the other hand, for two and three times segmented 3D GRASE, the obtained tSNR was higher for both perfusion and arterial signal when compared to the 2D EPI (Figure 20a). The aBV maps in Figure 21 show a better delineation of the arterial signal when the first order FC was employed, and when two and three shots were performed.

Regarding the blurring effects on 3D GRASE data, the present results for te-pCASL showed considerable less blurring for segmented acquisition when compared two the single-shot readout, also in agreement to previously reported studies (156, 157).

Although the non-recommendation in a standard ASL sequence for clinical routine (31), the scaling of the flow compensation experiment plays a big role in recovering the vascular signal (158, 159, 160, 24). The present results revealed that the visualization of the intravascular signal at PLDs of 510 ms and 660 ms was restored (Figure 22). However, at a PLD of 510 ms, a good visualization of the intravascular signal was achieved only using 75% or more of FC gradient-strength (Figure 23b). When the inflow blood started to fuel the cerebral arteries, at the PLD of 310 ms, only with full flow compensation gradients, it was possible to depict the intravascular signal (Figure 23a). The inspection of aBV maps in Figure 24 also shows a better visualization starting from 75% of flow compensation (160). Regarding the perfusion signal, all FC settings resulted in good signal quality.

In conclusion, this study showed higher effective tSNR for segmented GRASE compared to 2D-EPI and single-shot GRASE. Based on the presented results, we recommend the use of two or three shots for 3D GRASE. Flow crushing properties of the GRASE readout module should be carefully controlled when applying it for time-encoded pCASL. The use of full FC is essential to visualize the inflow blood through the intravascular signal since, without FC, the vascular signal is considerably crushed. When single-shot readout is required, 3D GRASE and multi-slice EPI provide similar results regarding the tSNR.

5 Intravoxel Incoherent Motion MRI in Neurological and Cerebrovascular Diseases

5.1 Abstract

Intravoxel Incoherent Motion (IVIM) is a recently rediscovered noninvasive magnetic resonance imaging (MRI) method based on diffusion-weighted imaging. It enables the separation of the intravoxel signal into diffusion due to Brownian motion and perfusion-related contributions and provides important information on microperfusion in the tissue and therefore it is a promising tool for applications in neurological and neurovascular diseases. This review focuses on the basic principles and outputs of IVIM and details its major applications in the brain, such as stroke, tumor, and cerebral small vessel disease. A bi-exponential model that considers two different compartments, namely capillaries, and medium-sized vessels, has been frequently used for the description of the IVIM signal and may be important in those clinical applications cited before. Moreover, the combination of IVIM and arterial spin labeling MRI enables the estimation of water permeability across the blood-brain barrier (BBB), suggesting a potential imaging biomarker for disrupted-BBB diseases.

5.2 Introduction

Perfusion refers to the passage of blood delivering nutrients and oxygen to the tissue in the capillary bed (161). It is an important mechanism of the brain metabolism and plays a crucial role in its normal operation. It is directly involved with regulatory mechanisms (e.g. autoregulation of blood flow, vascular reactivity, and hyperemia) that once unregulated result in cerebral disorders (162), such as stroke, dementia and cognitive deficits.

In the brain, perfusion is classically quantified as cerebral blood flow (CBF) which consists of blood volume per unit of brain tissue per unit of time, usually given in mL/100 g/min (163). However, other metrics can be estimated depending on the imaging method. Among several methods, intravoxel incoherent motion (IVIM) estimates brain perfusion based on magnetic resonance imaging (MRI) (72). Other approaches are also based on MRI, nuclear medicine and optics (164, 165).

MRI-based perfusion methods include dynamic contrast enhancement (DCE), dynamic susceptibility contrast (DSC), arterial spin labeling (ASL) (164), and IVIM. The former two techniques are based on the concept of a bolus of blood volume transiting through the tissue. DCE provides information about Ktrans (volumetric transfer constant between blood plasma and extracellular extravascular space (EES)) (166), permeability-surface area product, and cerebral blood volume (CBV) (167, 168). However, the latter is not usually assessed. DSC,

the best choice for brain evaluation in clinical settings, provides a relative measurement of CBV, mean transit time (MTT), time to peak (TTP) and an estimation of CBF. ASL is a noninvasive alternative that assesses perfusion through quantification of CBF, which takes advantage of the hydrogen in the arterial blood as an endogenous tracer (75, 169, 23).

In the late 1980's, Le Bihan designed IVIM, another approach that measures perfusion-related parameters using MRI noninvasively (72). Multiple diffusion-weighted images (DWI) were acquired varying the diffusion gradient weighting. The amplitude of the resulted signal decays exponentially as the diffusion weighting increases. This decay is fitted to a theoretical model to separate diffusion and perfusion contributions of the signal (73). A detailed explanation is provided is section 2.

Initially, IVIM drew interest for applications in liver and kidney. Several studies proved its usefulness (170, 171, 172, 124, 173). Despite having been initially tested for cerebral imaging, due to its high fractional anisotropy, the existence of several other established imaging methods, and the lack of a consensus about the best fitting method to adjust the signal to a physiological model, IVIM was not very well explored a priori. However, a better physiological description of IVIM signal and emergence of optimized fitting approaches have increased the application of IVIM in the brain over the past years.

This review provides an overview of the IVIM technique and addresses its main applications in the brain and future directions regarding its use for the study and evaluation of neurological and neurovascular diseases. The combination of IVIM with ASL and their complementarity are also discussed.

5.3 Theoretical considerations

5.3.1 The concept of the IVIM signal

Water molecules in a fluid exhibit microscopic random translational motion, called Brownian motion (174), which results in molecular diffusion. The mean square distance traveled by a molecule is proportional to time and to the diffusion coefficient (D). The latter coefficient depends on diffusing molecules, fluid viscosity, and temperature. At the capillary bed, besides the free water diffusion, the water molecules also flow (175), due to the blood flow. Therefore, in the vascular compartment, the molecular diffusion path is limited by the vessel wall and influenced by the fluid viscosity and blood flow, which results in another diffusion contribution, modulated by a different coefficient, the pseudo-diffusion coefficient (D^*), one order of magnitude greater than coefficient D and first described by Le Bihan in 1986 (72).

Restrictions imposed on diffusion motion (65) are measured by MR experiments through the application of magnetic field gradients and result in diffusion-weighted images

(66, 67). After the use of those gradients, the MR signal decays exponentially according to the diffusion coefficient and the b-value, introduced by Stejskal and Tanner in 1965 (176) and refers to the weighting of the diffusion pulse sequence. The b-value, expressed in s/mm^2, depends on the diffusion gradient waveform, the time duration of the gradients and the interval between them, according to Equation 5.1 and 5.2:

$$b = (2\pi)^2 \int_0^{TE} \vec{K}_{(t)} * \vec{K}_{(t)} \, dt \tag{5.1}$$

$$\vec{K}_{(t)} = \frac{\gamma}{2\pi} \int_0^{t} \vec{G}_{(t')} \, dt' \tag{5.2}$$

where γ is the gyromagnetic ratio, G is the diffusion gradient magnitude in mT/m and t is the time duration of the application of the gradient pulse.

If the signal is measured in a pure solution, where the only source of motion is Brownian due to thermal diffusion, the MR signal can be expressed by a single exponential equation:

$$\frac{S_{(b)}}{S_0} = e^{-bD} \tag{5.3}$$

where S(b) represents the signal acquired at a specific b-value and S0 is the signal with no application of diffusion gradients.

When the signal comes from a biological tissue, some factors reduce the diffusion motion, such that it decays according to a different diffusion coefficient, called apparent diffusion coefficient (ADC) (72) which is the sum of contribution of all diffusion coefficients related the resulting motion. Under such a condition, diffusion MR signal can be expressed by:

$$\frac{S_{(b)}}{S_0} = e^{-bADC} \tag{5.4}$$

which is the representation of the diffusion mono-exponential model.

Several components account for the total ADC under biological conditions. However, in comparison to contributions of thermal diffusion and flowing effects, other sources can be neglected, and the signal can be modeled through a bi-exponential model (Equation 5.5), in which each exponential amplitude depends on the blood volume perfusion fraction (f) in a way the sum of those amplitudes must be one.

$$\frac{S_{(b)}}{S_0} = f e^{-bD^*} + (1-f) e^{-bD} \tag{5.5}$$

Equation 5.5 describes the IVIM signal where D is the diffusion coefficient of free water, D^* is the pseudo-diffusion coefficient, f is the perfusion fraction and b is the b-value.

The idea beyond the IVIM method is to separate those contributions through the mapping of D, D^* and f (Figure 25). Each map contributes with different information, which, combined, helps the understanding of the water movement. Perfusion fraction f represents the volume of blood flowing into the capillary, whose water movement has the contribution of the blood flow and the diffusion motion within a single voxel. All such motions are summarized into pseudo-diffusion coefficient D^*. Thus, with the parameters f and D^*, IVIM provides the perfusion contribution to the MR signal. Although D^* maps are noisier than the others (Figure 25b), studies in the literature have shown their utility, as discussed in section 2.1. The omission of D^* maps might result in the loss of useful information. On the other hand, D is the pure water diffusion coefficient and represents a voxel diffusion contribution to the signal in the extra-vascular pool.

Figure 25 – IVIM maps

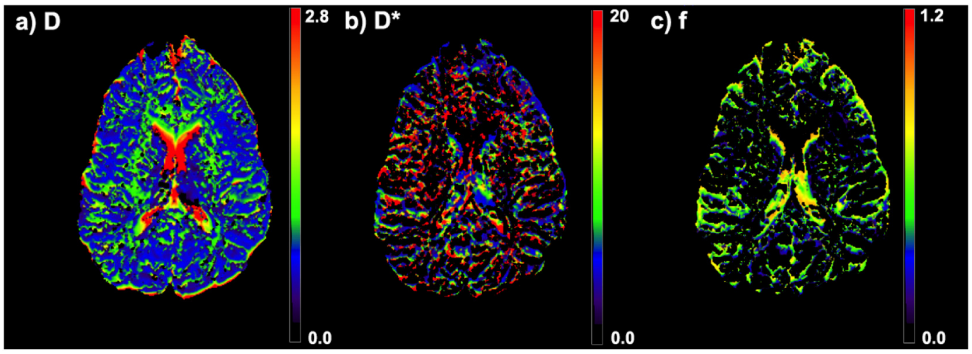

Examples of D, f and D^* maps. Source: the author.

Since D^* is one order of magnitude higher than D, the exponential decay with the pseudo-diffusion coefficient vanishes faster, and its contribution to the total signal is distinguishable only at low b-values. At higher b-values, the contribution of the exponential with D models the signal. Multiple b-values are necessary to estimate from which b-value there is only diffusion contribution and consequently to estimate D, D^* and f precisely (Figure 26). Le Bihan proposed acquisition with only three b-values, which are theoretically enough for the obtaining of IVIM outputs. However, more points are necessary especially for the brain due to noise contamination and low D/f ratio, i. e., 0.5%, in comparison to 3.5% in the liver, for example (29). Such a small percentage of perfusion contribution requires oversampling of low b-values. Therefore, between 10 and 30 b-values are usually employed, and the maximum b-value ranges from 1000 to 2000 s/mm^2 (177).

The IVIM signal represents approximately 5% of the total diffusion signal, which motivated Neil et al. to develop strategies for suppressing the diffusion contribution and better understanding the IVIM signal (178). The approach used was the injection of a contrast agent for decreasing T1 and selectively suppressing the signal of non-flowing components. Once the diffusion contribution had been suppressed, the authors expected to fit the resulted signal by a mono-exponential model. However, they observed the signal was better adjusted

Figure 26 – IVIM signal decay

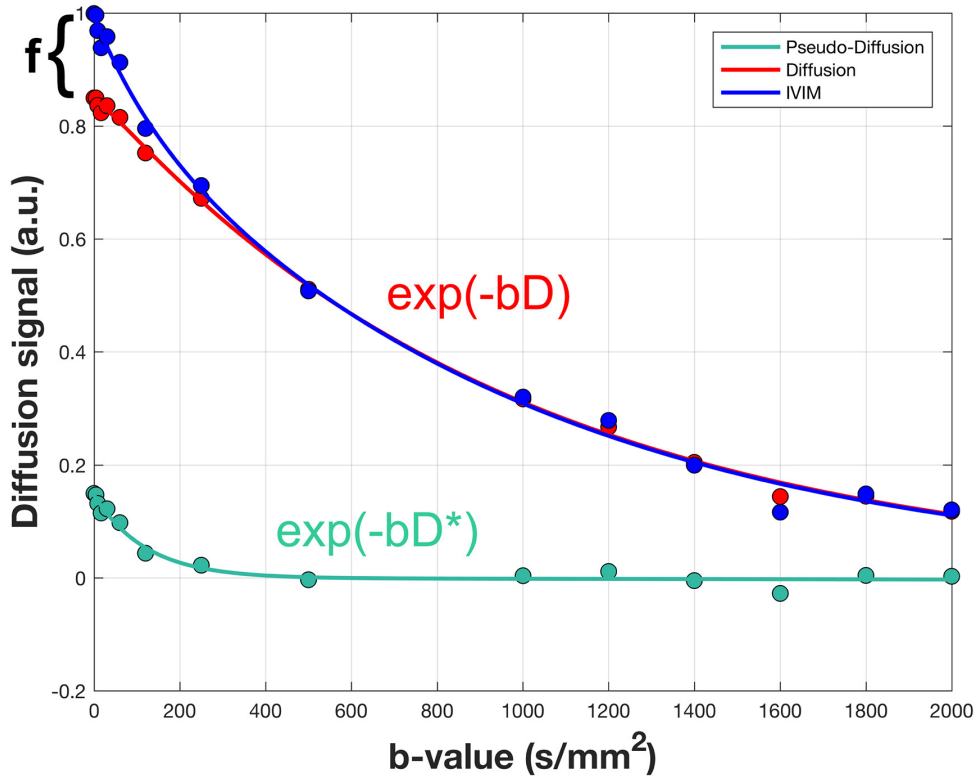

Example of Pseudo-Diffusion (green) and Diffusion (red) contributions to IVIM signal (blue). Pseudo-diffusion (D^*) and diffusion coefficients (D) are extracted from the exponential decay of green and red curves, respectively. Perfusion fraction f is obtained from the difference of the intercept of blue and red curves. Source: the author.

through a bi-exponential approach. Other studies also investigated that behavior towards explaining the results (179, 180, 181).

Fournet et al. described a more specific bi-exponential model (182) that considers two different compartments, namely capillaries, and medium-sized vessels. The authors hypothesized the bi-exponential behavior reflected the contribution of flow through two different vascular pools. The slow and fast pools represent capillaries and medium-sized vessels, respectively. That differs from classical IVIM models that consider a single compartment: the intravascular. At high b-values, both models converge to the mono-exponential decay, however, at low b-values, the signal is better fitted considering two pools. Such information helps the understanding of the IVIM signal and can also be useful for clinical applications.

5.3.2 Physiological models and fitting approaches

Since IVIM was proposed in 1986, several models were developed to explain the physiology related to the IVIM signal (physiological models) and others to better fit the acquired signal resulting in more trustful output maps (fitting models/approaches). However, there is some confusion in the literature about the terminology employed to classify all these models, especially about the bi-exponential terminology that is recurrently used to refer to

both physiological and fitting models.

5.3.2.1 Physiological models

Physiological models aim to explain the nature of the measured IVIM signal. Le Bihan et al. (1988) introduced the two first models, the mono-exponential and sinc models. Part of the confusion on terminology is related to the mono-exponential model since it is described by an equation of two exponential terms (Equation 5.5). It is referred to as mono-exponential because only one compartment (the intravascular one) is used for explaining the pseudo-diffusion contribution to a single exponential term. On the other hand, Fournet's bi-exponential IVIM model considers two compartments, namely capillaries and medium-sized vessels, to explain the pseudo-diffusion and perfusion related information (182). Therefore, the use of mono- and bi-compartment models may help to end the confusion.

5.3.2.2 Fitting models

The main step of the IVIM data analysis consists of fitting the measured signal to a theoretical model and, consequently, researches have focused on the optimization of the fitting approaches. Classically, the IVIM signal is fitted through a two-step mono-exponential analysis. First, the diffusion coefficient (D) is obtained from the mono-exponential fitting of the exponential decay for high b-values (usually higher than 200 s/mm^2). Then, a mono-exponential fitting of the exponential decay for low b-values is applied towards estimating the pseudo-diffusion coefficient (D^*) and perfusion fraction (f). The other usual fitting model is the bi-exponential, which tries to adjust the entire curve including all b-values to obtain D, D^* and f. The approach is commonly used for the mono-exponential physiological model.

Several studies have implemented more robust models for fitting the IVIM signal, e.g. kurtosis model, non-negative least squares (NNLS), models that use artificial neural network and Bayesian approaches. Details can be found in (183, 184, 185).

5.3.3 IVIM and classical perfusion measurements

IVIM emerged as a different approach for the obtaining of perfusion information and studies have aimed to correlate IVIM outputs with standard perfusion-related measures, as CBF and CBV (186, 187, 188).

Conventional perfusion can be assessed by nuclear medicine techniques, as positron emission tomography (PET) and single photon emission computed tomography (SPECT). In both techniques, a bolus of exogenous tracer is intravenously injected for tagging the arterial blood with radioisotopes. Emissions from radioisotopes enable the estimation of the delivery of nutrients, as oxygen, glucose and tracer injected in the tissues, which results in the measurement of CBF in physiological units, mL/100 g of tissue/min (163).

MRI-based DSC and DCE are well established methods applied in clinical routine for the assessment of perfusion (189). DSC uses T2*-weighted images of high temporal resolution to calculate perfusion-related metrics (CBV, MTT and TTP), towards CBF estimation. On the other hand, DCE – originally a technique to assess permeability of blood-brain barrier (BBB) – estimates CBF and CBV according to dynamic T1-weighted images and classic permeability parameters, as volume transfer constant (Ktrans) and plasma volume (Vp). It is the best option for the study of neck, breast, and abdomen, which are regions of high field inhomogeneities due to fat, bone and air interfaces that suffer from susceptibility artifacts in T2*-weighted images. However, both methods require an intravenous injection of gadolinium. Besides concerns regarding its deposition in the brain, some factors hamper the quantification of perfusion-related parameters – e.g. gauge of the venous access that limits injection velocity; physical characteristics of the contrast agent, as temperature and viscosity; characteristics of the injection pump; the injection protocol, and characteristics of patients, as arterial blood pressure and atherosclerosis.

In ASL, labeled blood flows through capillaries, delivers nutrients and oxygen to the brain tissue, and exchanges magnetization. The approach consists in the magnetic labeling of the arterial blood through the application of radiofrequency pulses. After the labeled blood has reached the slices of interest, the image is acquired and then subtracted from a label-free image acquired at the same position, which results in a perfusion map proportional to the CBF (60, 80) that takes into account some physiological and acquisition parameters (31).

On the other hand, IVIM perfusion measures all water motion contributions to the intravoxel signal, as the Brownian motion of free water at perivascular space, the microperfusion signal of water flowing in randomly distributed microvasculature and flowing blood inside arteries. Since f represents the volume fraction of the intravascular blood and D^* refers to pseudo-diffusion motions related to blood flow, these measurements can be connected to those of classical methods. The first hypothesis proposed by Le Bihan and colleagues (29, 188) suggests the link is related to capillary network geometry, as described by:

$$f_{IVIM} = \frac{CBV}{f_w} \tag{5.6}$$

$$MTT = \frac{L}{v} = \frac{Ll}{6D^*} \tag{5.7}$$

$$CBF = \frac{6f_w}{Ll} f_{IVIM} D^* \tag{5.8}$$

where f_w is the MRI-visible water content fraction, L is the total capillary length, l is the mean capillary segment length and v is the average blood velocity. Therefore, CBF is related to IVIM perfusion through product fD^*.

Recent studies have compared the blood flow measured with ASL and fD^* measured with IVIM. Yao and colleagues showed the correlation between fD^* and ASL-CBF was fair to good for stroke patients (190). Liang and colleagues also obtained a good correlation with the renal cortex, but weak correlation when the whole kidney was considered (191). Wu and colleagues did not achieve the same good correlation for the brain (192). Therefore, the comparison between IVIM parameters and ASL-CBF is still inconclusive and must be clarified. However, more than comparing IVIM parameters with standard ones, it is important to understand their physiological meaning, since they may provide complementary and useful information.

5.4 Neurological and Neurovascular applications

The analysis of neurological and neurovascular diseases revealed that measures of perfusion provide essential information for the patient's diagnosis and the disease characterization and monitoring. IVIM is an imaging tool that represents a new insight in perfusion measurements combined with simultaneously acquired diffusion information. Since its development, some applications for IVIM such as glioma grading, tumor diagnosis, stroke and cerebral death have been reported (193), and once the results have proven positive, their range has been extended over the past few years.

5.4.1 Cerebrovascular diseases

5.4.1.1 Stroke

Stroke is the second leading cause of death worldwide (1), therefore, it has been the subject of extensive studies regarding its characterization, diagnosis, and tissue lesion progression. Besides structural sequences, as T2W, T1W and T2-FLAIR (fluid attenuation inversion recovery), the standard protocols used for stroke evaluation include DWI and perfusion-weighted imaging. The current perfusion mapping is mostly performed by DSC, DCE and, more recently ASL methods (194, 195, 196). Measurements of perfusion in stroke aim to assess the reduction of regional blood flow, volume and transit time through maps of CBF, CBV, and MTT respectively. However, DSC and DCE use gadolinium-based contrast injected in peripheral veins and are highly dependent on hemodynamics impairment, stenosis of proximal large arteries and velocity of contrast injection. Moreover, they provide information mainly from large vessels rather than the microvasculature (197). On the other hand, the use of ASL, the classic non-contrast-agent technique, strongly depends on changes in the arterial arrival time and may provide underestimated CBF values (198).

IVIM provides intrinsically local information, and is nondependent on the regional effects of big arteries and peripheral hemodynamic impairment or problems related to gadolinium injection. It also provides absolute perfusion and diffusion information with a single

three-minute sequence. According to IVIM-based maps, information from D or ADC enables the anatomical determination of stroke lesions since it indicates the degree of diffusion restriction of water molecules (199). Simultaneously, due to incoherent motion, perfusion information is also available (f map) making it possible to determine if it is from intra- or extravascular medium.

The assessment of stroke by IVIM was first reported by Wirestam et al. (200). Perfusion fraction f was reduced in affected areas in comparison to the respective contralateral region. After that study, stroke evaluation by IVIM was not reported until 2014, when Federau et al. revisited (201). In agreement with the previous study (200), the authors also reported a reduction in perfusion fraction f in 14 out of 17 patients. The novelty was the combined analysis of quantitative maps of ADC and f (Figure 27b and c), which provided information about the penumbra region.

Figure 27 – IVIM application in stroke

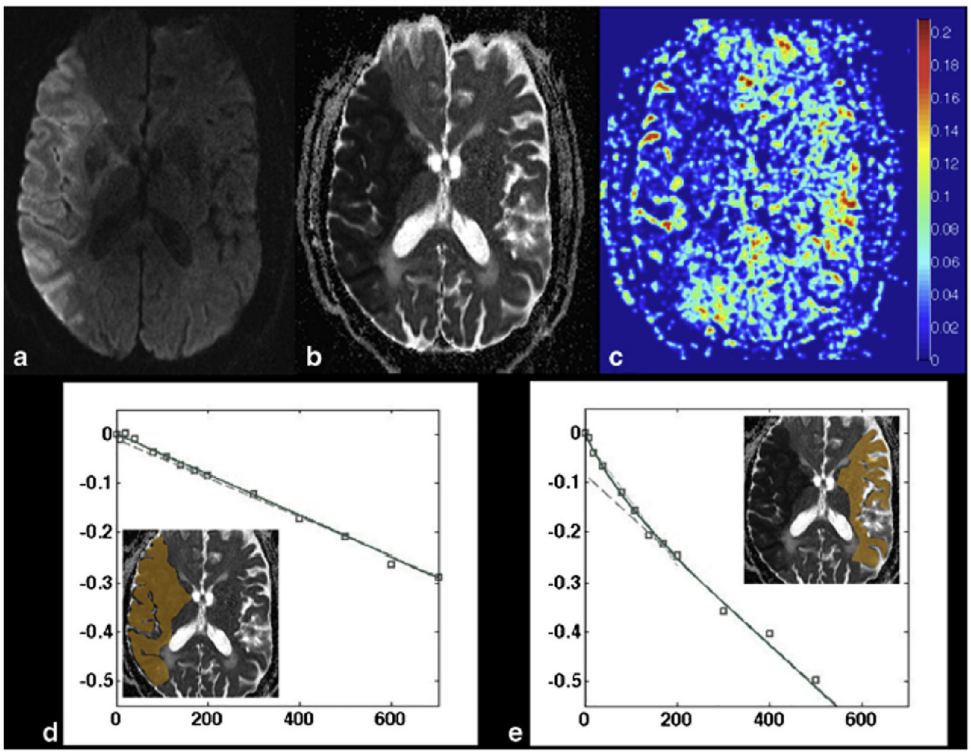

Example of a patient with a stroke in the middle cerebral artery territory. a) Raw image (b= 900 s/mm^2). b) ADC map. c) Perfusion fraction map. d) IVIM fitting in the stroke area. e) IVIM fitting in the contralateral hemisphere (201).

Other studies reported the possible use of different IVIM outputs, as maps of D, ADC, D^*, f, and fD^* for analysis of affected regions (202, 190). The authors concluded f and fD^* are more sensitive to detect changes during the stroke process, as these parameters are more related to CBF, with similar results to those obtained using ASL. In a different analysis, Suo et al. evaluated the correlation between ADC and IVIM-derived parameters and showed that for stroke lesions this correlation is different in comparison to normal tissue. Such a

difference is clear in the analysis of the scatter plot of the correlations, where stroke areas can be distinguished, especially for the ADC-f correlation (203).

5.4.1.2 Cerebral small vessel disease

A novel application of IVIM refers to the assessment of patients with cerebral small vessels disease (cSVD), a common microvascular pathology that can progress to complications such as lacunar stroke, leukoaraiosis and vascular dementia (204, 3). Such patients have reported alterations in the parenchyma, lacunes, enlarged perivascular spaces (PVS) and atrophy, which result in structural MRI abnormalities, as hyperintensities and microbleeds (205, 206, 207, 208, 209, 210, 211, 212, 213). Although the identification of cSVD through conventional MRI is relatively easy, finding indications of normal appearing white matter (NAWM) that can advance to cSVD is still a challenge.

Perfusion images have shown a reduction in white matter CBF for cSVD patients (214, 215), while DWI has also shown abnormalities (216). Wong et al. used FLAIR image to localize affected areas (Figure 28) and IVIM to estimate perfusion fraction f (Figure 28b) (217). They observed an increase in f values for both affected areas and in regions of FLAIR-NAWM, which is contrary to previous perfusion-based studies in cSVD. The results may be an evidence of vasodilation to increase the blood flow in those regions to suppress the cognition loss effects. Other possible explanations include deregulation in blood-brain barrier (BBB) and effects of increased vessel tortuosity. Even though the authors showed that IVIM might be useful to indicate affected regions before structural MRI, future studies must investigate the mechanism more carefully.

5.4.2 Tumor

Brain tumors deriving from cells of the central nervous system (CNS) are classified into benign and malignant. The most common malignant brain tumors are diffuse gliomas, mainly astrocytomas, and glioblastomas (218). Due to their high mortality rate, early diagnosis and precise characterization are crucial to the treatment prospectus. Clinically, DSC and DWI are commonly used to help the diagnosis in case of tumor suspicion (219). Therefore, tumors have quickly become an important target of application for IVIM that provides perfusion and diffusion information (193).

5.4.2.1 Glioma

Glial tumors represent over 50% of primary brain neoplasms and approximately 80% of all malignant brain tumors (220). Term glioma refers to all glial tumors, however diffuse gliomas (grades II to IV) are more critical than low proliferative and well-delimitated gliomas (grade I), which enable complete surgical resection. Diffuse gliomas are divided into low grade glioma (LGG) or grade II, high grade glioma (HGG) or grade III), and glioblastoma (GBM,

Figure 28 – IVIM application in cerebral small vessels disease

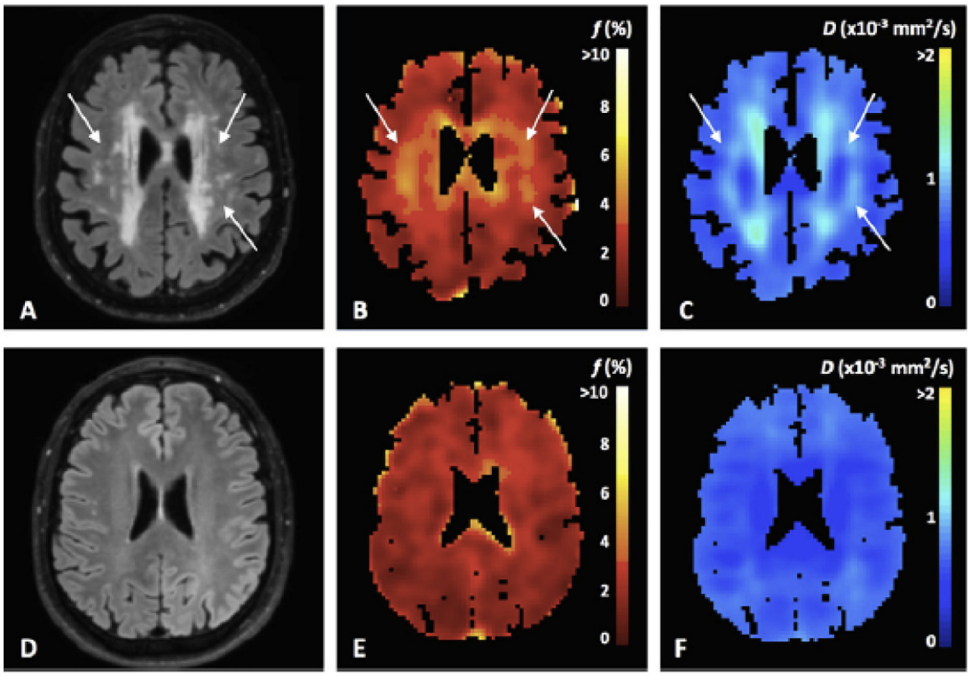

Example of FLAIR images (A, D), perfusion fraction f maps (B, E) and parenchymal diffusivity D (C, F) for a small vessel disease patient (top row) and a healthy subject (bottom row) (217).

grade IV), according to the World Health Organization (WHO) (221). Histologically, grade II gliomas have well-differentiated cells, and patients have an average survival of 5 to 10 years after diagnosis. Grade III anaplastic oligodendrogliomas or astrocytomas show anaplasia and mitotic activity and patients usually survive less than 5 years. Grade IV GBM shows further microvascular proliferation and necrosis and is associated with less than two-year average survival. Because of such differences, therapeutic strategies are different, and the grading of diffuse gliomas is crucial.

Bisdas showed the first evidence that IVIM could provide useful information in grading gliomas (74). They reported both D^* and f could be used to differentiate gliomas since these parameters were higher in HGG in comparison to LGG, which is consistent with the patho-physiology of the disease. Other researchers have reported similar results and emphasized IVIM-derived parameters could be used as markers for the diagnosis of glioma (222, 223).

According to Hu et al. ADC and D were significantly lower in HGG in comparison to LGG and, similarly to previous studies, D^* at tumor site showed higher values for HGG (224). However, the authors found lower f values for HGG, possibly due to the use of different b-values, especially for lower ones, and to ROI selection that, in contrast to other studies, included the solid tumor with the highest signal intensity on DWI. Moreover, the highest cellularity density, nuclear-cytoplasmic ratio, and relatively fewer mesenchymal components are present in anaplastic gliomas and glioblastomas (225), which are possible sources of reduction in perfusion fraction (74, 222).

There are also reports on IVIM to differentiate between glioblastoma, metastasis and primary central nervous system lymphoma (PCNSL) (226, 227, 228). Other researchers reported ADC obtained from a mono-exponential model of DWI could differentiate glioblastoma from PCNSL (229, 230, 231, 232). However, there is evidence that perfusion effects enhance this difference in ADC within the affected region. Suh et al. used the bi-exponential model to separate perfusion and diffusion information on the IVIM signal and found no significant difference in the D coefficient comparing PNCSL and glioblastoma. They suggested the difference in ADC was related to perfusion (227) which was confirmed through the analysis of the perfusion fraction f higher in glioblastoma than in PNCSL, such a result is in agreement with histological examination, once the level of cellularity in tumors is higher in comparison to normal tissue (230, 231, 232).

5.4.2.2 Tumor monitoring

IVIM parameters have been used in the monitoring of tumors in patients treated with drugs, as antiangiogenic and vascular target agents applied outside the brain (233, 234, 235, 236, 237).

Detsky and colleagues used IVIM imaging to investigate patients subjected to stereotactic radiotherapy (238), and differentiate radiation necrosis from tumor progression. This differentiation is crucial for the continuation of or changes in the treatment. A signal enhancement in conventional MRI for both tumor progression and radiation necrosis hampers differentiation, although occurring in different scales. Detsky et al. showed perfusion fraction f might be useful for that differentiation (Figure 29). The perfusion fraction map is uniformly low in the affected region for the radiation necrosis (top row of Figure 29), whereas for tumor recurrence, it is more heterogeneous and shows higher perfusion fraction values (bottom row of Figure 29). However, such findings must be validated in a larger cohort.

5.5 Combination of IVIM and ASL

Recent studies have documented gadolinium deposits in the brain and adverse effects in several subjects (239, 240, 241, 242). As addressed in section 1, an accurate estimation of perfusion parameters based on DSC and DCE depends on different factors, including injection protocol and patients' anatomical vascularization. Therefore, a combination of ASL and IVIM may render a possible diagnostic benefit without the use of gadolinium.

Early ASL models assumed the labeled arterial blood could be classified as a freely diffusible tracer (75). However, other studies have reported the assumption is not completely valid, due to regulatory mechanisms of BBB that reduce water permeability according to the tissue necessity (243, 244, 245, 246). Researchers started to assess the ASL signal through a two-compartment model that considers BBB permeability. ASL images acquired at multiple

Figure 29 – IVIM application in tumor monitoring

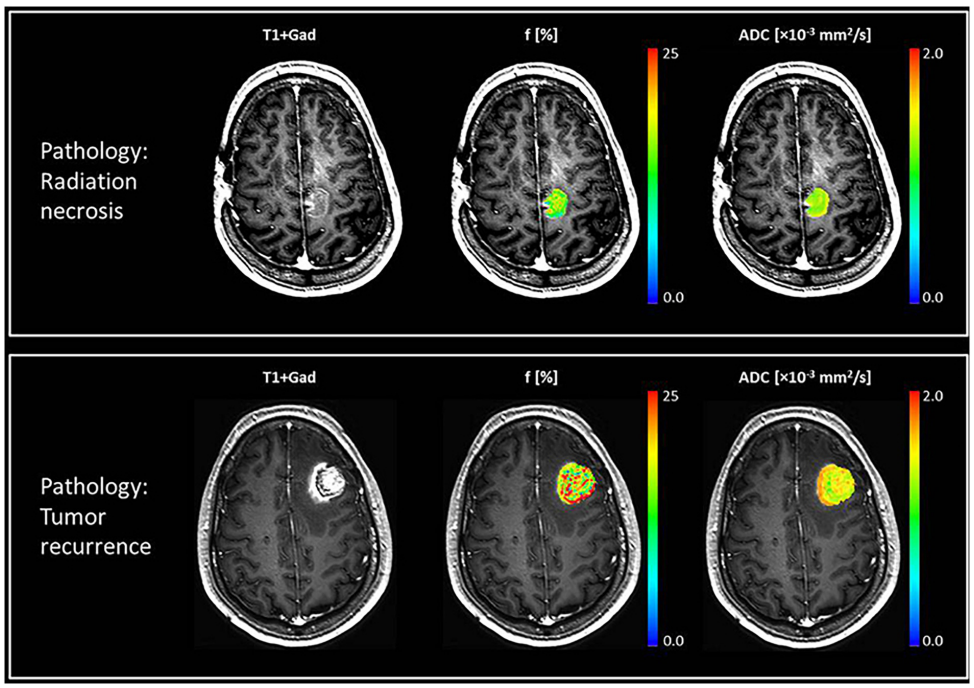

Example of IVIM parameter maps for a patient with radiation necrosis (top row) and another with tumor recurrence (bottom row) (238).

inflow times, which is known as multi-TI/PLD ASL, are an alternative for the obtaining of the BBB permeability resulted from a fitting model. However, the origin of ASL signal must be investigated through its splitting into intravascular and extravascular contributions, which can be done with IVIM. Therefore, a combination of ASL and IVIM started to be considered.

The combination of ASL and diffusion gradients was first described by Wang et al. (6), who used a hybrid sequence of continuous ASL and the twice-refocused spin-echo method for acquiring images with different b-values at three different post-labeling delays (PLDs). They estimated the BBB permeability to water through the bi-exponential model. Lawrence et al. reported a similar study but using a two-stage approach (7). First, the hybrid ASL.-DWI sequence was used in the estimation of b-values necessary for the separation of extra and intravascular components of the ASL signal. Using only the chosen b-values and varying the PLD, the authors acquired images that enabled the calculation of each contribution to the signal (Figure 30).

Other studies have aimed at better results of BBB permeability and understanding of the origin of the MRI perfusion signal (8, 247). The results of the combination of ASL and IVIM methods are promising and suggest a possible new imaging tool for the assessment of water exchange across BBB, providing important information about diseases as tumor and cSVD, and neurodegeneration.

Figure 30 – Combination of IVIM and ASL

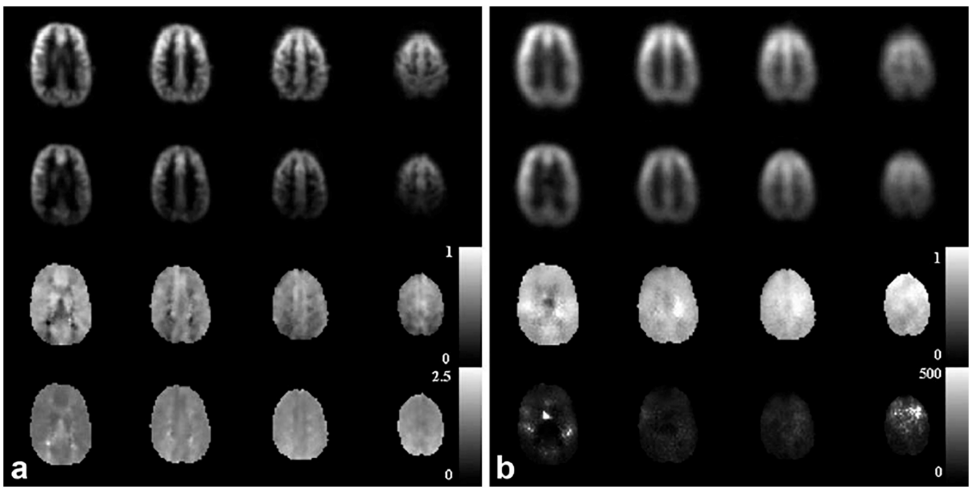

Examples of ASL-DWI images. For both figures a and b, first row shows the average diffusion-weighted (ΔM) maps for b_0; second row shows ΔM including diffusion weighting (b_{dw}); third row shows the ratio $\Delta M(b_{dw})/\Delta M(b_0)$. In fourth row, in figure a it is shown the Transit time to the capillary-tissue compartment (τ_a) while in figure b it is presented the exchange rate of water from blood to tissue (k_w) (7).

5.6 Conclusions

IVIM method is a diffusion-weighted MRI sequence for the estimation of perfusion parameters that offers several advantages in comparison to commonly used approaches. First, it is a noninvasive alternative for the measurement of perfusion with no intravenous injection of exogenous contrast agents, as gadolinium, and provides information on perfusion and diffusion simultaneously through a single image sequence, which shortens the exam. Third, its signal has high spatial specificity since it comes primarily from where the measure is achieved independently of the arterial blood path before arriving there. Finally, it provides complementary information in comparison to ASL and the combination of both methods can be useful for the assessment of neurological diseases.

However, for being a recently rediscovered method, especially for brain applications, IVIM is in development in almost every stage, such as acquisition, analysis, and applications. There is still discussion on how many b-values are necessary to obtain a reliable signal fitting, the maximum b-value to be acquired and the cutoff value where diffusion dominates the signal. Regarding analysis, physiological models and fitting strategies are still under investigation.

6 Non-negative least squares fitting model for IVIM data: simulation analysis and in vivo application

6.1 Abstract

Intravoxel incoherent motion (IVIM) is a DWI method that also allows the measurement of perfusion parameters. DWI are widely used in the clinical environment for the assessment of the spatial location of brain tumors, such as gliomas. Beyond such information, it is also possible to obtain simultaneous perfusion measurement if using IVIM. However, the fitting model plays a crucial role in the analysis of IVIM data due to the limited number of points and to typical noisy data. Also, injured tissues may present changes in the apparent diffusion coefficient (ADC) value so that the number of diffusion components that contribute to the total signal might be unknown. A possible solution for this problem is the utilization of non-negative least square (NNLS) fitting. This study aimed to evaluate the impact of the parameters used in this fitting algorithm and its applicability to simulated IVIM signal data processing. We also analyzed the use of the NNLS fitting model in patients with diffuse glioma to assess both diffusion and perfusion characteristics. Through such measurement, we aimed to enable the monitoring of whole-brain volume and tumor evolution regarding its structural and hemodynamic features.

6.2 Introduction

Diffusion-weighted image (DWI) is a magnetic resonance imaging (MRI) modality widely used in the clinical environment for a broad range of applications. It takes advantage of different levels of freedom of the water molecules' diffusion in the biologic tissue to measure the cellularity degree for different tissues. A widespread application for DWI is in brain tumors, which present a high cellularity level (248). Intravoxel incoherent motion (IVIM) is a DWI technique developed in the late 80's to explore the moving water molecules in blood flow by using various b-values to achieve different diffusion gradient intensities (30).

Due to its capability to measure both diffusion and perfusion, IVIM has several applications for glioma patients, such as spatial localization, monitoring tumor evolution, tumor grading, and re-incidence after radiotherapy, among others. However, the use of an appropriated analysis model plays an essential role in IVIM results, and so far, there is not a consensus about that. Recently, studies have suggested to take into account different compartments (182) to model the IVIM signal. Also, in some neurological applications, the number of contributions to the total signal is unknown, since affected tissues might induce a shift on specific diffusion coefficients. Therefore, NNLS (249, 250) fitting model is a promising approach, since

it does not require any prior information about the total number of compartments (185).

This study aimed to evaluate the impact of fitting parameters through simulated data based on NNLS model and evaluate its applicability for IVIM data processing. After defining the optimal fitting parameters for the model, it was applied first in a healthy subjects group and further to a group of patients with brain glioma.

6.3 Methods

6.3.1 Simulation experiment

IVIM signals were simulated using MATLAB according to Equation 6.1, setting $D = 1\times10^{-3} mm^2/s$ and $D^* = 10\times10^{-3} mm^2/s$. The amplitudes f and f* randomly varied between 0 and 1, respecting the constraint that f + f* = 1. Two sets of b-values were used in the simulation, with 10 and 20 values, respectively, ranging from 0 to $1000 s/mm^2$ spaced logarithmically. Each of these configurations was analyzed without and with noise generated using a Gaussian distribution with standard deviation estimated from typical real data measured in a 3T MRI system.

In NNLS, signal intensity as a function of b-values is described as in Equation 6.1:

$$y(b_i) = \sum_{i=1}^{M} S(D_j) e^{-bD_i} = \sum_{i=1}^{M} A_{ij} S_J \tag{6.1}$$

where $y(b_i)$ is the simulated signal, A_{ij} is the matrix containing the exponential kernel function, and Sj is the unknown amplitude for the component with diffusion coefficient D_j. Using Tikhonov regularization to NNLS, the problem consists of finding amplitudes Sj that minimize Equation 6.2.

$$\sum_{i=1}^{N} (\sum_{j=1}^{M} A_{ij} S_j - y_i)^2 + \mu \sum_{i=1}^{N} (\sum_{j=1}^{M} H_{ij} S_J)^2 \tag{6.2}$$

in which μ is the regularization parameter calculated according to the L-curve for Tikhonov regularization (251) and H_{ij} is the identity matrix. In Equation 6.2, N is the number of b-values used in the simulation and M is the number of exponential terms with different diffusion values used in the fitting. Results are presented as a "D spectrum", where each peak corresponds to a diffusion component and its area represents the amplitude of that component. In this study, diffusion coefficients between 10^{-3} and $10^3 mm^2/s$ were analyzed and the number of exponentials used for fitting assumed the following values: 200, 400, 600, 800 and 1000. Perfusion fraction was estimated as pf = f*/(f+f*).

6.3.2 MRI experiment

Twenty healthy subjects (8 females, 31.05 ±10.30) and twenty patients (12 females, 50.35 ± 19.36) with diffuse glioma were scanned in a 3T Philips system equipped with gradients capable of 80 mT/m amplitude and 200 mT/m/ms slew rate, and a 32-channel head coil. Images were acquired using 15 different b-values and a SE-EPI sequence (TR/TE = 1500/106ms, FOV = 240x240mm, matrix = 288x288). For this study, two patients were chosen to be described. In one patient, images were acquired in three sessions, with one week of interval between each other, while the second had only one scan session.

6.3.3 Data analysis

Data analysis was performed in MATLAB (MathWorks, Natick, MA). The data preprocessing consisted of the correction for motion and effects of eddy currents using the ACID toolbox (252). The NNLS fitting model described in Equation 6.1 and 6.2 was implemented in a local script in MATLAB to extract the IVIM outputs.

6.4 Results

6.4.1 Simulation experiment

Figure 31 shows a simulated signal with 20 b-values and its respective spectral distribution of diffusion coefficients obtained from regularized NNLS fitting using 600 exponentials. In this case, values estimated for diffusion coefficients (D and D*) and perfusion fraction were exact for noiseless data and 0.80x10^{-3} mm^2/s, 10^{-3} mm^2/s, 0.64, respectively, for noisy data. Figure 32 shows the percentage difference between simulated signal parameters and fitting outputs for a different number of b-values and noisy and noiseless data. Figure 33 illustrates the importance of using the proper regularization parameter. Although fitting seems good, the use of a high regularization parameter prevented NNLS from separating the diffusion coefficients contributing to the signal properly.

6.4.2 MRI experiments

The results for the three sessions of patient 1 are shown in Figure 34. In Figure 34a we show the structural images resulted from b_0 of IVIM acquisition. Apparent diffusion coefficient (ADC) and perfusion fraction measurements were output of NNLS fitting and shown in Figure 34b and 34c, respectively. For patient 2, images were acquired for only one session. Results for structural images, ADC and perfusion fraction are in Figure 35a, 35b and 35c, respectively. Red arrows indicate tumor abnormalities.

Figure 31 – IVIM simulation fitting

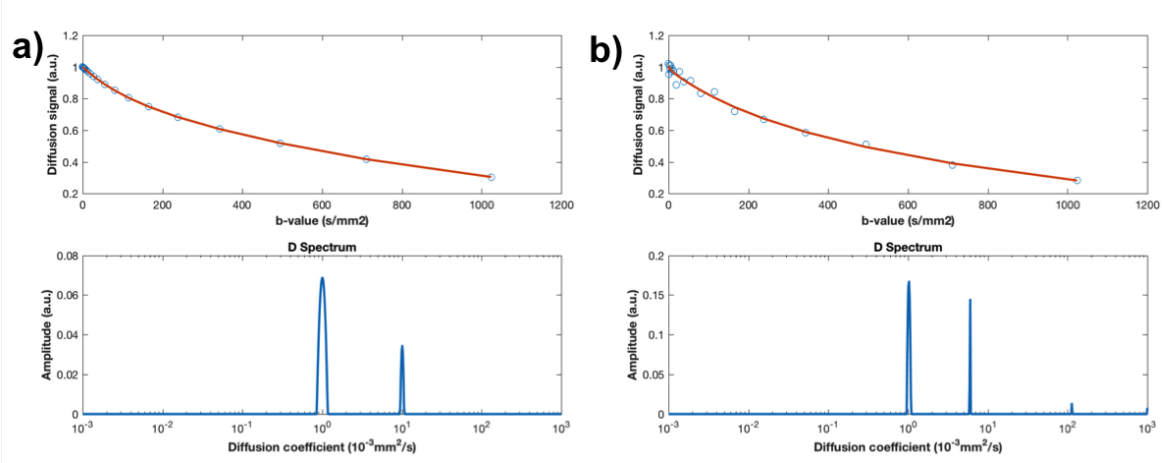

Diffusion signal simulated with 20 b-values (upper row) and its respective spectral distribution of diffusion coefficients obtained from regularized NNLS fitting using 600 exponentials (lower row). (a) Noiseless and (b) noisy data. Source: the author.

6.5 Discussion

The simulated data showed that the fitting model we used could provide the required information without any prior inputs (185). It is a relevant contribution since some neurological diseases present an unknown number of diffusion components (253), which can impair conventional evaluation using either mono or bi-exponential models. Also, this method has the potential to separate large vessels' contributions, which is expected to present a very fast-decaying component (182), undetectable by conventional fitting methods. For noiseless data, the method returns all values of interest with high precision (Figure 32 a and c). For noisy data, every diffusion component is found within its own order of magnitude (Figure 32 b and d). The precision of the fitting improves as the number of exponentials used for the fitting, increases. Thus, we recommend using at least 600 intervals in the spectrum (Figure 32). Finally, determining the regularization parameter accurately is crucial for the efficiency of the proposed method. We used the L-curve method, which revealed to be a good candidate for that (251). First, results for in vivo data showed good perspectives.

From data of patient 1, we evaluated the use of IVIM for tumor monitoring within three weeks. ADC maps had a good sensibility to detect tumor localization according to structural images in agreement to (254, 74). In regions affected by the tumor, increased ADC was observed (224, 74). It was also possible to find abnormalities in perfusion measurements by assessing perfusion fraction maps, which also showed differences among the three acquisitions. Images for patient 2 showed good accuracy in IVIM ADC to localize tumor spatially, compared to structural images. Perfusion fraction maps allowed the detection of small perfusion changes due to the glioma.

In conclusion, our preliminary study showed the efficiency of the NNLS fitting model

Figure 32 – IVIM fitting errors

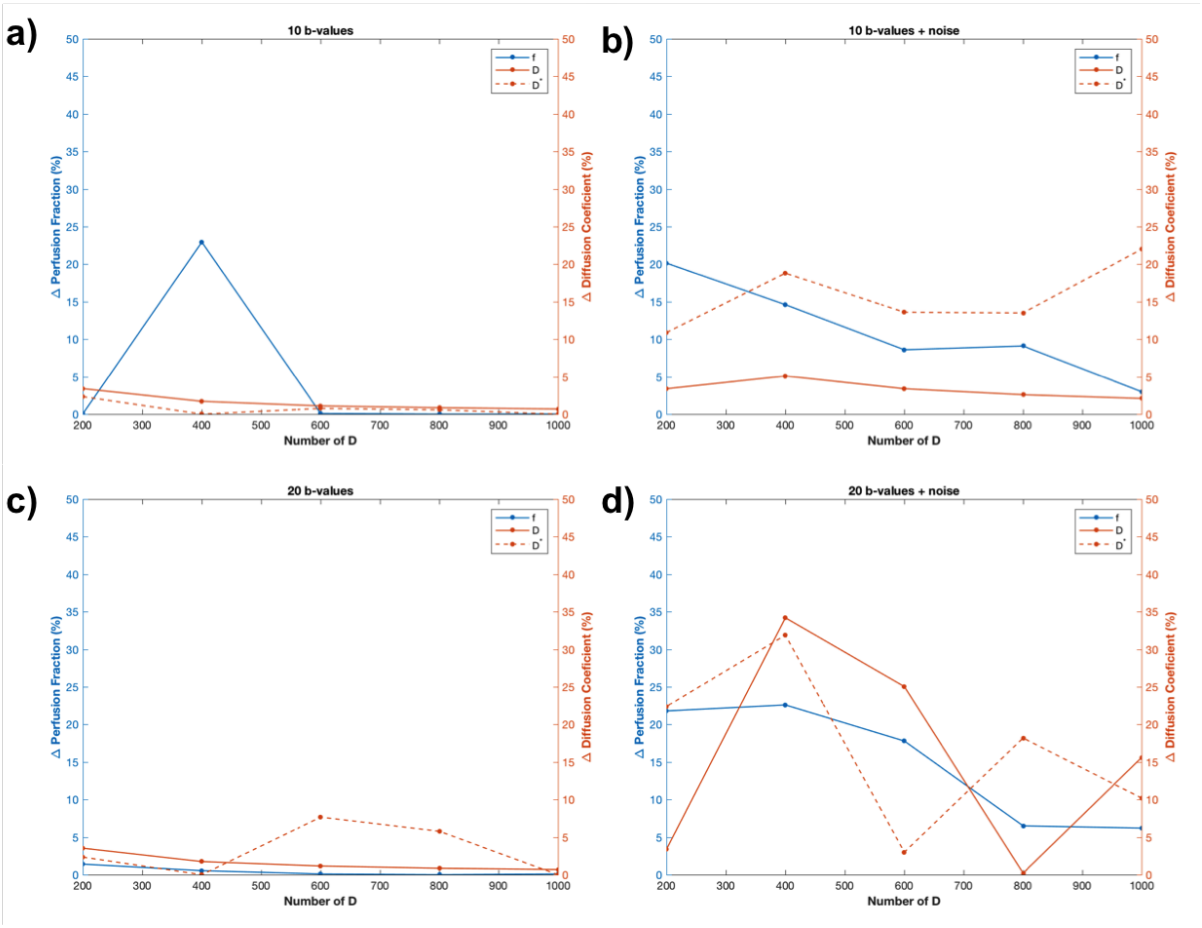

Variation between simulated and obtained values using NNLS fitting for IVIM data processing. (a) Noiseless and (b) noisy data with 10 b-values. (c) Noiseless and (d) noisy data with 20 b-values. Source: the author.

for analyzing IVIM images for the whole-brain assessment of brain glioma. The next steps include the acquisition of a higher number of patients, statistical analysis, and correlation of IVIM outputs between each other and also combining with other MRI approaches, such as ASL,DSC, and DCE for glioma grading and assessment of blood-brain barrier integrity.

Figure 33 – IVIM fitting with non-optimized parameters

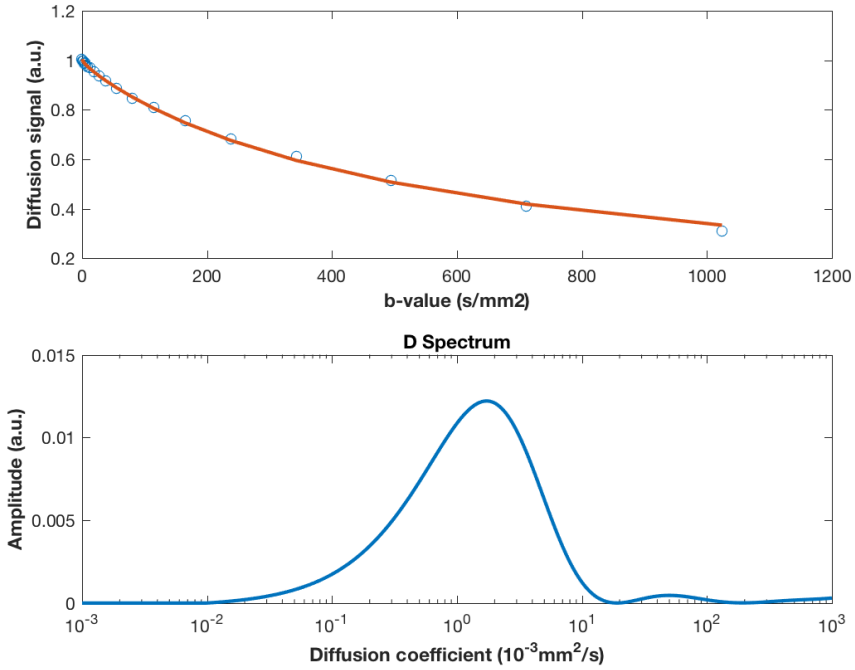

Fitting result calculated with a wrong regularization parameter. NNLS model could not separate the diffusion coefficients contributing to total signal. Source: the author.

Figure 34 – IVIM maps for tumor monitoring of patient 1

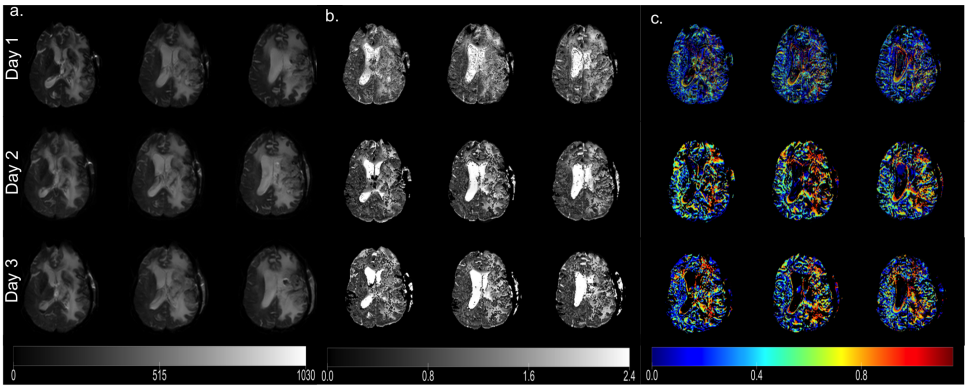

Three sessions acquired for patient 1. (a) Structural images, (b) Apparent diffusion coefficient map and (c) Perfusion fraction map. Source: the author.

Figure 35 – IVIM maps for tumor assessment of patient 2

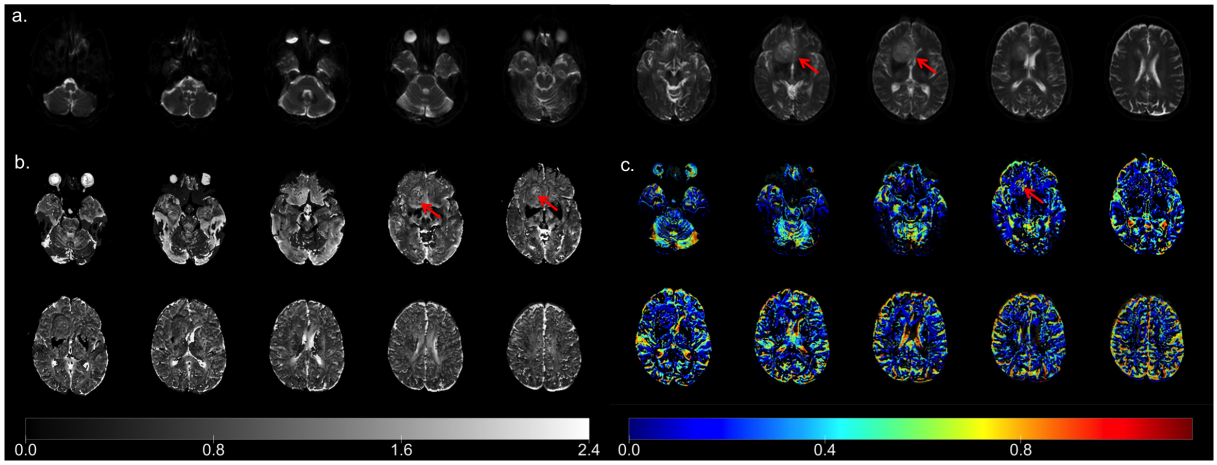

Images acquired for patient 2. (a) Structural images, (b) Apparent diffusion coefficient map and (c) Perfusion fraction map. Red arrows indicate tumor abnormalities. Source: the author.

7 General conclusion and future steps

This doctoral thesis aimed to explore imaging methods related to blood flow and brain perfusion, with possible clinical applications in several neurological diseases, in particular, cerebrovascular diseases. For early diagnosis improvement, we explored acquisition methods' optimization, as well as the combination of different techniques to assess the brain hemodynamics, and also to obtain information about the blood-brain barrier integrity. On the other hand, for the aim of patient monitoring, we focused on the use of a different approach to performing functional analysis based on the cerebral blood flow fluctuations. So, the use of functional arterial spin labeling (fASL) was explored to analyze the brain functional connectivity in the resting state condition and under the performing of motor and language tasks.

The results obtained for functional analysis using fASL showed a high potential of applicability. The first step was to optimize the imaging protocol for dual-echo ASL, to obtain accurate information of both the cerebral blood flow and the bold signal simultaneously. The protocol optimization, as well as the method validation, was performed with a task-based fMRI experiment during a robust motor task. The analysis of the results showed no statistical difference for CBF quantification between single-echo and dual-echo ASL acquisitions while providing the exploration of functional analysis by using the concurrent BOLD signal of the ASL data. After its validation in a more robust task, the next step was the novel application in a language task and its comparison to the resting-state condition. For this application, we showed statistical differences in the quantitative CBF in regions primarily related to the language processing in the brain when comparing the language task experiment to the resting state condition. Furthermore, we showed positive evidence in the addition of a physiological basis (CBF) to the brain reorganization when performing a language task as well as a more accurate localization of the site of activation in the brain when compared to the BOLD signal. All these results suggest that fASL has good potential for the study of patients with neurological conditions. The future steps for this ASL application are to perform a larger cohort as well as its application to groups of patients with neurological diseases, e.g., Alzheimer's and cerebral small vessel diseases.

The effort to contribute to the imaging tools for diagnosis consisted of exploring MRI acquisition improvements as well as the combination of information provided by different techniques, including ASL and IVIM. The final, future goal is the noninvasive measurement of the blood-brain barrier permeability. To do so, we focused on the combination of a Hadamard-encoding approach for multi-PLD pCASL with the recommended 3D GRASE readout module. The obtained results suggested the segmented GRASE and the use of flow-compensation gradients to delineate better the vascular signal during the inflow of the arterial blood crossing

the BBB and its perfusion in the brain tissue. These two pulse sequence elements play an important role in increasing the SNR in the measurement of the capillaries signal and a key point to the further measurement of BBB water exchange.

We also performed the optimization of IVIM protocol to our MRI scanner, evaluating the number of b-values as well as the maximum b-value acquired. It was performed through a simulation study followed by the in vivo acquisition. Simulations were performed to optimize the fitting parameters required in the non-negative least squares approach and to analyze the impact of acquisition parameters on this model. After the simulation experiment, we acquired data of 20 healthy subjects for the validation of the acquisition protocol and the fitting model. Finally, to evaluate the IVIM outputs to obtain evidence of damages to BBB integrity, we started a pilot experiment in patients with diffuse glioma, which is an excellent model to analyze BBB disruption. Further steps for the measurement of BBB permeability include the combination of ASL and IVIM in a single MRI pulse sequence, which is also known as diffusion-ASL, to better understanding the flow direction within the vascular side and its movement crossing the BBB. Finally, we intend to compare our results with traditional BBB measurements, e.g., using the DCE-MRI approach.

8 Scientific production

8.1 Awards

- OHBM travel awards 2019 - Organization for Human Brain Mapping

8.2 Grants received

- PDSE CAPES scholarship (Brazilian doctoral exchange program) to the Leiden University Medical Center, in Leiden, the Netherlands.

8.3 Peer-reviewed scientific papers

- SILVA, JOÃO PAULO SANTOS ; DA MATA MÔNACO, LUCIANA ; **PASCHOAL, ANDRÉ MONTEIRO** ; DE OLIVEIRA, ÍCARO AGENOR FERREIRA ; LEONI, RENATA FERRANTI . Effects of global signal regression and subtraction methods on resting-state functional connectivity using arterial spin labeling data. MAGNETIC RESONANCE IMAGING, v. X, p. X, 2018.

- **PASCHOAL, A. M.**; LEONI, R. F.; SANTOS, A. C.; PAIVA, F.F. Intravoxel incoherent motion MRI in neurological andcerebrovascular diseases.NeuroImage: Clinical, v. 20, 2018. ISSN 22131582.

- **PASCHOAL, A. M.**; PAIVA, F. F.; LEONI, R. F. Dual-Echo Arterial SpinLabeling for Brain Perfusion Quantification and Functional Analysis.Concepts inMagnetic Resonance Part A, v. 2019, p. 1–7, aug 2019. ISSN 1546-6086.

8.4 Peer-reviewed abstracts at international conferences

- **PASCHOAL, A. M.**; LEONI, R. ; FOERSTER, B. U. ; SANTOS, A. ; PONTES NETO, O. M. ; PAIVA, F. F. . Improving Arterial Spin Labeling Acquisition to Reduce the Effect of Delayed Arrival Time. In: ISMRM 25th Annual Meeting & Exhibition, 2017, Honolulu. Proceedings of the ISMRM 25th Scientific Meeting & Exhibition. Saint Louis, MO: Mira Digital Publishing, 2017. v. 1. p. 1496-1496.

- SILVA, P. H. R.; CAMARGO, A. P. A. ; **PASCHOAL, A. M.** ; PONTES NETO, O. M. ; LEONI, R. F. . The potential of MRI as a biomarker in elderly patients with asymptomatic unilateral

internal carotid artery stenosis. In: Annual meeting ISMRM (International Society for Magnetic Resonance Medicine), 2017, Honolulu, Havai, EUA. Annual meeting ISMRM, 2017, Honolulu. Proceedings of the International Society for Magnetic Resonance in Medicine., 2017. v. 25.

- SILVA, J. P. S.; **PASCHOAL, A. M.** ; LEONI, R. F. . Evaluation of aging effects on cerebral hemodynamics by MRI. In: Annual meeting ISMRM (International Society for Magnetic Resonance Medicine), 2017, Honolulu, Havai, EUA. Annual meeting ISMRM, 2017, Honolulu. Proceedings of the International Society for Magnetic Resonance in Medicine., 2017. v. 25.

- **PASCHOAL, A. M.**; PAIVA, F. F. ; LEONI, R. . Brain connectivity assessment between rest condition and verbal fluency task through Arterial Spin Labeling. In: Joint Annual Meeting ISMRM-ESMRMB 2018, 2018, Paris. Proc. Intl. Soc. Mag. Reson. Med.(2018), 2018. v. 26.

- **PASCHOAL, A. M.**; LEONI, R. ; PAIVA, F. F. . Regularized nonnegative least-square fitting for intravoxel incoherent motion data processing: a simulation study. In: Joint Annual Meeting ISMRM-ESMRMB 2018, 2018, Paris. Proc. Intl. Soc. Mag. Reson. Med.(2018), 2018. v. 26.

- **PASCHOAL, ANDRÉ M.**; SILVA, P. H. R. ; RONDINONI, C. ; ARRIGO, I. ; PAIVA, F. F. ; LEONI, R. F. ORGANIZATION OF SEMANTIC VERBAL FLUENCY BRAIN NETWORK ASSESSED BY DUAL-ECHO ARTERIAL SPIN LABELING, Annual Meeting of Organization for Human Brain Mapping 2019, Rome, Italy.

8.5 Scientific papers in preparation

- **PASCHOAL, ANDRÉ M.**; SILVA, P. H. R. ; RONDINONI, C. ; ARRIGO, I. ; PAIVA, F. F. ; LEONI, R. F. Semantic verbal fluency brain network: delineating a physiological basis for the functional hubs using dual-echo ASL and graph theory approach. (Paper submitted to journal)

- **PASCHOAL, A. M.**; Leoni, R. F.; PASTORELLO, B; vas OSCH, M. J. P. Evaluation of number of segments in 3D GRASE readout andflow compensation effects for time-encoded pCASL. (Manuscript in preparation).

Bibliography

1 ORGANIZATION, W. H. Web Page, *The top 10 causes of death*. 2017. Disponível em: <http://www.who.int/mediacentre/factsheets/fs310/en/>. Cited 2 times in pages 23 and 80.

2 MACDONALD, M. E.; FRAYNE, R. Cerebrovascular MRI: a review of state-of-the-art approaches, methods and techniques. *Nmr in Biomedicine*, v. 28, n. 7, p. 767–791, 2015. ISSN 0952-3480. Cited in page 23.

3 WARDLAW, J. M. et al. Blood-Brain Barrier Permeability and Long-Term Clinical and Imaging Outcomes in Cerebral Small Vessel Disease. *Stroke*, v. 44, n. 2, p. 525–527, 2013. ISSN 0039-2499. Cited 2 times in pages 23 and 82.

4 ZHANG, C. E. et al. Blood-brain barrier leakage is more widespread in patients with cerebral small vessel disease. *Neurology*, v. 88, n. 5, p. 426–432, 2017. ISSN 1526-632X (Electronic) 0028-3878 (Linking). Disponível em: <http://www.ncbi.nlm.nih.gov/pubmed/28031395>. Cited in page 23.

5 HAAR, H. J. van de et al. Blood-Brain Barrier Leakage in Patients with Early Alzheimer Disease. *Radiology*, v. 281, n. 2, p. 527–535, 2016. ISSN 1527-1315 (Electronic) 0033-8419 (Linking). Disponível em: <http://www.ncbi.nlm.nih.gov/pubmed/27243267>. Cited in page 23.

6 WANG, J. J. et al. When perfusion meets diffusion: in vivo measurement of water permeability in human brain. *Journal of Cerebral Blood Flow and Metabolism*, v. 27, n. 4, p. 839–849, 2007. ISSN 0271-678x. Cited 3 times in pages 23, 49, and 85.

7 LAWRENCE, K. S.; OWEN, D.; WANG, D. J. J. A two-stage approach for measuring vascular water exchange and arterial transit time by diffusion-weighted perfusion MRI. *Magnetic Resonance in Medicine*, v. 67, n. 5, p. 1275–1284, 2012. ISSN 0740-3194. Cited 6 times in pages 23, 26, 33, 69, 85, and 86.

8 HALES, P. W.; CLARK, C. A. Combined arterial spin labeling and diffusion-weighted imaging for noninvasive estimation of capillary volume fraction and permeability-surface product in the human brain. *Journal of Cerebral Blood Flow and Metabolism*, v. 33, n. 1, p. 67–75, 2013. ISSN 0271-678x. Cited 2 times in pages 23 and 85.

9 ZHANG, R.; ROSE, W. N. Photopheresis Provides Significant Long-Lasting Benefit in Nephrogenic Systemic Fibrosis. *Case Rep Dermatol Med*, v. 2017, p. 3240287, 2017. ISSN 2090-6463 (Print) 2090-6463 (Linking). Disponível em: <http://www.ncbi.nlm.nih.gov/pubmed/28695022>. Cited in page 23.

10 SCHMID, S. et al. Time-efficient determination of spin compartments by time-encoded pCASL T-2-relaxation-under-spin-tagging and its application in hemodynamic characterization of the cerebral border zones. *Neuroimage*, v. 123, p. 72–79, 2015. ISSN 1053-8119. Cited in page 23.

11 RISACHER, S. L.; SAYKIN, A. J. Neuroimaging Biomarkers of Neurodegenerative Diseases and Dementia. *Seminars in Neurology*, v. 33, n. 4, p. 386–416, 2013. ISSN 0271-8235. Cited in page 23.

12 TARTAGLIA, M. C.; ROSEN, H. J.; MILLER, B. L. Neuroimaging in Dementia. *Neurotherapeutics*, v. 8, n. 1, p. 82–92, 2011. ISSN 1933-7213. Cited in page 23.

13 GLOVER, G. H. *Overview of functional magnetic resonance imaging*. 2011. Cited in page 23.

14 LEE, M. H.; SMYSER, C. D.; SHIMONY, J. S. Resting-state fMRI: a review of methods and clinical applications. *AJNR Am J Neuroradiol*, v. 34, n. 10, p. 1866–1872, 2013. ISSN 1936-959X (Electronic) 0195-6108 (Linking). Disponível em: <http://www.ncbi.nlm.nih.gov/pubmed/22936095>. Cited in page 23.

15 PETERSON, E. C.; WANG, Z.; BRITZ, G. *Regulation of cerebral blood flow*. 2011. Cited in page 24.

16 HANAKAWA, T. Clinical Systems Neuroscience. 2015. Cited in page 24.

17 BUXTON, R. B.; FRANK, L. R. A model for the coupling between cerebral blood flow and oxygen metabolism during neural stimulation. *Journal of Cerebral Blood Flow and Metabolism*, 1997. ISSN 0271678X. Cited 2 times in pages 25 and 32.

18 CIPOLLA, M. J. *The cerebral circulation*. 2016. Cited in page 25.

19 HAAR, H. J. van de et al. *Blood-brain barrier impairment in dementia: Current and future in vivo assessments*. 2015. Cited in page 25.

20 WINTERMARK, M. et al. Comparative overview of brain perfusion imaging techniques. *Stroke*, v. 36, n. 9, p. e83–99, 2005. ISSN 1524-4628 (Electronic) 0039-2499 (Linking). Disponível em: <http://www.ncbi.nlm.nih.gov/pubmed/16100027>. Cited in page 26.

21 LUYPAERT, R. et al. Diffusion and perfusion MRI: Basic physics. *European Journal of Radiology*, 2001. ISSN 0720048X. Cited in page 26.

22 GADIAN, D. G. et al. Diffusion and perfusion magnetic resonance imaging in childhood stroke. *Journal of Child Neurology*, 2000. ISSN 08830738. Cited in page 26.

23 FERRE, J. C. et al. Arterial spin labeling (ASL) Perfusion: techniques and clinical use. *Journal De Radiologie Diagnostique Et Interventionnelle*, v. 94, n. 12, p. 1208–1221, 2013. ISSN 2211-5706. Cited 4 times in pages 26, 35, 47, and 74.

24 OSCH, M. J. van et al. *Advances in arterial spin labelling MRI methods for measuring perfusion and collateral flow*. 2018. Cited 3 times in pages 26, 31, and 71.

25 SCHMID, S. et al. Venous Velocity Selective Inversion for improved selection of the venous blood pool for oxygen extraction fraction determination. In: *Proc. Intl. Soc. Mag. Reson. Med.* Montreal, Canada: [s.n.], 2019. p. 4968. Cited 2 times in pages 26 and 69.

26 LECLERCQ, D. et al. *Diffusion tractography: Methods, validation and applications in patients with neurosurgical lesions*. 2011. Cited in page 26.

27 FARQUHARSON, S. et al. White matter fiber tractography: Why we need to move beyond DTI. *Journal of Neurosurgery*, 2013. ISSN 00223085. Cited in page 26.

28 GALLAGHER, T. A.; ALEXANDER, A. L.; FIELD, A. S. Diffusion tensor magnetic resonance imaging: Physical principles. In: *Functional Neuroradiology: Principles and Clinical Applications*. [S.l.: s.n.], 2012. ISBN 9781441903457. Cited in page 26.

29 Le Bihan, D. What can we see with IVIM MRI? *Neuroimage*, 2017. ISSN 1095-9572 (Electronic) 1053-8119 (Linking). Disponível em: <http://www.ncbi.nlm.nih.gov/pubmed/29277647>. Cited 3 times in pages 26, 76, and 79.

30 PASCHOAL, A. et al. Intravoxel incoherent motion MRI in neurological and cerebrovascular diseases. *NeuroImage: Clinical*, v. 20, 2018. ISSN 22131582. Cited 2 times in pages 26 and 87.

31 ALSOP, D. C. et al. Recommended implementation of arterial spin-labeled perfusion MRI for clinical applications: A consensus of the ISMRM perfusion study group and the European consortium for ASL in dementia. *Magn Reson Med*, v. 73, n. 1, p. 102–116, 2015. ISSN 1522-2594 (Electronic) 0740-3194 (Linking). Disponível em: <http://www.ncbi.nlm.nih.gov/pubmed/24715426>. Cited 6 times in pages 27, 28, 29, 63, 71, and 79.

32 DAI, W. et al. Continuous flow-driven inversion for arterial spin labeling using pulsed radio frequency and gradient fields. *Magn Reson Med*, v. 60, n. 6, p. 1488–1497, 2008. ISSN 1522-2594 (Electronic) 0740-3194 (Linking). Disponível em: <http://www.ncbi.nlm.nih.gov/pubmed/19025913>. Cited in page 27.

33 PETERSEN, E. T. et al. Non-invasive measurement of perfusion: a critical review of arterial spin labelling techniques. *British Journal of Radiology*, v. 79, n. 944, p. 688–701, 2006. ISSN 0007-1285. Cited in page 27.

34 TALAGALA, S. L. et al. Whole-brain 3D perfusion MRI at 3.0 T using CASL with a separate labeling coil. *Magnetic Resonance in Medicine*, v. 52, n. 1, p. 131–140, 2004. ISSN 0740-3194. Cited in page 27.

35 TRAMPEL, R. et al. Efficiency of flow-driven adiabatic spin inversion under realistic experimental conditions: a computer simulation. *Magnetic Resonance in Medicine*, v. 51, n. 6, p. 1187–1193, 2004. ISSN 0740-3194 (Print) 0740-3194 (Linking). Disponível em: <http://www.ncbi.nlm.nih.gov/pubmed/15170839>. Cited in page 27.

36 FERNANDEZ-SEARA, M. A. et al. Continuous arterial spin labeling perfusion measurements using single shot 3D GRASE at 3 T. *Magn Reson Med*, v. 54, n. 5, p. 1241–1247, 2005. ISSN 0740-3194 (Print) 0740-3194 (Linking). Disponível em: <http://www.ncbi.nlm.nih.gov/pubmed/16193469>. Cited in page 27.

37 EDELMAN, R. R. et al. Qualitative mapping of cerebral blood flow and functional localization with echo-planar MR imaging and signal targeting with alternating radio frequency. *Radiology*, v. 192, n. 2, p. 513–520, 1994. ISSN 0033-8419 (Print) 0033-8419 (Linking). Disponível em: <http://www.ncbi.nlm.nih.gov/pubmed/8029425>. Cited in page 27.

38 EDELMAN, R. R. et al. Qualitative mapping of cerebral blood flow and functional localization with echo-planar MR imaging and signal targeting with alternating radio frequency. *Radiology*, v. 192, n. 2, p. 513–520, 1994. ISSN 0033-8419 (Print) 0033-8419 (Linking). Disponível em: <http://www.ncbi.nlm.nih.gov/entrez/query.fcgi?cmd=Retrieve{&}db=PubMed{&}dopt=Citation{&}list{_}>. Cited in page 27.

39 WU, W. C. et al. A theoretical and experimental investigation of the tagging efficiency of pseudocontinuous arterial spin labeling. *Magn Reson Med*, v. 58, n. 5,

p. 1020–1027, 2007. ISSN 0740-3194 (Print) 0740-3194 (Linking). Disponível em: <http://www.ncbi.nlm.nih.gov/pubmed/17969096>. Cited in page 27.

40 DAI, W. et al. Continuous flow-driven inversion for arterial spin labeling using pulsed radio frequency and gradient fields. *Magn Reson Med*, v. 60, n. 6, p. 1488–1497, 2008. ISSN 1522-2594 (Electronic) 0740-3194 (Linking). Disponível em: <http://www.ncbi.nlm.nih.gov/entrez/query.fcgi?cmd=Retrieve{&}db=PubMed{&}dopt=Citation{&}list{_}u>. Cited in page 27.

41 QIN, Q.; ZIJL, P. C. van. Velocity-selective-inversion prepared arterial spin labeling. *Magnetic Resonance in Medicine*, 2016. ISSN 15222594. Cited 2 times in pages 28 and 69.

42 JUNG, Y.; WONG, E. C.; LIU, T. T. Multiphase pseudocontinuous arterial spin labeling (MP-PCASL) for robust quantification of cerebral blood flow. *Magnetic Resonance in Medicine*, v. 64, n. 3, p. 799–810, 2010. ISSN 1522-2594 (Electronic) 0740-3194 (Linking). Disponível em: <http://www.ncbi.nlm.nih.gov/pubmed/20578056>. Cited in page 28.

43 LOU, X. et al. Multi-delay ASL can identify leptomeningeal collateral perfusion in endovascular therapy of ischemic stroke. *Oncotarget*, v. 8, n. 2, p. 2437–2443, 2017. ISSN 1949-2553 (Electronic) 1949-2553 (Linking). Disponível em: <http://www.ncbi.nlm.nih.gov/pubmed/27974692>. Cited in page 28.

44 MALEKI, N.; DAI, W.; ALSOP, D. C. Optimization of background suppression for arterial spin labeling perfusion imaging. *Magnetic Resonance Materials in Physics, Biology and Medicine*, 2012. ISSN 09685243. Cited in page 28.

45 GARCIA, D. M.; DUHAMEL, G.; ALSOP, D. C. Efficiency of inversion pulses for background suppressed arterial spin labeling. *Magnetic Resonance in Medicine*, 2005. ISSN 07403194. Cited 2 times in pages 28 and 63.

46 DIXON, W. T. et al. Multiple inversion recovery reduces static tissue signal in angiograms. *Magnetic Resonance in Medicine*, 1991. ISSN 15222594. Cited in page 28.

47 YE, F. Q. et al. Noise reduction in 3D perfusion imaging by attenuating the static signal in arterial spin tagging (ASSIST). *Magnetic Resonance in Medicine*, 2000. ISSN 07403194. Cited 2 times in pages 28 and 63.

48 PARKER, D. L. et al. The need for phase-encoding flow compensation in high-resolution intracranial magnetic resonance angiography. *J Magn Reson Imaging*, v. 18, n. 1, p. 121–127, 2003. ISSN 1053-1807 (Print) 1053-1807 (Linking). Disponível em: <http://www.ncbi.nlm.nih.gov/pubmed/12815647>. Cited 2 times in pages 28 and 63.

49 GUNTHER, M.; OSHIO, K.; FEINBERG, D. A. Single-shot 3D imaging techniques improve arterial spin labeling perfusion measurements. *Magn Reson Med*, v. 54, n. 2, p. 491–498, 2005. ISSN 0740-3194 (Print) 0740-3194 (Linking). Disponível em: <http://www.ncbi.nlm.nih.gov/pubmed/16032686>. Cited 2 times in pages 29 and 63.

50 OSHIO, K.; FEINBERG, D. A. GRASE (Gradient-and Spin-Echo) imaging: A novel fast MRI technique. *Magnetic Resonance in Medicine*, 1991. ISSN 15222594. Cited 2 times in pages 29 and 63.

51 BERNSTEIN, M. A.; KING, K. F.; ZHOU, X. J. *Handbook of MRI pulse sequences*. Amsterdam; Boston: Academic Press, 2004. ISBN 0120928612 9780120928613. Cited 2 times in pages 29 and 30.

52 GUNTHER, M. Encoded continuous arterial spin labeling. In: *ISMRM workshop on cerebral perfusion and brain function: Novel techniques and applications*. Salvador, Bahia: [s.n.], 2007. Cited 2 times in pages 31 and 63.

53 TEEUWISSE, W. M. et al. Time-encoded pseudocontinuous arterial spin labeling: Basic properties and timing strategies for human applications. *Magnetic Resonance in Medicine*, 2014. ISSN 15222594. Cited 2 times in pages 31 and 63.

54 WELLS, J. A. et al. In vivo Hadamard encoded Continuous arterial spin labeling (H-CASL). *Magnetic Resonance in Medicine*, 2010. ISSN 07403194. Cited in page 31.

55 CHEN, J. E.; GLOVER, G. H. *Functional Magnetic Resonance Imaging Methods*. 2015. Cited in page 31.

56 LIN, A. L.; Monica Way, H. Y. Functional Magnetic Resonance Imaging. In: *Pathobiology of Human Disease: A Dynamic Encyclopedia of Disease Mechanisms*. [S.l.: s.n.], 2014. ISBN 9780123864567. Cited in page 31.

57 INGLIS, B. A checklist for fMRI acquisition methods reporting in the literature. *The Winnower*, 2015. ISSN 2373-146X. Cited in page 31.

58 DETRE, J. A.; WANG, J. J. Technical aspects and utility of fMRI using BOLD and ASL. *Clinical Neurophysiology*, v. 113, n. 5, p. 621–634, 2002. ISSN 1388-2457. Cited 4 times in pages 31, 32, 36, and 47.

59 SHEN, Q.; REN, H.; DUONG, T. Q. CBF, BOLD, CBV, and CMRO2 fMRI signal temporal dynamics at 500-msec resolution. *Journal of Magnetic Resonance Imaging*, 2008. ISSN 10531807. Cited in page 32.

60 BUXTON, R. B. et al. A general kinetic model for quantitative perfusion imaging with arterial spin labeling. *Magn Reson Med*, v. 40, n. 3, p. 383–396, 1998. ISSN 0740-3194 (Print) 0740-3194 (Linking). Disponível em: <http://www.ncbi.nlm.nih.gov/pubmed/9727941>. Cited 7 times in pages 32, 36, 37, 47, 49, 57, and 79.

61 LU, H. Z.; DONAHUE, M. J.; ZIJL, P. C. M. van. Detrimental effects of BOLD signal in arterial spin Labeling fMRI at high field strength. *Magnetic Resonance in Medicine*, v. 56, n. 3, p. 546–552, 2006. ISSN 0740-3194. Cited 3 times in pages 32, 36, and 47.

62 PIMENTEL, M. A. F. et al. Localization of the hand motor area by arterial spin labeling and blood oxygen level-dependent functional magnetic resonance imaging. *Human Brain Mapping*, v. 34, n. 1, p. 96–108, 2013. ISSN 1065-9471. Cited 3 times in pages 32, 36, and 47.

63 GALAZZO, I. B. et al. Investigation of Brain Hemodynamic Changes Induced by Active and Passive Movements: A Combined Arterial Spin Labeling-BOLD fMRI Study. *Journal of Magnetic Resonance Imaging*, v. 40, n. 4, p. 937–948, 2014. ISSN 1053-1807. Cited 3 times in pages 32, 36, and 47.

64 GALAZZO, I. B. et al. Patient-Specific Detection of Cerebral Blood Flow Alterations as Assessed by Arterial Spin Labeling in Drug-Resistant Epileptic Patients. *Plos One*, v. 10, n. 5, 2015. ISSN 1932-6203. Cited 3 times in pages 32, 36, and 47.

65 TANNER, J. E.; STEJSKAL, E. O. Restricted Self-Diffusion of Protons in Colloidal Systems by Pulsed-Gradient Spin-Echo Method. *Journal of Chemical Physics*, v. 49, n. 4, p. 1768–+, 1968. ISSN 0021-9606. Cited 2 times in pages 32 and 74.

66 CARR, H. Y.; PURCELL, E. M. Effects of Diffusion on Free Precession in Nuclear Magnetic Resonance Experiments. *Physical Review*, v. 94, n. 3, p. 630–638, 1954. ISSN 0031-899x. Cited 2 times in pages 32 and 75.

67 HAHN, E. L. Spin Echoes. *Physical Review*, v. 77, n. 5, p. 746, 1950. ISSN 0031-899x. Cited 2 times in pages 32 and 75.

68 SCHAEFER, P. W.; GRANT, P. E.; GONZALEZ, R. G. Diffusion-weighted MR Imaging of the Brain. *Radiology*, v. 217, n. 2, p. 331–345, nov 2000. ISSN 0033-8419. Disponível em: <http://pubs.rsna.org/doi/10.1148/radiology.217.2.r00nv24331>. Cited in page 32.

69 MORITANI, T.; EKHOLM, S.; WESTESSON, P. L. *Diffusion-weighted MR imaging of the brain*. [S.l.: s.n.], 2005. ISSN 02210363. ISBN 3540253599. Cited in page 32.

70 MUKHERJEE, P. et al. *Diffusion tensor MR imaging and fiber tractography: Theoretic underpinnings*. 2008. Cited in page 32.

71 TOURNIER, J. D.; MORI, S.; LEEMANS, A. *Diffusion tensor imaging and beyond*. 2011. Cited in page 32.

72 Le Bihan, D. et al. MR imaging of intravoxel incoherent motions: application to diffusion and perfusion in neurologic disorders. *Radiology*, v. 161, n. 2, p. 401–407, 1986. ISSN 0033-8419 (Print) 0033-8419 (Linking). Disponível em: <http://www.ncbi.nlm.nih.gov/pubmed/3763909>. Cited 4 times in pages 32, 73, 74, and 75.

73 Le Bihan, D. et al. Separation of diffusion and perfusion in intravoxel incoherent motion MR imaging. *Radiology*, v. 168, n. 2, p. 497–505, 1988. ISSN 0033-8419 (Print) 0033-8419 (Linking). Disponível em: <http://www.ncbi.nlm.nih.gov/pubmed/3393671>. Cited 2 times in pages 32 and 74.

74 BISDAS, S. et al. Intravoxel incoherent motion diffusion-weighted MR imaging of gliomas: feasibility of the method and initial results. *Neuroradiology*, v. 55, n. 10, p. 1189–1196, 2013. ISSN 0028-3940. Cited 3 times in pages 33, 83, and 90.

75 DETRE, J. A. et al. Perfusion imaging. *Magn Reson Med*, v. 23, n. 1, p. 37–45, 1992. ISSN 0740-3194 (Print) 0740-3194 (Linking). Disponível em: <http://www.ncbi.nlm.nih.gov/pubmed/1734182>. Cited 4 times in pages 35, 47, 74, and 84.

76 WONG, E. C.; BUXTON, R. B.; FRANK, L. R. Quantitative perfusion imaging using arterial spin labeling. *Neuroimaging Clin N Am*, v. 9, n. 2, p. 333–342, 1999. ISSN 1052-5149 (Print) 1052-5149 (Linking). Disponível em: <http://www.ncbi.nlm.nih.gov/entrez/query.fcgi?cmd=Retrieve{&}db=PubMed{&}dopt=Citation{&}list{_}u>. Cited in page 35.

77 TALAGALA, S. L.; NOLL, D. C. Functional MRI using steady-state arterial water labeling. *Magnetic Resonance in Medicine*, v. 39, n. 2, p. 179–183, 1998. ISSN 0740-3194. Cited 2 times in pages 36 and 47.

78 AGUIRRE, G. K. et al. Experimental design and the relative sensitivity of BOLD and perfusion fMRI. *Neuroimage*, v. 15, n. 3, p. 488–500, 2002. ISSN 1053-8119. Cited 3 times in pages 36, 46, and 47.

79 WONG, E. C.; BUXTON, R. B.; FRANK, L. R. Implementation of quantitative perfusion imaging techniques for functional brain mapping using pulsed arterial spin labeling. *NMR Biomed*, v. 10, n. 4-5, p. 237–249, 1997. ISSN 0952-3480 (Print) 0952-3480 (Linking). Disponível em: <http://www.ncbi.nlm.nih.gov/pubmed/9430354>. Cited 3 times in pages 36, 47, and 57.

80 BUXTON, R. B. Quantifying CBF with arterial spin labeling. *J Magn Reson Imaging*, v. 22, n. 6, p. 723–726, 2005. ISSN 1053-1807 (Print) 1053-1807 (Linking). Disponível em: <http://www.ncbi.nlm.nih.gov/pubmed/16261574>. Cited 4 times in pages 36, 47, 57, and 79.

81 LUH, W. M. et al. Comparison of simultaneously measured perfusion and BOLD signal increases during brain activation with T-1-based tissue identification. *Magnetic Resonance in Medicine*, v. 44, n. 1, p. 137–143, 2000. ISSN 0740-3194. Cited in page 36.

82 TAK, S. et al. Dynamic and static contributions of the cerebrovasculature to the resting-state BOLD signal. *Neuroimage*, v. 84, p. 672–680, 2014. ISSN 1095-9572 (Electronic) 1053-8119 (Linking). Disponível em: <http://www.ncbi.nlm.nih.gov/pubmed/24099842>. Cited 2 times in pages 36 and 47.

83 WOOLRICH, M. W. et al. Bayesian inference of hemodynamic changes in functional arterial spin labeling data. *Magnetic Resonance in Medicine*, v. 56, n. 4, p. 891–906, 2006. ISSN 0740-3194. Cited 2 times in pages 36 and 47.

84 GHARIQ, E. et al. Effects of background suppression on the sensitivity of dual-echo arterial spin labeling MRI for BOLD and CBF signal changes. *Neuroimage*, v. 103, p. 316–322, 2014. ISSN 1053-8119. Cited in page 36.

85 STORTI, S. F. et al. Dual-echo ASL contributes to decrypting the link between functional connectivity and cerebral blow flow. *Hum Brain Mapp*, v. 38, n. 12, p. 5831–5844, 2017. ISSN 1097-0193 (Electronic) 1065-9471 (Linking). Disponível em: <http://www.ncbi.nlm.nih.gov/pubmed/28885752>. Cited 3 times in pages 36, 47, and 57.

86 STORTI, S. F. et al. Dual-echo ASL based assessment of motor networks: a feasibility study. *J Neural Eng*, v. 15, n. 2, p. 26018, 2018. ISSN 1741-2552 (Electronic) 1741-2552 (Linking). Disponível em: <http://www.ncbi.nlm.nih.gov/pubmed/28884708>. Cited 4 times in pages 36, 47, 49, and 57.

87 COHEN, A. D.; NENCKA, A. S.; WANG, Y. Multiband multi-echo simultaneous ASL/BOLD for task-induced functional MRI. *PLoS One*, v. 13, n. 2, p. e0190427, 2018. ISSN 1932-6203 (Electronic) 1932-6203 (Linking). Disponível em: <http://www.ncbi.nlm.nih.gov/pubmed/29389985>. Cited in page 36.

88 WANG, Z. et al. Empirical optimization of ASL data analysis using an ASL data processing toolbox: ASLtbx. *Magnetic Resonance Imaging*, v. 26, n. 2, p. 261–269, 2008. ISSN 0730-725x. Cited 2 times in pages 37 and 57.

89 SILVA, J. et al. Effects of global signal regression and subtraction methods on resting-state functional connectivity using arterial spin labeling data. *Magnetic Resonance Imaging*, v. 51, 2018. ISSN 18735894. Cited 2 times in pages 37 and 49.

90 OLIVEIRA, I. A. F. et al. Brain functional and perfusional alterations in schizophrenia: an arterial spin labeling study. *Psychiatry Res*, v. 272, p. 71–78, 2018. ISSN 1872-7123 (Electronic)

0165-1781 (Linking). Disponível em: <http://www.ncbi.nlm.nih.gov/pubmed/29229240>. Cited 3 times in pages 37, 49, and 57.

91 JENKINSON, M. et al. Improved optimization for the robust and accurate linear registration and motion correction of brain images. *Neuroimage*, v. 17, n. 2, p. 825–841, 2002. ISSN 1053-8119. Cited in page 38.

92 JANN, K. et al. Functional connectivity in BOLD and CBF data: similarity and reliability of resting brain networks. *Neuroimage*, v. 106, p. 111–122, 2015. ISSN 1095-9572 (Electronic) 1053-8119 (Linking). Disponível em: <http://www.ncbi.nlm.nih.gov/pubmed/25463468>. Cited in page 38.

93 WHITFIELD-GABRIELI, S.; NIETO-CASTANON, A. Conn: a functional connectivity toolbox for correlated and anticorrelated brain networks. *Brain Connect*, v. 2, n. 3, p. 125–141, 2012. ISSN 2158-0022 (Electronic) 2158-0014 (Linking). Disponível em: <http://www.ncbi.nlm.nih.gov/pubmed/22642651>. Cited 4 times in pages 38, 50, 51, and 57.

94 R Development Core, T. Computational Many-Particle Physics. 2008. Cited in page 38.

95 LIU, J. H.; VENOT, A. Design of a computerized system for the retrospective analysis by the physician of his own drug prescriptions. *Stud Health Technol Inform*, v. 84, n. Pt 2, p. 1175–1179, 2001. ISSN 0926-9630 (Print) 0926-9630 (Linking). Disponível em: <http://www.ncbi.nlm.nih.gov/pubmed/11604915>. Cited in page 42.

96 YONGBI, M. N. et al. Simultaneous BOLD/perfusion measurement using dual-echo FAIR and UNFAIR: sequence comparison at 1.5T and 3.0T. *Magn Reson Imaging*, v. 19, n. 9, p. 1159–1165, 2001. ISSN 0730-725X (Print) 0730-725X (Linking). Disponível em: <http://www.ncbi.nlm.nih.gov/pubmed/11755725>. Cited in page 42.

97 LIU, T. T.; WONG, E. C. A signal processing model for arterial spin labeling functional MRI. *Neuroimage*, v. 24, n. 1, p. 207–215, 2005. ISSN 1053-8119 (Print) 1053-8119 (Linking). Disponível em: <http://www.ncbi.nlm.nih.gov/pubmed/15588612>. Cited 2 times in pages 42 and 59.

98 LEZAK, M. D.; LORING, D. W.; HOWIESON, D. B. Book. *Neuropsychological assessment*. Oxford: Oxford Univ. Press, 2004. ISBN 9780195111217 0195111214. Cited in page 45.

99 MASCALI, D. et al. Disruption of Semantic Network in Mild Alzheimer's Disease Revealed by Resting-State fMRI. *Neuroscience*, v. 371, p. 38–48, 2018. ISSN 1873-7544 (Electronic) 0306-4522 (Linking). Disponível em: <http://www.ncbi.nlm.nih.gov/pubmed/29197559>. Cited in page 45.

100 WAGNER, S. et al. A coordinate-based ALE functional MRI meta-analysis of brain activation during verbal fluency tasks in healthy control subjects. *BMC Neurosci*, v. 15, p. 19, 2014. ISSN 1471-2202 (Electronic) 1471-2202 (Linking). Disponível em: <http://www.ncbi.nlm.nih.gov/pubmed/24456150>. Cited 3 times in pages 45, 46, and 50.

101 ZHAO, Q.; GUO, Q.; HONG, Z. Clustering and switching during a semantic verbal fluency test contribute to differential diagnosis of cognitive impairment. *Neurosci Bull*, v. 29, n. 1, p. 75–82, 2013. ISSN 1995-8218 (Electronic) 1995-8218 (Linking). Disponível em: <http://www.ncbi.nlm.nih.gov/pubmed/23322003>. Cited in page 46.

102 PETTIT, L. et al. Heterogeneity of letter fluency impairment and executive dysfunction in Parkinson's disease. *J Int Neuropsychol Soc*, v. 19, n. 9, p. 986–994, 2013. ISSN 1469-7661 (Electronic) 1355-6177 (Linking). Disponível em: <http://www.ncbi.nlm.nih.gov/pubmed/23953916>. Cited in page 46.

103 ANDREOU, G.; TROTT, K. Verbal fluency in adults diagnosed with attention-deficit hyperactivity disorder (ADHD) in childhood. *Atten Defic Hyperact Disord*, v. 5, n. 4, p. 343–351, 2013. ISSN 1866-6647 (Electronic) 1866-6116 (Linking). Disponível em: <http://www.ncbi.nlm.nih.gov/pubmed/23749309>. Cited in page 46.

104 METTERNICH, B. et al. Verbal fluency in focal epilepsy: a systematic review and meta-analysis. *Neuropsychol Rev*, v. 24, n. 2, p. 200–218, 2014. ISSN 1573-6660 (Electronic) 1040-7308 (Linking). Disponível em: <http://www.ncbi.nlm.nih.gov/pubmed/24667998>. Cited in page 46.

105 TYBURSKI, E. et al. Neuropsychological characteristics of verbal and non-verbal fluency in schizophrenia patients. *Arch Psychiatr Nurs*, v. 29, n. 1, p. 33–38, 2015. ISSN 1532-8228 (Electronic) 0883-9417 (Linking). Disponível em: <http://www.ncbi.nlm.nih.gov/pubmed/25634872>. Cited in page 46.

106 PISKUNOWICZ, M. et al. [Verbal fluency tests–application in neuropsychological assessment]. *Psychiatr Pol*, v. 47, n. 3, p. 475–485, 2013. ISSN 0033-2674 (Print) 0033-2674 (Linking). Disponível em: <http://www.ncbi.nlm.nih.gov/pubmed/23885541>. Cited 2 times in pages 46 and 59.

107 GLIKMANN-JOHNSTON, Y. et al. Distinct functional connectivity of the hippocampus during semantic and phonemic fluency. *Neuropsychologia*, v. 69, p. 39–49, 2015. ISSN 1873-3514 (Electronic) 0028-3932 (Linking). Disponível em: <http://www.ncbi.nlm.nih.gov/pubmed/25619848>. Cited in page 46.

108 PRICE, C. J. The anatomy of language: a review of 100 fMRI studies published in 2009. *Ann N Y Acad Sci*, v. 1191, p. 62–88, 2010. ISSN 1749-6632 (Electronic) 0077-8923 (Linking). Disponível em: <http://www.ncbi.nlm.nih.gov/pubmed/20392276>. Cited in page 46.

109 BALDO, J. V. et al. Role of frontal versus temporal cortex in verbal fluency as revealed by voxel-based lesion symptom mapping. *J Int Neuropsychol Soc*, v. 12, n. 6, p. 896–900, 2006. ISSN 1355-6177 (Print) 1355-6177 (Linking). Disponível em: <http://www.ncbi.nlm.nih.gov/pubmed/17064451>. Cited in page 46.

110 GHANAVATI, E. et al. Differential role of prefrontal, temporal and parietal cortices in verbal and figural fluency: Implications for the supramodal contribution of executive functions. *Sci Rep*, v. 9, n. 1, p. 3700, 2019. ISSN 2045-2322 (Electronic) 2045-2322 (Linking). Disponível em: <http://www.ncbi.nlm.nih.gov/pubmed/30842493>. Cited in page 46.

111 SAUR, D. et al. Ventral and dorsal pathways for language. *Proc Natl Acad Sci U S A*, v. 105, n. 46, p. 18035–18040, 2008. ISSN 1091-6490 (Electronic) 0027-8424 (Linking). Disponível em: <http://www.ncbi.nlm.nih.gov/pubmed/19004769>. Cited in page 46.

112 WAWRZYNIAK, M. et al. Fronto-temporal interactions are functionally relevant for semantic control in language processing. *PLoS One*, v. 12, n. 5, p. e0177753, 2017. ISSN 1932-6203 (Electronic) 1932-6203 (Linking). Disponível em: <http://www.ncbi.nlm.nih.gov/pubmed/28505211>. Cited in page 46.

113 TRAUTWEIN, J.; SCHROEDER, S. Orthographic Networks in the Developing Mental Lexicon. Insights From Graph Theory and Implications for the Study of Language Processing. *Front Psychol*, v. 9, p. 2252, 2018. ISSN 1664-1078 (Print) 1664-1078 (Linking). Disponível em: <http://www.ncbi.nlm.nih.gov/pubmed/30524342>. Cited in page 46.

114 VISSER, M.; JEFFERIES, E.; Lambon Ralph, M. A. Semantic processing in the anterior temporal lobes: a meta-analysis of the functional neuroimaging literature. *J Cogn Neurosci*, v. 22, n. 6, p. 1083–1094, 2010. ISSN 1530-8898 (Electronic) 0898-929X (Linking). Disponível em: <http://www.ncbi.nlm.nih.gov/pubmed/19583477>. Cited 2 times in pages 46 and 58.

115 ELMER, S. Broca Pars Triangularis Constitutes a "Hub" of the Language-Control Network during Simultaneous Language Translation. *Front Hum Neurosci*, v. 10, p. 491, 2016. ISSN 1662-5161 (Print) 1662-5161 (Linking). Disponível em: <http://www.ncbi.nlm.nih.gov/pubmed/27746729>. Cited in page 46.

116 BERTOLA, L. et al. Graph analysis of verbal fluency test discriminate between patients with Alzheimer's disease, mild cognitive impairment and normal elderly controls. *Front Aging Neurosci*, v. 6, p. 185, 2014. ISSN 1663-4365 (Print) 1663-4365 (Linking). Disponível em: <http://www.ncbi.nlm.nih.gov/pubmed/25120480>. Cited in page 46.

117 LI, Q. et al. Functional Translocation of Broca's Area in a Low-Grade Left Frontal Glioma: Graph Theory Reveals the Novel, Adaptive Network Connectivity. *Front Neurol*, v. 10, p. 702, 2019. ISSN 1664-2295 (Print) 1664-2295 (Linking). Disponível em: <http://www.ncbi.nlm.nih.gov/pubmed/31333562>. Cited in page 46.

118 LIANG, X. et al. Coupling of functional connectivity and regional cerebral blood flow reveals a physiological basis for network hubs of the human brain. *Proc Natl Acad Sci U S A*, v. 110, n. 5, p. 1929–1934, 2013. ISSN 1091-6490 (Electronic) 0027-8424 (Linking). Disponível em: <http://www.ncbi.nlm.nih.gov/pubmed/23319644>. Cited in page 46.

119 DETRE, J. A. et al. Tissue specific perfusion imaging using arterial spin labeling. *NMR Biomed*, v. 7, n. 1-2, p. 75–82, 1994. ISSN 0952-3480 (Print) 0952-3480 (Linking). Disponível em: <http://www.ncbi.nlm.nih.gov/pubmed/8068529>. Cited in page 47.

120 PETCHARUNPAISAN, S.; RAMALHO, J.; CASTILLO, M. Arterial spin labeling in neuroimaging. *World J Radiol*, v. 2, n. 10, p. 384–398, 2010. ISSN 1949-8470 (Electronic) 1949-8470 (Linking). Disponível em: <http://www.ncbi.nlm.nih.gov/pubmed/21161024>. Cited in page 47.

121 COHEN, A. D.; NENCKA, A. S.; WANG, Y. Multiband multi-echo simultaneous ASL/BOLD for task-induced functional MRI. *PLoS One*, v. 13, n. 2, p. e0190427, 2018. ISSN 1932-6203 (Electronic) 1932-6203 (Linking). Disponível em: <http://www.ncbi.nlm.nih.gov/pubmed/29389985>. Cited in page 47.

122 O'BRIEN, C. P. The CAGE questionnaire for detection of alcoholism: a remarkably useful but simple tool. *JAMA*, v. 300, n. 17, p. 2054–2056, 2008. ISSN 1538-3598 (Electronic) 0098-7484 (Linking). Disponível em: <http://www.ncbi.nlm.nih.gov/pubmed/18984895>. Cited 2 times in pages 48 and 60.

123 FOLSTEIN, M. F. Book. *Mini-mental state examination MMSE-2 ; user's manual*. [S.l.: s.n.], 2010. Cited 2 times in pages 48 and 60.

124 LI, Y. T. et al. Liver intravoxel incoherent motion (IVIM) magnetic resonance imaging: a comprehensive review of published data on normal values and applications for fibrosis and tumor evaluation. *Quant Imaging Med Surg*, v. 7, n. 1, p. 59–78, 2017. ISSN 2223-4292 (Print) 2223-4306 (Linking). Disponível em: <http://www.ncbi.nlm.nih.gov/pubmed/28275560>. Cited 2 times in pages 48 and 74.

125 PEIRCE, J. W. PsychoPy–Psychophysics software in Python. *J Neurosci Methods*, v. 162, n. 1-2, p. 8–13, 2007. ISSN 0165-0270 (Print) 0165-0270 (Linking). Disponível em: <http://www.ncbi.nlm.nih.gov/pubmed/17254636>. Cited in page 48.

126 WANG, Z. Improving cerebral blood flow quantification for arterial spin labeled perfusion MRI by removing residual motion artifacts and global signal fluctuations. *Magn Reson Imaging*, v. 30, n. 10, p. 1409–1415, 2012. ISSN 1873-5894 (Electronic) 0730-725X (Linking). Disponível em: <http://www.ncbi.nlm.nih.gov/pubmed/22789842>. Cited 2 times in pages 49 and 57.

127 BEHZADI, Y. et al. A component based noise correction method (CompCor) for BOLD and perfusion based fMRI. *Neuroimage*, v. 37, n. 1, p. 90–101, 2007. ISSN 1053-8119 (Print) 1053-8119 (Linking). Disponível em: <http://www.ncbi.nlm.nih.gov/pubmed/17560126>. Cited 2 times in pages 49 and 57.

128 BZDOK, D. et al. Subspecialization in the human posterior medial cortex. *Neuroimage*, v. 106, p. 55–71, 2015. ISSN 1095-9572 (Electronic) 1053-8119 (Linking). Disponível em: <http://www.ncbi.nlm.nih.gov/pubmed/25462801>. Cited 2 times in pages 50 and 60.

129 ESPOSITO, F. et al. Spatial independent component analysis of functional MRI time-series: to what extent do results depend on the algorithm used? *Hum Brain Mapp*, v. 16, n. 3, p. 146–157, 2002. ISSN 1065-9471 (Print) 1065-9471 (Linking). Disponível em: <http://www.ncbi.nlm.nih.gov/pubmed/12112768>. Cited in page 50.

130 De Martino, F. et al. Classification of fMRI independent components using IC-fingerprints and support vector machine classifiers. *Neuroimage*, v. 34, n. 1, p. 177–194, 2007. ISSN 1053-8119 (Print) 1053-8119 (Linking). Disponível em: <http://www.ncbi.nlm.nih.gov/pubmed/17070708>. Cited in page 50.

131 MUELLER, P. A.; OPPENHEIMER, D. M. The pen is mightier than the keyboard: advantages of longhand over laptop note taking. *Psychol Sci*, v. 25, n. 6, p. 1159–1168, 2014. ISSN 1467-9280 (Electronic) 0956-7976 (Linking). Disponível em: <http://www.ncbi.nlm.nih.gov/pubmed/24760141>. Cited 3 times in pages 51, 58, and 60.

132 BASSETT, D. S.; BULLMORE, E. Small-world brain networks. *Neuroscientist*, v. 12, n. 6, p. 512–523, 2006. ISSN 1073-8584 (Print) 1073-8584 (Linking). Disponível em: <http://www.ncbi.nlm.nih.gov/pubmed/17079517>. Cited in page 51.

133 MULLER, A. M.; MEYER, M. Language in the brain at rest: new insights from resting state data and graph theoretical analysis. *Front Hum Neurosci*, v. 8, p. 228, 2014. ISSN 1662-5161 (Print) 1662-5161 (Linking). Disponível em: <http://www.ncbi.nlm.nih.gov/pubmed/24808843>. Cited 2 times in pages 51 and 60.

134 ALAERTS, K. et al. Functional Organization of the Action Observation Network in Autism: A Graph Theory Approach. *PLoS One*, v. 10, n. 8, p. e0137020, 2015. ISSN 1932-6203 (Electronic) 1932-6203 (Linking). Disponível em: <http://www.ncbi.nlm.nih.gov/pubmed/26317222>. Cited 2 times in pages 51 and 60.

135 SPORNS, O. The non-random brain: efficiency, economy, and complex dynamics. *Front Comput Neurosci*, v. 5, p. 5, 2011. ISSN 1662-5188 (Electronic) 1662-5188 (Linking). Disponível em: <http://www.ncbi.nlm.nih.gov/pubmed/21369354>. Cited in page 51.

136 RUBINOV, M.; SPORNS, O. Complex network measures of brain connectivity: uses and interpretations. *Neuroimage*, v. 52, n. 3, p. 1059–1069, 2010. ISSN 1095-9572 (Electronic) 1053-8119 (Linking). Disponível em: <http://www.ncbi.nlm.nih.gov/pubmed/19819337>. Cited in page 51.

137 LATORA, V.; MARCHIORI, M. Efficient behavior of small-world networks. *Phys Rev Lett*, v. 87, n. 19, p. 198701, 2001. ISSN 0031-9007 (Print) 0031-9007 (Linking). Disponível em: <http://www.ncbi.nlm.nih.gov/pubmed/11690461>. Cited in page 51.

138 WANG, J.; ZUO, X.; HE, Y. Graph-based network analysis of resting-state functional MRI. *Front Syst Neurosci*, v. 4, p. 16, 2010. ISSN 1662-5137 (Electronic) 1662-5137 (Linking). Disponível em: <http://www.ncbi.nlm.nih.gov/pubmed/20589099>. Cited in page 51.

139 WARBURTON, E. et al. Noun and verb retrieval by normal subjects. Studies with PET. *Brain*, v. 119 (Pt 1, p. 159–179, 1996. ISSN 0006-8950 (Print) 0006-8950 (Linking). Disponível em: <http://www.ncbi.nlm.nih.gov/pubmed/8624678>. Cited in page 57.

140 SHUSTER, L. I.; LEMIEUX, S. K. An fMRI investigation of covertly and overtly produced mono- and multisyllabic words. *Brain Lang*, v. 93, n. 1, p. 20–31, 2005. ISSN 0093-934X (Print) 0093-934X (Linking). Disponível em: <http://www.ncbi.nlm.nih.gov/pubmed/15766765>. Cited in page 57.

141 CUTTING, L. E. et al. Differential components of sentence comprehension: beyond single word reading and memory. *Neuroimage*, v. 29, n. 2, p. 429–438, 2006. ISSN 1053-8119 (Print) 1053-8119 (Linking). Disponível em: <http://www.ncbi.nlm.nih.gov/pubmed/16253527>. Cited in page 57.

142 DIETZ, N. A. et al. Phonological decoding involves left posterior fusiform gyrus. *Hum Brain Mapp*, v. 26, n. 2, p. 81–93, 2005. ISSN 1065-9471 (Print) 1065-9471 (Linking). Disponível em: <http://www.ncbi.nlm.nih.gov/pubmed/15934062>. Cited in page 57.

143 PAPATHANASSIOU, D. et al. A common language network for comprehension and production: a contribution to the definition of language epicenters with PET. *Neuroimage*, v. 11, n. 4, p. 347–357, 2000. ISSN 1053-8119 (Print) 1053-8119 (Linking). Disponível em: <http://www.ncbi.nlm.nih.gov/pubmed/10725191>. Cited in page 58.

144 OLMAN, C. A.; DAVACHI, L.; INATI, S. Distortion and signal loss in medial temporal lobe. *PLoS One*, v. 4, n. 12, p. e8160, 2009. ISSN 1932-6203 (Electronic) 1932-6203 (Linking). Disponível em: <http://www.ncbi.nlm.nih.gov/pubmed/19997633>. Cited in page 58.

145 ISCHEBECK, A. et al. Reading in a regular orthography: an FMRI study investigating the role of visual familiarity. *J Cogn Neurosci*, v. 16, n. 5, p. 727–741, 2004. ISSN 0898-929X (Print) 0898-929X (Linking). Disponível em: <http://www.ncbi.nlm.nih.gov/pubmed/15200701>. Cited in page 58.

146 KIM, J. et al. Anterior cingulate cortex inactivation impairs rodent visual selective attention and prospective memory. *Behav Neurosci*, v. 130, n. 1, p. 75–90, 2016. ISSN 1939-0084 (Electronic) 0735-7044 (Linking). Disponível em: <http://www.ncbi.nlm.nih.gov/pubmed/26692448>. Cited in page 59.

147 PASCHOAL, A. M.; PAIVA, F. F.; LEONI, R. F. Dual-Echo Arterial Spin Labeling for Brain Perfusion Quantification and Functional Analysis. *Concepts in Magnetic Resonance Part A*, v. 2019, p. 1–7, aug 2019. ISSN 1546-6086. Disponível em: <https://www.hindawi.com/journals/cmra/2019/5040465/>. Cited in page 59.

148 TOULMIN, H. et al. Specialization and integration of functional thalamocortical connectivity in the human infant. *Proc Natl Acad Sci U S A*, v. 112, n. 20, p. 6485–6490, 2015. ISSN 1091-6490 (Electronic) 0027-8424 (Linking). Disponível em: <http://www.ncbi.nlm.nih.gov/pubmed/25941391>. Cited in page 59.

149 De Pisapia, N.; SLOMSKI, J. A.; BRAVER, T. S. Functional specializations in lateral prefrontal cortex associated with the integration and segregation of information in working memory. *Cereb Cortex*, v. 17, n. 5, p. 993–1006, 2007. ISSN 1047-3211 (Print) 1047-3211 (Linking). Disponível em: <http://www.ncbi.nlm.nih.gov/pubmed/16769743>. Cited in page 59.

150 Friston K; Büchel, C. Book. *Statistical parametric mapping the analysis of functional brain images*. Amsterdam; Boston; Heidelberg: Elsevier, 2007. ISBN 0123725607 9780123725608. Cited in page 59.

151 BINDER, J. R. The Wernicke area: Modern evidence and a reinterpretation. *Neurology*, v. 85, n. 24, p. 2170–2175, 2015. ISSN 1526-632X (Electronic) 0028-3878 (Linking). Disponível em: <http://www.ncbi.nlm.nih.gov/pubmed/26567270>. Cited in page 59.

152 COSTAFREDA, S. G. et al. A systematic review and quantitative appraisal of fMRI studies of verbal fluency: role of the left inferior frontal gyrus. *Hum Brain Mapp*, v. 27, n. 10, p. 799–810, 2006. ISSN 1065-9471 (Print) 1065-9471 (Linking). Disponível em: <http://www.ncbi.nlm.nih.gov/pubmed/16511886>. Cited in page 59.

153 WELLS, J. A. et al. In vivo Hadamard encoded continuous arterial spin labeling (H-CASL). *Magn Reson Med*, v. 63, n. 4, p. 1111–1118, 2010. ISSN 1522-2594 (Electronic) 0740-3194 (Linking). Disponível em: <http://www.ncbi.nlm.nih.gov/pubmed/20373414>. Cited in page 63.

154 DAI, W.; SHANKARANARAYANAN, A.; ALSOP, D. C. Volumetric measurement of perfusion and arterial transit delay using hadamard encoded continuous arterial spin labeling. *Magnetic Resonance in Medicine*, 2013. ISSN 07403194. Cited in page 63.

155 ZHANG, X. et al. Comparison of perfusion signal acquired by arterial spin labeling-prepared intravoxel incoherent motion (IVIM) MRI and conventional IVIM MRI to unravel the origin of the IVIM signal. *Magn Reson Med*, 2017. ISSN 1522-2594 (Electronic) 0740-3194 (Linking). Disponível em: <http://www.ncbi.nlm.nih.gov/pubmed/28480534>. Cited in page 69.

156 FEINBERG, D.; RAMANN, S.; GUNTHER, M. Evaluation of new ASL 3D GRASE sequences using Parallel Imaging , Segmented and Interleaved k-space at 3T with 12- and 32-channel Coils. *Proc. Intl. Soc. Mag. Reson. Med. 17*, v. 52, n. mx, p. 623, 2009. Cited 2 times in pages 70 and 71.

157 VIDORRETA, M. et al. Comparison of 2D and 3D single-shot ASL perfusion fMRI sequences. *NeuroImage*, 2013. ISSN 10959572. Cited in page 71.

158 WANG, J. et al. Arterial transit time imaging with flow encoding arterial spin tagging (FEAST). *Magnetic Resonance in Medicine*, 2003. ISSN 07403194. Cited in page 71.

159 LE, T. T. et al. Identification of venous signal on arterial spin labeling improves diagnosis of dural arteriovenous fistulas and small arteriovenous malformations. *American Journal of Neuroradiology*, 2012. ISSN 01956108. Cited in page 71.

160 WOLF, R. L. et al. Arteriovenous shunt visualization in arteriovenous malformations with arterial spin-labeling MR imaging. *American Journal of Neuroradiology*, 2008. ISSN 01956108. Cited in page 71.

161 KROGH, A. Book. *The anatomy and physiology of capillaries*. New Haven, Conn.: Yale University Press; etc., etc., 1922. xvii, 276 p. p. (Yale university Mrs Hepsa Ely Silliman memorial lectures). Cited in page 73.

162 HALL, J. E.; GUYTON, A. C. Book. *Guyton and Hall textbook of medical physiology*. 12th. ed. Philadelphia, PA: Saunders/Elsevier, 2011. xix, 1091p. p. ISBN 9781416045748 (alk. paper). Cited in page 73.

163 Le Bihan, D. Theoretical principles of perfusion imaging. Application to magnetic resonance imaging. *Invest Radiol*, v. 27 Suppl 2, p. S6–11, 1992. ISSN 0020-9996 (Print) 0020-9996 (Linking). Disponível em: <http://www.ncbi.nlm.nih.gov/pubmed/1468877>. Cited 2 times in pages 73 and 78.

164 WINTERMARK, M. et al. Comparative overview of brain perfusion imaging techniques. *J Neuroradiol*, v. 32, n. 5, p. 294–314, 2005. ISSN 0150-9861 (Print) 0150-9861 (Linking). Disponível em: <http://www.ncbi.nlm.nih.gov/entrez/query.fcgi?cmd=Retrieve{&}db=PubMed{&}dopt=Citation{&}list{_}u>. Cited in page 73.

165 OBRIG, H. NIRS in clinical neurology - a 'promising' tool? *Neuroimage*, v. 85 Pt 1, p. 535–546, 2014. ISSN 1095-9572 (Electronic) 1053-8119 (Linking). Disponível em: <http://www.ncbi.nlm.nih.gov/pubmed/23558099>. Cited in page 73.

166 SOURBRON, S. P.; BUCKLEY, D. L. Classic models for dynamic contrast-enhanced MRI. *NMR Biomed*, v. 26, n. 8, p. 1004–1027, 2013. ISSN 1099-1492 (Electronic) 0952-3480 (Linking). Disponível em: <http://www.ncbi.nlm.nih.gov/pubmed/23674304>. Cited in page 73.

167 PALDINO, M. J.; BARBORIAK, D. P. Fundamentals of quantitative dynamic contrast-enhanced MR imaging. *Magn Reson Imaging Clin N Am*, v. 17, n. 2, p. 277–289, 2009. ISSN 1557-9786 (Electronic) 1064-9689 (Linking). Disponível em: <http://www.ncbi.nlm.nih.gov/pubmed/19406359>. Cited in page 73.

168 HEYE, A. K. et al. Tracer kinetic modelling for DCE-MRI quantification of subtle blood-brain barrier permeability. *Neuroimage*, v. 125, p. 446–455, 2016. ISSN 1095-9572 (Electronic) 1053-8119 (Linking). Disponível em: <http://www.ncbi.nlm.nih.gov/pubmed/26477653>. Cited in page 73.

169 WILLIAMS, D. S. et al. Magnetic resonance imaging of perfusion using spin inversion of arterial water. *Proceedings of the National Academy of Sciences U S A*, v. 89, n. 1, p. 212–216, 1992. ISSN 0027-8424 (Print) 0027-8424 (Linking). Disponível em: <http://www.ncbi.nlm.nih.gov/pubmed/1729691>. Cited in page 74.

170 YAMADA, I. et al. Diffusion coefficients in abdominal organs and hepatic lesions: evaluation with intravoxel incoherent motion echo-planar MR imaging. *Radiology*, v. 210, n. 3, p. 617–623, 1999. ISSN 0033-8419 (Print) 0033-8419 (Linking). Disponível em: <http://www.ncbi.nlm.nih.gov/pubmed/10207458>. Cited in page 74.

171 LUCIANI, A. et al. Liver cirrhosis: intravoxel incoherent motion MR imaging–pilot study. *Radiology*, v. 249, n. 3, p. 891–899, 2008. ISSN 1527-1315 (Electronic) 0033-8419 (Linking). Disponível em: <http://www.ncbi.nlm.nih.gov/pubmed/19011186>. Cited in page 74.

172 HU, F. et al. Liver fibrosis: in vivo evaluation using intravoxel incoherent motion-derived histogram metrics with histopathologic findings at 3.0 T. *Abdom Radiol (NY)*, 2017. ISSN 2366-0058 (Electronic). Disponível em: <http://www.ncbi.nlm.nih.gov/pubmed/28624925>. Cited in page 74.

173 MEEUS, E. M. et al. Rapid measurement of intravoxel incoherent motion (IVIM) derived perfusion fraction for clinical magnetic resonance imaging. *MAGMA*, 2017. ISSN 1352-8661 (Electronic) 0968-5243 (Linking). Disponível em: <http://www.ncbi.nlm.nih.gov/pubmed/29075909>. Cited in page 74.

174 EINSTEIN, A. Book. *Investigations on the theory of the Brownian movement*. New York: Dover Publications, 1956. 119 p. p. Cited in page 74.

175 BUDINGER, T. F. et al. Tissue perfusion phantom for magnetic resonance flow studies. In: *4th annual meeting of Society of Magnetic Resonance in Medicine*. [S.l.: s.n.]. p. 577–588. Cited in page 74.

176 STEJSKAL, E. O.; TANNER, J. E. Spin Diffusion Measurements: Spin Echoes in the Presence of a Time-Dependent Field Gradient. *Journal of Chemical Physics*, v. 42, n. 1, p. 288–+, 1965. ISSN 0021-9606. Cited in page 75.

177 LEMKE, A. et al. Toward an optimal distribution of b values for intravoxel incoherent motion imaging. *Magnetic Resonance Imaging*, v. 29, n. 6, p. 766–776, 2011. ISSN 0730-725x. Cited in page 76.

178 NEIL, J. J.; SCHERRER, L. A.; ACKERMAN, J. J. H. An Approach to Solving the Dynamic-Range Problem in Measurement of the Pseudodiffusion Coefficient Invivo with Spin Echoes. *Journal of Magnetic Resonance*, v. 95, n. 3, p. 607–614, 1991. ISSN 0022-2364. Cited in page 76.

179 HENKELMAN, R. M.; NEIL, J. J.; XIANG, Q. S. A Quantitative Interpretation of Ivim Measurements of Vascular Perfusion in the Rat-Brain. *Magnetic Resonance in Medicine*, v. 32, n. 4, p. 464–469, 1994. ISSN 0740-3194. Cited in page 77.

180 NEIL, J. J.; ACKERMAN, J. J. H. Detection of Pseudodiffusion in Rat-Brain Following Blood Substitution with Perfluorocarbon. *Journal of Magnetic Resonance*, v. 97, n. 1, p. 194–201, 1992. ISSN 0022-2364. Cited in page 77.

181 NEIL, J. J.; BOSCH, C. S.; ACKERMAN, J. J. H. An Evaluation of the Sensitivity of the Intravoxel Incoherent Motion (Ivim) Method of Blood-Flow Measurement to Changes in Cerebral Blood-Flow. *Magnetic Resonance in Medicine*, v. 32, n. 1, p. 60–65, 1994. ISSN 0740-3194. Cited in page 77.

182 FOURNET, G. et al. A two-pool model to describe the IVIM cerebral perfusion. *J Cereb Blood Flow Metab*, v. 37, n. 8, p. 2987–3000, 2017. ISSN 1559-7016 (Electronic) 0271-678X (Linking). Disponível em: <http://www.ncbi.nlm.nih.gov/pubmed/27903921>. Cited 4 times in pages 77, 78, 87, and 90.

183 BERTLEFF, M. et al. Diffusion parameter mapping with the combined intravoxel incoherent motion and kurtosis model using artificial neural networks at 3 T. *NMR Biomed*, v. 30, n. 12, 2017. ISSN 1099-1492 (Electronic) 0952-3480 (Linking). Disponível em: <http://www.ncbi.nlm.nih.gov/pubmed/28960549>. Cited in page 78.

184 GUSTAFSSON, O. et al. Impact of prior distributions and central tendency measures on Bayesian intravoxel incoherent motion model fitting. *Magn Reson Med*, v. 79, n. 3, p. 1674–1683, 2018. ISSN 1522-2594 (Electronic) 0740-3194 (Linking). Disponível em: <http://www.ncbi.nlm.nih.gov/pubmed/28626964>. Cited in page 78.

185 KEIL, V. C. et al. Intravoxel incoherent motion MRI in the brain: Impact of the fitting model on perfusion fraction and lesion differentiability. *J Magn Reson Imaging*, v. 46, n. 4, p. 1187–1199, 2017. ISSN 1522-2586 (Electronic) 1053-1807 (Linking). Disponível em: <http://www.ncbi.nlm.nih.gov/pubmed/28152250>. Cited 3 times in pages 78, 88, and 90.

186 BISDAS, S. et al. Correlative assessment of tumor microcirculation using contrast-enhanced perfusion MRI and intravoxel incoherent motion diffusion-weighted MRI: Is there a link between them? *NMR in Biomedicine*, v. 27, n. 10, p. 1184–1191, 2014. ISSN 10991492. Cited in page 78.

187 HENKELMAN, R. M. Does Ivim Measure Classical Perfusion. *Magnetic Resonance in Medicine*, v. 16, n. 3, p. 470–475, 1990. ISSN 0740-3194. Cited in page 78.

188 Le Bihan, D.; TURNER, R. The capillary network: a link between IVIM and classical perfusion. *Magn Reson Med*, v. 27, n. 1, p. 171–178, 1992. ISSN 0740-3194 (Print) 0740-3194 (Linking). Disponível em: <http://www.ncbi.nlm.nih.gov/pubmed/1435202>. Cited 2 times in pages 78 and 79.

189 SOURBRON, S. P.; BUCKLEY, D. L. Classic models for dynamic contrast-enhanced MRI. *Nmr in Biomedicine*, v. 26, n. 8, p. 1004–1027, 2013. ISSN 0952-3480. Cited in page 79.

190 YAO, Y. et al. Intravoxel incoherent motion diffusion-weighted imaging in stroke patients: initial clinical experience. *Clin Radiol*, v. 71, n. 9, p. 938 e11–6, 2016. ISSN 1365-229X (Electronic) 0009-9260 (Linking). Disponível em: <http://www.ncbi.nlm.nih.gov/pubmed/27210244>. Cited 2 times in pages 80 and 81.

191 LIANG, L. et al. Using intravoxel incoherent motion MR imaging to study the renal pathophysiological process of contrast-induced acute kidney injury in rats: Comparison with conventional DWI and arterial spin labelling. *Eur Radiol*, v. 26, n. 6, p. 1597–1605, 2016. ISSN 1432-1084 (Electronic) 0938-7994 (Linking). Disponível em: <http://www.ncbi.nlm.nih.gov/pubmed/26373761>. Cited in page 80.

192 WU, W. C. et al. Caveat of measuring perfusion indexes using intravoxel incoherent motion magnetic resonance imaging in the human brain. *Eur Radiol*, v. 25, n. 8, p. 2485–2492, 2015. ISSN 1432-1084 (Electronic) 0938-7994 (Linking). Disponível em: <http://www.ncbi.nlm.nih.gov/pubmed/25693668>. Cited in page 80.

193 FEDERAU, C. et al. Measuring brain perfusion with intravoxel incoherent motion (IVIM): initial clinical experience. *J Magn Reson Imaging*, v. 39, n. 3, p. 624–632, 2014. ISSN 1522-2586 (Electronic) 1053-1807 (Linking). Disponível em: <http://www.ncbi.nlm.nih.gov/pubmed/24068649>. Cited 2 times in pages 80 and 82.

194 HEYE, A. K. et al. Assessment of blood-brain barrier disruption using dynamic contrast-enhanced MRI. A systematic review. *Neuroimage-Clinical*, v. 6, p. 262–274, 2014. ISSN 2213-1582. Cited in page 80.

195 HUANG, Y. C. et al. Comparison of arterial spin labeling and dynamic susceptibility contrast perfusion MRI in patients with acute stroke. *PLoS One*, v. 8, n. 7, p. e69085, 2013. ISSN 1932-6203 (Electronic) 1932-6203 (Linking). Disponível em: <http://www.ncbi.nlm.nih.gov/pubmed/23874876>. Cited in page 80.

196 ZHANG, S. X. et al. Comparative study of DSC-PWI and 3D-ASL in ischemic stroke patients. *J Huazhong Univ Sci Technolog Med Sci*, v. 35, n. 6, p. 923–927, 2015. ISSN 1672-0733 (Print) 1672-0733 (Linking). Disponível em: <http://www.ncbi.nlm.nih.gov/pubmed/26670447>. Cited in page 80.

197 JAHNG, G. H. et al. Perfusion magnetic resonance imaging: a comprehensive update on principles and techniques. *Korean J Radiol*, v. 15, n. 5, p. 554–577, 2014. ISSN 2005-8330 (Electronic) 1229-6929 (Linking). Disponível em: <http://www.ncbi.nlm.nih.gov/pubmed/25246817>. Cited in page 80.

198 MACINTOSH, B. J. et al. Assessment of arterial arrival times derived from multiple inversion time pulsed arterial spin labeling MRI. *Magn Reson Med*, v. 63, n. 3, p. 641–647, 2010. ISSN 1522-2594 (Electronic) 0740-3194 (Linking). Disponível em: <http://www.ncbi.nlm.nih.gov/pubmed/20146233>. Cited in page 80.

199 MUIR, K. W. et al. Imaging of acute stroke. *Lancet Neurology*, v. 5, n. 9, p. 755–768, 2006. ISSN 1474-4422. Cited in page 81.

200 WIRESTAM, R. et al. The perfusion fraction in volunteers and in patients with ischaemic stroke. *Acta Radiol*, v. 38, n. 6, p. 961–964, 1997. ISSN 0284-1851 (Print) 0284-1851 (Linking). Disponível em: <http://www.ncbi.nlm.nih.gov/pubmed/9394649>. Cited in page 81.

201 FEDERAU, C. et al. Intravoxel incoherent motion perfusion imaging in acute stroke: initial clinical experience. *Neuroradiology*, v. 56, n. 8, p. 629–635, 2014. ISSN 1432-1920 (Electronic) 0028-3940 (Linking). Disponível em: <http://www.ncbi.nlm.nih.gov/pubmed/24838807>. Cited in page 81.

202 HU, L. B.; HONG, N.; ZHU, W. Z. Quantitative Measurement of Cerebral Perfusion with Intravoxel Incoherent Motion in Acute Ischemia Stroke: Initial Clinical Experience. *Chin Med J (Engl)*, v. 128, n. 19, p. 2565–2569, 2015. ISSN 0366-6999 (Print) 0366-6999 (Linking). Disponível em: <http://www.ncbi.nlm.nih.gov/pubmed/26415791>. Cited in page 81.

203 SUO, S. et al. Stroke assessment with intravoxel incoherent motion diffusion-weighted MRI. *NMR Biomed*, v. 29, n. 3, p. 320–328, 2016. ISSN 1099-1492 (Electronic) 0952-3480 (Linking). Disponível em: <http://www.ncbi.nlm.nih.gov/pubmed/26748572>. Cited in page 82.

204 WARDLAW, J. M. Blood-brain barrier and cerebral small vessel disease. *Journal of the Neurological Sciences*, v. 299, n. 1-2, p. 66–71, 2010. ISSN 0022-510x. Cited in page 82.

205 CORDONNIER, C.; Al-Shahi Salman, R.; WARDLAW, J. Spontaneous brain microbleeds: systematic review, subgroup analyses and standards for study design and reporting. *Brain*, v. 130, n. Pt 8, p. 1988–2003, 2007. ISSN 1460-2156 (Electronic) 0006-8950 (Linking). Disponível em: <http://www.ncbi.nlm.nih.gov/pubmed/17322562>. Cited in page 82.

206 EWERS, M. et al. Multicenter assessment of reliability of cranial MRI. *Neurobiol Aging*, v. 27, n. 8, p. 1051–1059, 2006. ISSN 1558-1497 (Electronic) 0197-4580 (Linking). Disponível em: <http://www.ncbi.nlm.nih.gov/pubmed/16169126>. Cited in page 82.

207 JOVICICH, J. et al. MRI-derived measurements of human subcortical, ventricular and intracranial brain volumes: Reliability effects of scan sessions, acquisition sequences, data analyses, scanner upgrade, scanner vendors and field strengths. *Neuroimage*, v. 46, n. 1, p. 177–192, 2009. ISSN 1095-9572 (Electronic) 1053-8119 (Linking). Disponível em: <http://www.ncbi.nlm.nih.gov/pubmed/19233293>. Cited in page 82.

208 KRUGGEL, F. et al. Impact of scanner hardware and imaging protocol on image quality and compartment volume precision in the ADNI cohort. *Neuroimage*, v. 49, n. 3, p. 2123–2133, 2010. ISSN 1095-9572 (Electronic) 1053-8119 (Linking). Disponível em: <http://www.ncbi.nlm.nih.gov/pubmed/19913626>. Cited in page 82.

209 REIG, S. et al. Assessment of the increase in variability when combining volumetric data from different scanners. *Hum Brain Mapp*, v. 30, n. 2, p. 355–368, 2009. ISSN 1097-0193 (Electronic) 1065-9471 (Linking). Disponível em: <http://www.ncbi.nlm.nih.gov/pubmed/18064586>. Cited in page 82.

210 ROOB, G. et al. MRI evidence of past cerebral microbleeds in a healthy elderly population. *Neurology*, v. 52, n. 5, p. 991–994, 1999. ISSN 0028-3878 (Print) 0028-3878 (Linking). Disponível em: <http://www.ncbi.nlm.nih.gov/pubmed/10102418>. Cited in page 82.

211 SCHNACK, H. G. et al. Reliability of brain volumes from multicenter MRI acquisition: a calibration study. *Hum Brain Mapp*, v. 22, n. 4, p. 312–320, 2004. ISSN 1065-9471 (Print) 1065-9471 (Linking). Disponível em: <http://www.ncbi.nlm.nih.gov/pubmed/15202109>. Cited in page 82.

212 WARDLAW, J. M. et al. Neuroimaging standards for research into small vessel disease and its contribution to ageing and neurodegeneration. *Lancet Neurol*, v. 12, n. 8, p. 822–838, 2013. ISSN 1474-4465 (Electronic) 1474-4422 (Linking). Disponível em: <http://www.ncbi.nlm.nih.gov/pubmed/23867200>. Cited in page 82.

213 WONDERLICK, J. S. et al. Reliability of MRI-derived cortical and subcortical morphometric measures: effects of pulse sequence, voxel geometry, and parallel imaging. *Neuroimage*, v. 44, n. 4, p. 1324–1333, 2009. ISSN 1095-9572 (Electronic) 1053-8119 (Linking). Disponível em: <http://www.ncbi.nlm.nih.gov/pubmed/19038349>. Cited in page 82.

214 MARKUS, H. S. et al. Reduced cerebral blood flow in white matter in ischaemic leukoaraiosis demonstrated using quantitative exogenous contrast based perfusion MRI. *Journal of Neurology Neurosurgery and Psychiatry*, v. 69, n. 1, p. 48–53, 2000. ISSN 0022-3050. Cited in page 82.

215 O'SULLIVAN, M. et al. Patterns of cerebral blood flow reduction in patients with ischemic leukoaraiosis. *Neurology*, v. 59, n. 3, p. 321–326, 2002. ISSN 0028-3878. Cited in page 82.

216 WARDLAW, J. M.; SMITH, C.; DICHGANS, M. Mechanisms of sporadic cerebral small vessel disease: insights from neuroimaging. *Lancet Neurol*, v. 12, n. 5, p. 483–497, 2013. ISSN 1474-4465 (Electronic) 1474-4422 (Linking). Disponível em: <http://www.ncbi.nlm.nih.gov/pubmed/23602162>. Cited in page 82.

217 WONG, S. M. et al. Simultaneous investigation of microvasculature and parenchyma in cerebral small vessel disease using intravoxel incoherent motion imaging. *Neuroimage-Clinical*, v. 14, p. 216–221, 2017. ISSN 2213-1582. Cited 2 times in pages 82 and 83.

218 ROBLES, P. de et al. The worldwide incidence and prevalence of primary brain tumors: a systematic review and meta-analysis. *Neuro Oncol*, v. 17, n. 6, p. 776–783, 2015. ISSN 1523-5866 (Electronic) 1522-8517 (Linking). Disponível em: <http://www.ncbi.nlm.nih.gov/pubmed/25313193>. Cited in page 82.

219 MULLEN, K. M.; HUANG, R. Y. An Update on the Approach to the Imaging of Brain Tumors. *Curr Neurol Neurosci Rep*, v. 17, n. 7, p. 53, 2017. ISSN 1534-6293 (Electronic) 1528-4042 (Linking). Disponível em: <http://www.ncbi.nlm.nih.gov/pubmed/28516376>. Cited in page 82.

220 GOODENBERGER, M. L.; JENKINS, R. B. Genetics of adult glioma. *Cancer Genet*, v. 205, n. 12, p. 613–621, 2012. ISSN 2210-7762 (Print). Disponível em: <http://www.ncbi.nlm.nih.gov/pubmed/23238284>. Cited in page 82.

221 LOUIS, D. N. et al. The 2016 World Health Organization Classification of Tumors of the Central Nervous System: a summary. *Acta Neuropathol*, v. 131, n. 6, p. 803–820, 2016. ISSN 1432-0533 (Electronic) 0001-6322 (Linking). Disponível em: <http://www.ncbi.nlm.nih.gov/pubmed/27157931>. Cited in page 83.

222 FEDERAU, C. et al. Perfusion Measurement in Brain Gliomas with Intravoxel Incoherent Motion MRI. *American Journal of Neuroradiology*, v. 35, n. 2, p. 256–262, 2014. ISSN 0195-6108. Cited in page 83.

223 TOGAO, O. et al. Differentiation of high-grade and low-grade diffuse gliomas by intravoxel incoherent motion MR imaging. *Neuro-Oncology*, v. 18, n. 1, p. 132–141, 2016. ISSN 1522-8517. Cited in page 83.

224 HU, Y. C. et al. Intravoxel incoherent motion diffusion-weighted MR imaging of gliomas: efficacy in preoperative grading. *Scientific Reports*, v. 4, 2014. ISSN 2045-2322. Cited 2 times in pages 83 and 90.

225 PLATE, K. H. et al. Vascular endothelial growth factor is a potential tumour angiogenesis factor in human gliomas in vivo. *Nature*, v. 359, n. 6398, p. 845–848, 1992. ISSN 0028-0836 (Print) 0028-0836 (Linking). Disponível em: <http://www.ncbi.nlm.nih.gov/pubmed/1279432>. Cited in page 83.

226 SHIM, W. H. et al. Comparison of Apparent Diffusion Coefficient and Intravoxel Incoherent Motion for Differentiating among Glioblastoma, Metastasis, and Lymphoma Focusing on Diffusion-Related Parameter. *Plos One*, v. 10, n. 7, 2015. ISSN 1932-6203. Cited in page 84.

227 SUH, C. H. et al. Atypical Imaging Features of Primary Central Nervous System Lymphoma That Mimics Glioblastoma: Utility of Intravoxel Incoherent Motion MR Imaging. *Radiology*, v. 272, n. 2, p. 504–513, 2014. ISSN 0033-8419. Cited in page 84.

228 YAMASHITA, K. et al. Diagnostic utility of intravoxel incoherent motion mr imaging in differentiating primary central nervous system lymphoma from glioblastoma multiforme. *Journal of Magnetic Resonance Imaging*, v. 44, n. 5, p. 1256–1261, 2016. ISSN 1053-1807. Cited in page 84.

229 CALLI, C. et al. Perfusion and diffusion MR imaging in enhancing malignant cerebral tumors. *Eur J Radiol*, v. 58, n. 3, p. 394–403, 2006. ISSN 0720-048X (Print) 0720-048X (Linking). Disponível em: <http://www.ncbi.nlm.nih.gov/pubmed/16527438>. Cited in page 84.

230 GUO, A. C. et al. Lymphomas and high-grade astrocytomas: comparison of water diffusibility and histologic characteristics. *Radiology*, v. 224, n. 1, p. 177–183, 2002. ISSN 0033-8419 (Print) 0033-8419 (Linking). Disponível em: <http://www.ncbi.nlm.nih.gov/pubmed/12091680>. Cited in page 84.

231 TOH, C. H. et al. Primary cerebral lymphoma and glioblastoma multiforme: differences in diffusion characteristics evaluated with diffusion tensor imaging. *AJNR Am J Neuroradiol*, v. 29, n. 3, p. 471–475, 2008. ISSN 1936-959X (Electronic) 0195-6108 (Linking). Disponível em: <http://www.ncbi.nlm.nih.gov/pubmed/18065516>. Cited in page 84.

232 YAMASAKI, F. et al. Apparent diffusion coefficient of human brain tumors at MR imaging. *Radiology*, v. 235, n. 3, p. 985–991, 2005. ISSN 0033-8419 (Print) 0033-8419 (Linking). Disponível em: <http://www.ncbi.nlm.nih.gov/pubmed/15833979>. Cited in page 84.

233 CUI, Y. et al. Intravoxel Incoherent Motion Diffusion-weighted Magnetic Resonance Imaging for Monitoring the Early Response to ZD6474 from Nasopharyngeal Carcinoma in Nude Mouse. *Sci Rep*, v. 5, p. 16389, 2015. ISSN 2045-2322 (Electronic) 2045-2322 (Linking). Disponível em: <http://www.ncbi.nlm.nih.gov/pubmed/26574153>. Cited in page 84.

234 JOO, I. et al. Monitoring Vascular Disrupting Therapy in a Rabbit Liver Tumor Model: Relationship between Tumor Perfusion Parameters at IVIM Diffusion-weighted MR Imaging and Those at Dynamic Contrast-enhanced MR Imaging. *Radiology*, v. 278, n. 1, p. 104–113, 2016. ISSN 1527-1315 (Electronic) 0033-8419 (Linking). Disponível em: <http://www.ncbi.nlm.nih.gov/pubmed/26200601>. Cited in page 84.

235 JOO, I. et al. Intravoxel incoherent motion diffusion-weighted MR imaging for monitoring the therapeutic efficacy of the vascular disrupting agent CKD-516 in rabbit VX2 liver tumors. *Radiology*, v. 272, n. 2, p. 417–426, 2014. ISSN 1527-1315 (Electronic) 0033-8419 (Linking). Disponível em: <http://www.ncbi.nlm.nih.gov/pubmed/24697148>. Cited in page 84.

236 MARZI, S. et al. Early radiation-induced changes evaluated by intravoxel incoherent motion in the major salivary glands. *J Magn Reson Imaging*, v. 41, n. 4, p. 974–982, 2015. ISSN 1522-2586 (Electronic) 1053-1807 (Linking). Disponível em: <http://www.ncbi.nlm.nih.gov/pubmed/24700435>. Cited in page 84.

237 YANG, S. H. et al. Evaluation of antiangiogenic and antiproliferative effects of sorafenib by sequential histology and intravoxel incoherent motion diffusion-weighted imaging in an orthotopic hepatocellular carcinoma xenograft model. *J Magn Reson Imaging*, v. 45, n. 1, p. 270–280, 2017. ISSN 1522-2586 (Electronic) 1053-1807 (Linking). Disponível em: <http://www.ncbi.nlm.nih.gov/pubmed/27299302>. Cited in page 84.

238 DETSKY, J. S. et al. Differentiating radiation necrosis from tumor progression in brain metastases treated with stereotactic radiotherapy: utility of intravoxel incoherent motion perfusion MRI and correlation with histopathology. *Journal of Neuro-Oncology*, v. 134, n. 2, p. 433–441, 2017. ISSN 0167-594x. Cited 2 times in pages 84 and 85.

239 COSTA, A. et al. Brain gadolinium deposition, hyperintense MRI signals, and resonance contrast agents. *Magn Reson Imaging*, 2018. ISSN 1873-5894 (Electronic) 0730-725X (Linking). Disponível em: <http://www.ncbi.nlm.nih.gov/pubmed/29885445>. Cited in page 84.

240 FITZGERALD, R. T. et al. The Impact of Gadolinium Deposition on Radiology Practice: An International Survey of Radiologists. *Curr Probl Diagn Radiol*, 2018. ISSN 1535-6302 (Electronic) 0363-0188 (Linking). Disponível em: <http://www.ncbi.nlm.nih.gov/pubmed/29530452>. Cited in page 84.

241 PULLICINO, R. et al. A Review of the Current Evidence on Gadolinium Deposition in the Brain. *Clin Neuroradiol*, v. 28, n. 2, p. 159–169, 2018. ISSN 1869-1447 (Electronic) 1869-1439 (Linking). Disponível em: <http://www.ncbi.nlm.nih.gov/pubmed/29523896>. Cited in page 84.

242 RAHATLI, F. K. et al. Does renal function affect gadolinium deposition in the brain? *Eur J Radiol*, v. 104, p. 33–37, 2018. ISSN 1872-7727 (Electronic) 0720-048X (Linking). Disponível em: <http://www.ncbi.nlm.nih.gov/pubmed/29857863>. Cited in page 84.

243 EICHLING, J. O. et al. Evidence of the limitations of water as a freely diffusible tracer in brain of the rhesus monkey. *Circ Res*, v. 35, n. 3, p. 358–364, 1974. ISSN 0009-7330 (Print) 0009-7330 (Linking). Disponível em: <http://www.ncbi.nlm.nih.gov/pubmed/4419687>. Cited in page 84.

244 LI, K. L. et al. Four-phase single-capillary stepwise model for kinetics in arterial spin labeling MRI. *Magn Reson Med*, v. 53, n. 3, p. 511–518, 2005. ISSN 0740-3194 (Print) 0740-3194 (Linking). Disponível em: <http://www.ncbi.nlm.nih.gov/pubmed/15723393>. Cited in page 84.

245 PARKES, L. M.; TOFTS, P. S. Improved accuracy of human cerebral blood perfusion measurements using arterial spin labeling: accounting for capillary water permeability. *Magn Reson Med*, v. 48, n. 1, p. 27–41, 2002. ISSN 0740-3194 (Print) 0740-3194 (Linking). Disponível em: <http://www.ncbi.nlm.nih.gov/pubmed/12111929>. Cited in page 84.

246 ZHOU, J. et al. Two-compartment exchange model for perfusion quantification using arterial spin tagging. *J Cereb Blood Flow Metab*, v. 21, n. 4, p. 440–455, 2001. ISSN 0271-678X (Print) 0271-678X (Linking). Disponível em: <http://www.ncbi.nlm.nih.gov/pubmed/11323530>. Cited in page 84.

247 ZHANG, X. et al. Comparison of perfusion signal acquired by arterial spin labeling-prepared intravoxel incoherent motion (IVIM) MRI and conventional IVIM MRI to unravel the origin of the IVIM signal. *Magn Reson Med*, v. 79, n. 2, p. 723–729, 2018. ISSN 1522-2594 (Electronic) 0740-3194 (Linking). Disponível em: <http://www.ncbi.nlm.nih.gov/pubmed/28480534>. Cited in page 85.

248 BRUZZONE, M. G. et al. CT and MRI of brain tumors. *Q J Nucl Med Mol Imaging*, v. 56, n. 2, p. 112–137, 2012. ISSN 1824-4785 (Print) 1824-4785 (Linking). Disponível em: <http://www.ncbi.nlm.nih.gov/pubmed/22617235>. Cited in page 87.

249 LAWSON, C. L.; HANSON, R. J. Book. *Solving least squares problems*. Englewood Cliffs, N.J.,: Prentice-Hall, 1974. xii, 340 p. p. (Prentice-Hall series in automatic computation). ISBN 0138225850. Cited in page 87.

250 WHITTALL, K. P.; MACKAY, A. L. Quantitative Interpretation of Nmr Relaxation Data. *Journal of Magnetic Resonance*, v. 84, n. 1, p. 134–152, 1989. ISSN 0022-2364. Cited in page 87.

251 WU, L. M. A parameter choice method for Tikhonov regularization. *Electronic Transactions on Numerical Analysis*, v. 16, p. 107–128, 2003. ISSN 1068-9613. Cited 2 times in pages 88 and 90.

252 MOHAMMADI, S. et al. Correcting eddy current and motion effects by affine whole-brain registrations: Evaluation of three-dimensional distortions and comparison with slicewise correction. *Magnetic Resonance in Medicine*, 2010. ISSN 07403194. Cited in page 89.

253 WONG, S. et al. Spectral Diffusion IVIM Analysis of Enlarged Perivascular Spaces in Cerebral Small Vessel Disease. *Proc 17th Sci Meet Int Soc Magn Reson Med. 2017*, p. 4721, 2017. Cited in page 90.

254 FEDERAU, C. et al. Measuring brain perfusion with intravoxel incoherent motion (IVIM): initial clinical experience. *J Magn Reson Imaging*, v. 39, n. 3, p. 624–632, 2014. ISSN 1522-2586 (Electronic) 1053-1807 (Linking). Disponível em: <http://www.ncbi.nlm.nih.gov/pubmed/24068649>. Cited in page 90.